CO_2 Foam Using non-ionic Surfactants

For Increased Storage Capacity and Oil Recovery

Tore Lyngås Føyen

Thesis for the degree of Philosophiae Doctor (PhD)
University of Bergen, Norway
2020

UNIVERSITY OF BERGEN

CO2 Foam Using non-ionic Surfactants

For Increased Storage Capacity and Oil Recovery

Tore Lyngås Føyen

Thesis for the degree of Philosophiae Doctor (PhD)
at the University of Bergen

Date of defense: 18.12.2020

Year: 2020

Title: CO2 Foam Using non-ionic Surfactants

Name: Tore Lyngås Føyen

Print: Skipnes Kommunikasjon / University of Bergen

Scientific environment

This dissertation was submitted September 21, 2020, as a part of the fulfillment for the degree of Philosophiae Doctor (PhD) at the University of Bergen (UiB), department Physics and Technology. The candidate has been funded by the Research Council of Norway as instituttstipendiat (project no. 259868), employed by SINTEF Industry and supervised by Prof. Arne Graue, Prof. Martin Fernø and Researcher Bergit Brattekås at the Department Physics and Technology and Senior Researcher Torleif Holt at SINTEF Industry.

The candidate has been associated with two research groups; the Reservoir Physics research group at the University of Bergen and the Applied Geoscience group at SINTEF Industry. Both research groups have several projects on CO_2-foam for storage and enhanced oil recovery. The PhD-project has facilitated cooperation between two research groups by contributing in CO_2-foam projects lead by both groups. The candidate, therefore, wish to acknowledge the Research Council of Norway for financial support: *Improved performance of CO_2 EOR and underground storage by mobility control of CO_2* (project no. 267859), *Nanoparticles to Stabilize CO_2-foam for Efficient CCUS in Challenging Reservoirs* (project no. 268216) and *CO_2 Storage from Lab to On-Shore Field Pilots Using CO_2-Foam for Mobility Control in CCUS* (project no. 249742).

Acknowledgements

I wish to thank the Norwegian Research Council for financial support and SINTEF Industry for giving me the opportunity to participate in such a challenging project.

I would like to express my gratitude to my supervisors Professor Arne Graue, Professor Martin Fernø, and Dr. Bergit Brattekås at the Department of Physics and Technology at the University of Bergen and Senior Research Scientist Torleif Holt at SINTEF Industry. Thank you for the support, guidance, and valuable discussions. I would also like to thank Associate Professor Geir Ersland and Dr. Marianne Steinsbø for their contributions to the Reservoir Physics group.

To all my former students and colleges in the reservoir physics group at the Department of Physics and Technology and in the Applied Geoscience group in SINTEF Industry, thank you for the excellent collaboration. Thanks to Malin Hauge, Benyamine Benali, Zachary P. Alcorn, and Jarand Gauteplass, for the collaboration in the laboratory, a good atmosphere, and a productive working environment. Thanks to Martin Raphaug and Albert Barrabino for great times when visiting Trondheim. Thanks to Leilei Zhang and Metine Karakas for a memorable time at the field-site in West-Texas.

A special thanks go to my dear friend Martin Dugstad, good luck completing your Ph.D-degree!

Finally, A warm and special thanks go to my family, friends and especially my dear girlfriend Marita Drage for support and encouragement. It has been much appreciated!

Summary

Large-scale carbon capture and storage is needed to achieve the target set forward by the Paris agreement; to limit global warming to 1.5 °C. The primary obstacle for implementing large-scale carbon capture and storage is the high economical cost. Utilization of CO_2 as a commodity in production processes, commonly called carbon capture and utilization (CCUS), can establish a CO_2 value-chain and provide economic incentives. A promising use of CO_2 is for enhanced oil recovery (EOR). Additional oil can be recovered from oil reservoirs by injecting CO_2; simultaneously, CO_2 is stored in the subsurface. CO_2-EOR is field-proven, however, it has primarily been implemented using non-anthropogenic CO_2. The potential economic revenue by establishing a CO_2 value-chain with CO_2-EOR, using anthropogenic CO_2 have yet been insufficient for the industry.

CO_2-EOR has inherent challenges due to the viscosity and density differences between reservoir fluids and the injected CO_2, potentially leading to poor sweep efficiency. Poor sweep efficiency is detrimental to oil recovery and CO_2 storage. Providing technological solutions that tackle the sweep efficiency issues can potentially make CO_2-EOR feasible and catalyze the implementation of large-scale carbon capture and storage. Foam is a technological solution that decreases the mobility of CO_2 and increases sweep efficiency. This thesis presents a multi-scale investigation of foam for CO_2 mobility control stabilized using non-ionic surfactants. The study includes investigations from pore-scale foam dynamics to field-scale implementation of CO_2-foam injection, with an emphasis to produce oil from mature field with a reduced carbon footprint.

The thesis consists of five chapters. Chapter 1 provides an introduction and a rationale for the research questions addressed in this thesis, whereas Chapter 2 provides a theoretical background of fundamental concepts of foam in porous media. Chapter 3 summarizes the experimental methods and clarifies how the experiments relate to each other. Chapter 4 presents key findings from the five publications, emphasizing synergetic results from published work, and is organized into individual foam-subjects.

Chapter 5 summarizes the main conclusions of the dissertation. The five listed publications constituting the dissertation are briefly described in the next paragraphs:

Paper 1 presents a comprehensive pore-scale investigation of CO_2 foam dynamics using a micromodel with an irregular pore network at dense CO_2 conditions. Quantitative analysis of bubble dynamics was performed, and foam generation and decay mechanisms were identified. Experimental observations of trapped bubbles, bubble trains and gas channels were contextualized in the framework developed for population balance foam models. The observations corroborated core scale behavior reported in Paper 2 & 4.

Paper 2 presents a series of unsteady-state injections of dense phase CO_2 in a long sandstone outcrop core (1.15 m) pre-saturated with surfactant solutions. Five commercially available non-ionic, non-fluorinated, partially CO_2-soluble surfactants were evaluated and compared with the well-known anionic, water-soluble AOS surfactant. The paper emphasizes the improved storage capacity of CO_2 obtained by foam due to decreased residual water saturation. The unsteady-state injections also gave insights on foam generation and decay. Three foam generation categories were defined based on the build-up of foam strength as a function of the amount of CO_2 injected. Mass transfer of the partially CO_2 soluble surfactants from water to the flowing CO_2, and the potential effect on foam decay was addressed.

Paper 3 extends on the work presented in Paper 1, by including complementary core-scale experiments using the same foaming agent solutions. Hybrid foaming agent solutions, containing nanoparticles and surfactant, were compared with foaming agent solutions containing surfactant and nanoparticles only. Additionally, the effect of residual oil saturation on foam stability was evaluated. All foaming agent solutions containing surfactant generated foam in the absence and presence of oil at the core- and pore-scale.

Paper 4 presents a series of steady-state foam co-injections with dense phase CO_2 and six different surfactant solutions at varying CO_2 flow velocities and CO_2 fractions. The study extends on the steady-state evaluation presented in Paper 2 and uses the same six commercially available surfactants. All of the tested surfactants generated foam and reduced CO_2 mobility by more than three orders of magnitude and increased the pore volume available for CO_2 storage. The experimental data were fitted to an empirical foam model and can be used as input for reservoir simulations. The experiments were performed in sandstone representative for north-sea reservoirs and can potentially be useful for feasibility studies of CO_2 -EOR with mobility control using foam.

Paper 5 presents the design, monitoring program, and preliminary results from the on-going CO_2-foam field pilot performed in Permian Basin, USA. The pilot is performed to demonstrate the feasibility and benefits of foam during CO_2 -EOR and to reduce the knowledge gap between laboratory- and field-scale foam displacement processes.

List of Publications

1. **Føyen, T**., Benali, B., Haugen, M., Gauteplass, J., Kovscek, A.R., Fernø, M.A. Pore-scale Bubble Population Dynamics of CO_2-Foam. *Transport in Porous Media,* submitted Aug. 2020

2. **Føyen, T**., Brattekås, B., Fernø, M.A., Barrabino, A., Holt, T. Increased CO_2 storage capacity using CO_2 -foam. *International Journal of Greenhouse Gas Control*. Volume 96, 2020, https://doi.org/10.1016/j.ijggc.2020.103016

3. Alcorn, Z.P., **Føyen, T**., Gauteplass, J., Benali, B., Soyke, A., Fernø, M.A. Pore- and core-scale insights of nanoparticle-stabilized foam for CO_2 enhanced oil recovery, *Nanomaterials,* accepted Sept. 2020

4. **Føyen, T**.,Alcorn, Z.P., Fernø, M.A., Barrabino, A., Holt, T.CO_2 mobility reduction using foam stabilized by CO_2- and water-soluble surfactants. *Journal of Petroleum Science and Engineering*. Volume 196, 2020, 107651, https://doi.org/10.1016/j.petrol.2020.107651

5. Alcorn, Z.P., **Føyen, T.**, Zhang, L., Karakas, M., Biswal, L., Hirasaki, G., Graue, A. CO_2 foam field pilot design and initial results. Proceeding at SPE Improved Oil Recovery Conference, Tulsa, Oklahoma, USA, Aug 31st to Sept 4th 2020,https://doi.org/10.2118/200450-MS

Additional Scientific Contributions

Alcorn, Z.P., Fredriksen, S.B, Sharma, M., Rognmo U.A., **Føyen, T**., Fernø, M.A., Graue, A. An Integrated Carbon-Dioxide-Foam Enhanced-Oil-Recovery Pilot Program With Combined Carbon Capture, Utilization, and Storage in an Onshore Texas Heterogeneous Carbonate Field. *SPE Reservoir Evaluation & Engineering* 2019

Alcorn, Z.P., Fredriksen, S.B, Sharma, M., **Føyen, T**., Wergeland, C., Fernø, M.A., Graue, A.,Ersland, G. Core-scale sensitivity study of CO_2 foam injection strategies for mobility control, enhanced oil recovery, and CO_2 storage. *E3S Web of Conferences SCA 2019*

Rognmo U.A., Fredriksen, Alcorn, Z.P., S.B, Sharma, M., **Føyen, T**., Eide, Ø., Graue, A., Fernø, M.A.,Pore-to-Core EOR Upscaling for CO_2 Foam for CCUS. *SPE Journal* 2019

Eide, Ø., **Føyen, T**., Skjelsvik E.B, Rognmo U.A., Fernø, M.A. Nanoparticle Stabilized Foam in Harsh Conditions for CO_2 EOR. Proceeding at the SPE Abu Dhabi International Petroleum Exhibition & Conference, Abu Dhabi, UAE, 12-15 November 2018.

Andersen, P.Ø., Brattekås, B., Nødland, O.M., Lohne, A., **Føyen, T.**, Fernø, M.A. Darcy-Scale Simulation of Boundary-Condition Effects During Capillary-Dominated Flow in High-Permeability System. *SPE Reservoir Evaluation & Engineering* 2019

Føyen, T., Fernø, M.A., Brattekås, B.The Effects of Nonuniform Wettability and Heterogeneity on Induction Time and Onset of Spontaneous Imbibition. SPE Journal 2019

Brattekås, B., **Føyen, T**., Vabø, T., Haugland, H., Reite, S.I., Saunes, A.S., Fernø, M.A. Dos and Don'ts When Developing a System to Investigate Spontaneous Imbibition in Unconsolidated Porous Media. *E3S Web of Conferences SCA 2018*

Alcorn, Z.P., **Føyen, T**., Karakas, M., Zhang, L., Biswal, L., Hirasaki, G., Graue, A. Preliminary Progress Report:East Seminole CO_2 Foam Field Pilot, Report (April 30, 2020)
Andersen, P.Ø., **Føyen, T.**, Jaldeepsinh, C., Brattekås, B.Interpretation of Induction Time and Nonstandard Spontaneous Imbibition Trends Utilizing In-situ Measurements -Identification of No-Flow Regions and Wettability Alteration. Proceeding at the EAGE IOR, Pau, France, 8-11April 2019

Contents

1. Introduction

Historically there has been a strong positive correlation between energy consumption and the Human Development Index (Wu & Chen 2017). The human development and prosperity have been fuel using abundantly available and reliable energy from fossil sources. However, the combustion of fossils fuels releases CO_2, and the subsequent accumulation in the atmosphere has caused the global temperature to increase. The continued increase in global temperature must be halted to avoid long-lasting negative changes to the natural environment, and the Paris agreement aims to limit global warming to 1.5 °C (Arneth 2019). Four emission pathways are mapped in the SPECIAL REPORT: GLOBAL WARMING OF 1.5 °C by IPCC (2018), and require global net-negative CO_2 emissions in the forthcoming century (**Fig.1**).

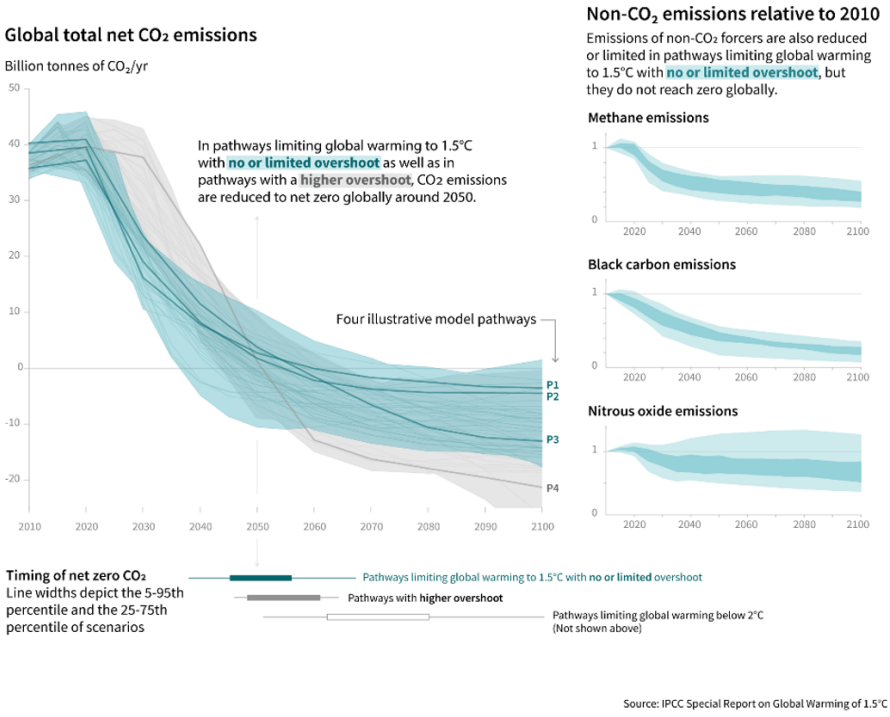

Fig. 1: Global emissions pathway characteristics. General characteristics of the evolution of anthropogenic net emissions of CO_2 that limit global warming to 1.5 °C. Net emissions are defined as anthropogenic emissions reduced by anthropogenic removals. Figure from Summary for Policymakers IN: Special Report on Global Warming of 1.5 °C, page 13, Figure SPM.3a and SPM.3b. IPCC, 2018

Continued development in human prosperity requires increased production of cheap and available energy. There is a clear on-going shift in the global energy mix with an increased use of renewable energy sources (IEA 2019). Additionally, the development of feasible energy carriers, such as batteries and hydrogen or hydrogen-derived fuels, to replace easily transportable high energy density hydrocarbons, have come far. However, despite the on-going shift in the global energy mix, gas and oil production is expected to continue to contribute to the fossil fuel dependency in the foreseeable future (IEA 2019). Additionally, the increased use of renewable energy sources mix does not directly address releases of anthropogenic CO_2 from industrial processes, such as incineration of waste and production of metals and cement.

Large-scale implementation of carbon capture and storage (CCS) is needed to achieve net-negative CO_2 emissions (IPCC 2018). Large-scale carbon capture and storage involves capture, transport and injection of CO_2 into suitable subsurface geological formations for safe storage (Svensson et al. 2004; Balat & Öz 2007; Bickle 2009). Emission from point sources, e.g., power plants and industrial sources can be captured (Leeson *et al.* 2017). Natural gas can be converted to hydrogen and hydrogen derived fuels, and the associated carbon captured (Gaudernack & Lynum 1998). Remaining releases of anthropogenic CO_2 from sources that are challenging to capture must be compensated with carbon dioxide removal, such as carbon capture and storage from biomass sources. Overall, the total deployment level of carbon dioxide removal (CDR) through the 21st century, which includes storage in geological formations, is estimated in the order of 100–1000 Gt CO_2 (IPCC 2018).

The largest obstacle for implementing large-scale carbon capture and storage is the high economical cost (Lipponen *et al.* 2017).Utilization of CO_2 as a commodity in production processes, commonly called carbon capture and utilization (CCUS), can establish a CO_2 value-chain and provide economic incentives. A promising use of CO_2 is for enhanced oil recovery (CO_2 -EOR) (Mac Dowell *et al.* 2017). Additional oil can be recovered by injecting CO_2 into oil reservoirs simultaneously CO_2 is stored. The carbon footprint from the global consumption of hydrocarbons can be reduce by combining CO_2 -EOR and CO_2 storage, as the injected and stored CO_2 can account for the emitted CO_2 when the

produced oil combusted (Lindeberg *et al.* 2017; Ettehadtavakkol *et al.* 2014).CO_2-EOR is field-proven, however, it has primarily been implemented using non-anthropogenic CO_2. The potential economic revenue by establishing a CO_2 value-chain with CO_2-EOR, using anthropogenic CO_2, has yet been insufficient for the industry.

Injection of CO_2 for EOR has been performed since the nineteen-seventies and the first full-scale implementation is still ongoing (Langston *et al.* 1988). The efforts to implement CO_2-EOR (including modified production sites, pipelines for transportation, and distribution hubs) illustrate, together with the projects' longevity, the advantages of using CO_2 for oil recovery. CO_2 can act as a miscible solvent with crude oil, which improves oil recovery (Shokrollahi *et al.* 2013; Elsharkawy *et al.* 1996). Miscibility between the injected CO_2 and oil can be instant (first contact) or develop over time (multi-contact), depending on oil composition, temperature, and pressure conditions. CO_2/oil miscibility causes the oil to swell, while simultaneously reducing oil viscosity and interfacial tension, causing oil trapped by capillary forces to be mobilized and produced. Yet, several decades of CO_2-EOR has shown mixed results due to poor sweep efficiency, causing early gas breakthrough and high producing gas-oil ratios (GOR) (Moffitt *et al.* 2015). The poor sweep efficiency arises from the high mobility of CO_2 at reservoir conditions, compared with oil and brine (Lake *et al.* 2014), causing gravity override, viscous fingering, and gas channeling (Lee & Kam 2013; Shi & Rossen 1998). Implications of early gas breakthrough and high GOR are reduced oil production and additional costs associated with separation and recycling of produced CO_2. Additionally, recycling of CO_2 is detrimental for CO_2-EOR projects' sustainability, as it decreases the exergy recovered from the produced oil (Farajzadeh *et al.* 2020). Providing technological solutions for improving the sweep efficiency can potentially make CO_2-EOR using anthropogenic CO_2 feasible. CO_2 mobility control by foams is a potential technological solution as it can decrease the mobility of CO2 and subsequently increased sweep efficiency. The mobility of CO_2, defined as:

$$\lambda_g = \frac{k_{rCO2}}{\mu_{CO2}} \tag{1}$$

, where k_{rg} refers to CO_2 relative permeability and μ_g to viscosity.

Foam

Foam is a field-tested and promising method for gas/CO_2 mobility control (Chou *et al.* 1992; Hoefner & Evans 1995; Henry *et al.* 1996; Blaker *et al.* 1999), and can be described as a two-phase system consisting of dispersed gas bubbles separated by aqueous films, called lamella (Kovscek & Radke 1994). Foam effectively reduces the mobility of CO_2 because the lamellas impedes the flow of the discontinuous CO_2 phase. Studies of foam injection have primarily emphasized enhanced oil recovery, as the recovered oil gives revenue. The potential of foam to increase CO_2 storage capacity in geological formations, due to improved sweep efficiency and reduced water saturation in the swept volumes is less addressed.

Reduction in oil and water saturations occurs by increased viscous forces and a reduction of capillary forces (for oil/CO_2 systems, miscible displacement enhance local reduction in oil saturation). As shown in capillary desaturation curves, the residual saturation decreases when the capillary number increases (Fulcher *et al.* 1985; Guo *et al.* 2017). This concept is, in principle, also valid for CO_2-water systems. Foams are particularly effective for increasing the capillary number (N_{ca}), by increasing viscosity (μ) while simultaneously reducing the interfacial tension (σ) between CO_2 and water by surfactants.

The ratio between viscous forces and capillary forces defines the capillary number:

$$N_{ca} = \frac{u * \mu}{\sigma} \tag{2}$$

where u is the superficial Darcy velocity.

The global volumetric storage capacity is abundant compared with the estimated need for storage (Kearns *et al.* 2017), and optimization of storage efficiency and capacity might appear unnecessary. However, there are several arguments for minimizing the number of storage sites and optimizing storage at individual sites:

i) It is beneficial to use the formations with the best geological properties, ensuring safe storage of the injected CO_2 (Anthonsen *et al.* 2014).

ii) Storage locations geographically located near CO_2 emission sources simplifies infrastructure and logistics, and are therefore preferable.

iii) It is preferable to establish a minimum number of storage sites, as there is a cost associated with necessary infrastructure (e.g., transportation systems, surface infrastructure, and injection and production wells).

iv) There is a cost associated with characterizing the formation and monitoring during and after the injection period.

Increasing the CO_2 storage capacity is also desirable when combining CO_2 -EOR and CO_2 storage to achieve net neutral or negative CO_2 emissions, where the stored CO_2 accounts for the CO_2 released during combustion of the recovered oil. The experimental observations presented in this thesis demonstrate the ability of foam to increase storage capacity by increasing the CO_2 saturation (Paper 2 & 4).

Reservoirs are large (km) with complex geometries and commonly have a heterogeneous distribution of flow properties (permeability). Direct replication of reservoir behavior is impractical to perform in a controlled laboratory environment. Numerical modeling is therefore needed to assess displacement prosses in reservoirs. Numerical modeling relies heavily on empirical data obtained by laboratory investigations. Empirical data are needed to validate and develop numerical models. The models should be able to capture the same dynamics as observed in the laboratory. Additionally, the numerical models require empirical data as input parameters to fine-tune the model for specific cases.

Validation of foam models and assessments of which dynamics to be capture can be performed with more confidence if field-scale data is available. The project *CO_2 Storage from Lab to On-Shore Field Pilots Using CO_2-Foam for Mobility Control in CCUS* has therefore performed a foam field-pilot. The field pilot aims to reduce the knowledge gap between laboratory- and field-scale foam displacement processes and demonstrate the

feasibility of using foam during CO_2-EOR. The project is a collaborative effort, led by the University of Bergen, and takes a multidisciplinary and multiscale approach to design and executing the field pilot.

The pilot is performed in the East Seminole oil field located in the Permian Basin of west Texas. The development of the oil field started in the 1960s by primary depletion. Water flooding was initiated in the early 1970s, and CO_2 flooding started in 2013. Early CO_2 breakthrough and high gas-oil production ratios (GOR) were observed in the production wells: the field is, therefore, an excellent candidate for implementing and testing CO_2 foam. The rationale of performing a field test onshore in the Permian Basin is threefold: extensive regional experience with CO_2-EOR, CO_2 readily available and short distances between injection and production wells (compared with offshore fields).

The CO_2-foam field pilot is performed in one single injection well, and adjacent production wells are monitored. The foam injection started in May 2019 and is still ongoing as of September 2020. The foam injection strategy employed for the field pilot is SAG, where each injection cycle constitutes 10 days of surfactant injection (0.5 wt%) followed by 20 days of CO_2 injection. A non-ionic non-fluorinated surfactant (linear alcohol ethoxylates) with the commercial name Surfonic L24-22 and provided by Huntsman is used as the foaming agent. The Surfonic L24-22 is used in the two of the laboratory studies (Paper 1 & 3), and is chemically similar to one of the five non-ionic surfactants (Brij L23) used in Papers 2 & 4.

2. Fundamental concepts of CO_2-foam

Foam is a two-phase system consisting of dispersed gas bubbles and continuous thin aqueous films, called lamella. The experiments presented in this thesis are performed at pressures and temperatures where CO_2 is a liquid or a supercritical fluid with high density ($0.84 - 0.85 \frac{g}{ml}$), and the foam systems are, by definition, an emulsion. However, the term foam is used, and the term "gas" is used interchangeably for dense CO_2 in this thesis. Because foams are thermodynamically unstable systems, the lamellae require a foaming agent to be stabilized, most commonly surfactant.

Surfactants

Surfactants stabilize the basic structural elements of foam: lamellae and plateau borders (where the lamellas meet and form corners), by providing a disjoining pressure, further described by the DLVO theory (Kontogeorgis & Kiil 2016). The disjoining pressure arises from surfactant molecules adsorbed at both sides of the gas-water interface (lamella), providing repulsive forces between them. Insufficient repulsive forces will lead to drainage of water from the lamella to the curved plateau borders by Laplace capillary forces and subsequent lamellae collapse. The disjoining pressure also provides stability towards the porous medium's capillary pressure, which causes capillary suction drainage (Kovscek & Radke 1994).

Several factors must be considered before selecting a surfactant for foam mobility control, including the surfactant ability to generate foam, adsorption and subsequent loss to the reservoir rock, chemical stability at reservoir conditions, and environmental concerns due to potential toxicity. Additionally, economic aspects concerning surfactant price and volume needed must be considered. Numerous surfactants exist and are subdivided into categories based on the polarity of the head group: nonionic, anionic, cationic, amphoteric. Surfactants are commonly dissolved in water, however, using surfactants that are soluble in both phases (water and CO_2) can have inherent benefits as they are more easily transported into the reservoir.

Studies by (Adkins *et al.* 2010a; Adkins *et al.* 2010b) showed the potential for non-fluorinated non-ionic surfactant that partition between CO_2 and water as foaming agents. Additional studies have been published during the last decade, testing different non-fluorinated non-ionic surfactant as foaming agents, including: linear and branched alkylphenol ethoxylates (McLendon *et al.* 2012; Xing *et al.* 2010), branched alkyl ethoxylates (Xing *et al.* 2012), and linear alcohol ethoxylate (Chen *et al.* 2015). These studies report foam rheology measurements performed in bulk foam (Xing *et al.*, 2010), or by flow experiments in porous media such as cylindrical cores (McLendon *et al.*, 2012; Xing *et al.*, 2012) and sand packs (Chen *et al.* 2015; Adkins *et al.* 2010a). The experimental results from these studies are challenging to generalize and compare due to variations in rheology measurements, such as varying flow velocity, gas fractions and non-comparable porous media. The injection schemes employed in the studies are insufficient for calibrating empirical foam models, and saturation measurements were not performed. This thesis presents a comprehensive experimental dataset of foam flow characteristics using five different non-fluorinated non-ionic surfactants that partition between CO_2 and water. Both steady-state co-injection foam experiments (Paper 4), applicable for calibration of empirical foam models, and unsteady-state foam experiments, revealing foam generation and decay characteristics, are presented (Paper 2). The five surfactants are compared with experimental results obtained using the Alpha olefin sulfonates (AOS) surfactant, which can be considered a benchmark surfactant due to its excellent foaming properties (Farajzadeh *et al.*, 2008; Farajzadeh *et al.*, 2011; Jones *et al.*, 2016).

Pore-scale foam dynamics were investigated using micromodels (Paper 1), corroborating core flooding experiments (Paper 2,3 & 4). Foams are commonly stabilized using surfactants, although nano-particles have also recently been considered as foaming agents (Rognmo *et al.* 2017; Nguyen *et al.* 2014). A study hybrid surfactant-nanoparticle foaming agent solutions and the effect of residual oil saturation was performed (Paper 3). The pore-scale foam dynamics study (Paper 1) and hybrid surfactant-nanoparticle foaming agent study (Paper 4) used the Surfonic L24-22 surfactant, with and without nano-particles added to the foaming agent formulation. The Surfonic L24-22 surfactant is chemically similar to one of the five non-ionic surfactants

(Brij L23) used in Papers 2 & 4. Both surfactants are linear ethoxylated alcohol, with the same carbon number (12-14) and similar ethoxylation (23 and 22).

Foam injection strategies

To form foam during field-scale application, surfactant and gas must be simultaneously present in the same location. Surfactant distribution in the reservoir partially depend on the surfactant injected. Surfactant which are only solvable in water can potentially segregate from the less dense gaseous phase. Some reservoir zones can end up with inadequate surfactant concentrations to generate stable foam due to gravity segregation (Vassenden *et al.* 1999). Segregation of the injected surfactant can be mitigated by using surfactants soluble and transportable by both the aqueous and gaseous phase (Zeng *et al.* 2016), which could improve the distribution of surfactant in the reservoir. Surfactants soluble in both the aqueous and gaseous phase also provides flexibility in field-scale foam injection design. Water-soluble surfactants are limited to two injection strategies:

i) Continuous foam injection. Surfactant solution and gas is co-injected.
ii) Surfactant-Alternating-Gas (SAG). Surfactant solution and gas is alternately injected in successive slugs.

Three additional injection strategies have been proposed for surfactant partially soluble in the gaseous phase:

iii) Water-Alternating-Gas-with-Surfactant-in-Gas (WASG) (Le *et al.* 2008)
iv) Continuous Surfactant-Gas injection (SG) (Le *et al.* 2008).
v) Pre-injection of concentrated aqueous surfactant solution (Grimstad *et al.* 2018)

All five strategies can be employed when the surfactant is soluble in both phases. Co-injection (i) is rarely considered due to operational constraints and potential injectivity issues (Rossen *et al.* 1995), whereas SAG (ii) has been employed in several field-scale pilot test (Chou *et al.* 1992; Hoefner & Evans 1995; Henry *et al.* 1996; Blaker *et al.* 1999). In SAG, foam will be weakened near the injection well, mitigating the injectivity issues. WASG (iii) is similar to SAG, but the surfactant is dissolved in gas (CO_2) prior

to being injected, to facilitate improved surfactant distribution into the reservoir (Le *et al.* 2008). During SAG and WASG, the gas injections will temporarily be halted by the aqueous injection cycles. During WASG, injected water will also occupy potential storage volume, making SG (iv) more appealing (water-injection cycles are not performed). SG, however, relies on the water present in the reservoir to form foam, thus the gas-soluble surfactant must be able to generate and stabilize foam at low water saturations. Pre-injection (v) of concentrated aqueous surfactant solution simplifies field operations but relies on partitioning of surfactant from the pre-injection surfactant solution to the injected gas (CO_2) for efficient distribution into the reservoir. Partitioning requires the gas (CO_2) to come in contact with the aqueous surfactant solution and may be influenced by e.g. gravity segregation.

2.1 Reduction in CO_2 mobility

The structure of foam in porous media differs from that of "bulk" foams, commonly encountered in householding, as it is affected by walls in the confined pore space. Foam in porous media consists of lamellae that separate the gaseous phase into discontinuous bubbles. Generally, the bubble size exceeds the pore size, and the lamellae span entire pores. The lamellae impede the gas flow, reducing the effective gas-foam relative permeability (k_{rg}^{f*}) and increasing the effective gas-foam viscosity (μ_g^f). The mobility of the gas phase is, therefore, effectively reduced (see Eq. 1). The aqueous phase, which remains continuous, is unaffected by foam (Kovscek & Radke 1994). The combined effect of reduced effective gas-foam relative permeability and increased the effective gas-foam viscosity can be assessed by adapting Darcy's law for foam flow (Kovscek & Radke 1994):

$$u_g = \frac{k k_{rg}^{f*} \nabla \mathrm{p_g}}{\mu_g^f} \tag{3}$$

where u_g is the superficial gas flow velocity, k is the absolute permeability, and ∇p_g is the gas pressure gradient. Evidently, k_{rg}^{f*} and μ_g^f are tied to each other through Darcy's

law and cannot be determined independently from pressure gradient measurements (∇p_g), i.e. during core flooding experiments.

The increase in effective gas-foam viscosity μ_g^f is caused by the viscous shear associated with lamellae moving along pore walls (Hirasaki & Lawson 1985) and through pore throats (Falls *et al.* 1989). The gas-foam effective viscosity is proportional to the flowing foam bubble density (n_f) (Fried 1961; Kovscek & Radke 1994), and is shear-thinning with respect to interstitial velocity (v_f). This relation can be described by (Kovscek *et al.* 1995):

$$\mu_g^f = \mu_g + \alpha * \frac{n_f}{v_f^c} \tag{4}$$

where μ_g is the gas viscosity, α is a system dependent scaling constant and c has been estimated to be approximately $1/3$ (Hirasaki & Lawson 1985).

Trapped stationary foam reduces the effective gas-foam relative permeability k_{rg}^{f*}. The three-phase relative permeability model by Stone (1970) is applicable when describing the reduction in gas effective permeability by foam (k_{rg}^{f*}). By considering flowing foam (S_{fg}) and trapped foam (S_{tg}) as two pseudo saturations, in addition to the water saturation (S_w), we have a three-phase system. Water, being the most wetting phase occupies the smallest pores, whereas flowing foam will occupy the largest pores (Radke & Gillis 1990), illustrated in (**Fig. 2**). Stone's model for relative permeability states; the relative permeability of the least (S_{fg}) and most wetting phase (S_w) depends only on its own saturation, and is the same as their respective two-phase relative permeability. Conveniently, the intermediate saturation is the trapped foam (S_{tg}), with a relative permeability of zero. Therefore, the gas-foam relative permeability (k_{rg}^{f*}) equals the no-foam gas relative permeability at the flowing gas saturation S_{fg} (Kovscek & Radke 1994).

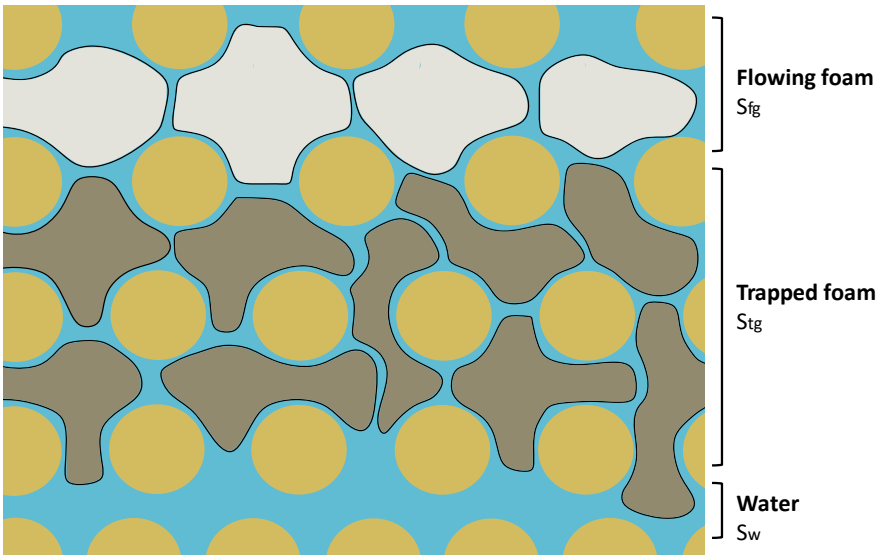

Fig. 2: Pore-level schematic illustration of flowing and trapped foam. Flowing discontinuous foam bubbles are colored white and located in the largest pores. Trapped foam bubbles are colored brown and are located in the intermediate-sized pores. The aqueous phase, colored blue, wets the surface of the yellow spherical rock grains and occupies the smallest pores. Modified from Radke & Gillis (1990).

2.2 Foam generation and coalescence

Foam generation can be defined as when the rate of lamella (bubble) creation exceeds the rate of lamella destruction by coalescence mechanisms. Increased bubble density during foam generation will reduce the mobility of gas. The terms "strong" and "weak" foam is extensively used in the literature to describe the mobility reduction state of the foam. However, these two states are not clearly defined, and "weak foam" can result from insufficient foam generation or by rapid destruction of unstable foam. At steady-state foam flow, the kinetics of foam generation and coalescence is at equilibrium, causing the bubble density and mobility reduction of gas to be fixed.

The three most recognized foam generation mechanisms are *Snap-off*, *Lamella mobilization/division* and *Lamella leave-behind* (Kovscek *et al.* 2007; Chen *et al.* 2005; Rossen 2003; Ransohoff & Radke 1988), illustrated in (Fig. 3). *Snap-off* occurs when gas is pushed through a liquid lens located at a pore-throat, and then "snaps off". The

process depends on the local capillary pressure, facilitating the liquid lens to recur at the pore-throat. *Lamella mobilization and division* occurs at pore-branch points, where single lamella can be divided into more lamellae. Both *Snap-off* and *Lamella mobilization and division* result in a "strong" foam, where lamellae are oriented perpendicular to the flow direction and effectively impede flow (Kam & Rossen 2003). *Lamella leave behind* results in lamellae oriented parallel to the flow direction, resulting in an "weaker" foam, as the gas phase is continuous (Kovscek & Radke 1994; Friedmann *et al.* 1991).

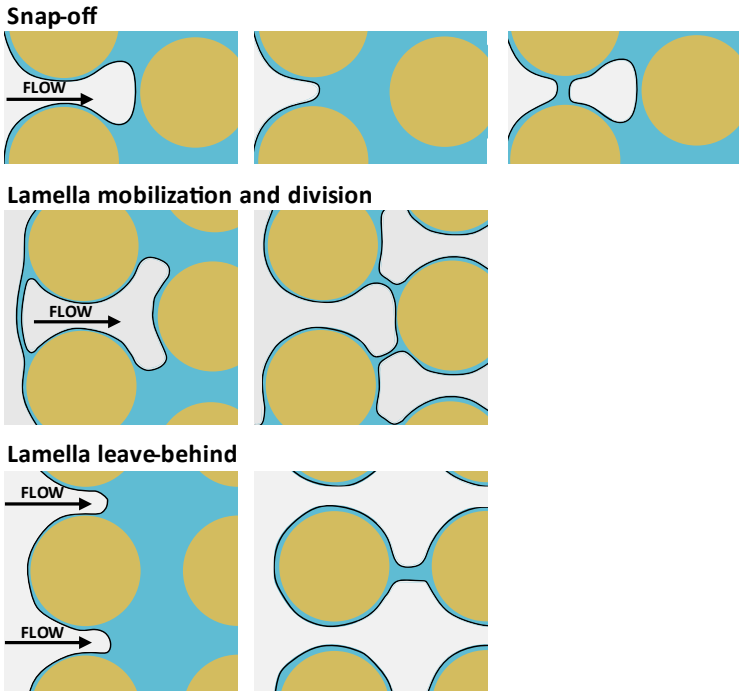

Fig. 3: **Pore-level schematic illustration of foam generation mechanisms. The arrows indicate flow direction, the gaseous phase is colored white, the aqueous phase is colored blue and spherical rock grains are colored brown. Modified from Kovscek &Radke (1994).**

Generation of strong foam requires minimum threshold pressure gradients (or minimum flow velocities) to be exceeded (Ransohoff & Radke 1988; Rossen & Gauglitz 1990; Kovscek & Radke 1994; Gauglitz *et al.* 2002). The minimum threshold pressure gradients might be related to mobilization and division of an initial population of

lamellae (Rossen & Gauglitz 1990), or the capillary entry pressure needed to be exceeded for *Snap off* to occur in narrow pore throats (Ransohoff & Radke 1988). The existence of minimum pressure gradients could affect field-scale application of foam, as sufficient pressure gradients might only be exceeded near the injection well. Foam can be generated by *Snap-off* independently from pressure gradients at sharp transitions in permeability (Rossen 1999; Shah *et al.* 2019).

Foam coalescence destroys foam bubbles, which reduces the bubble density and consequently counteract gas mobility reduction. Coalescence can be caused by three mechanisms within porous media: coarsening by diffusion (Ostwald ripening), capillary suction drainage, and gravitational liquid drainage (Kovscek & Radke 1994). Coarsening by diffusion occurs by transport of gas from smaller bubbles (small radius, high curvature), and thereby a higher internal pressure, to larger bubbles with lower internal pressure, with the consequence that smaller bubbles disappears (Marchalot *et al.* 2008; Saint-Jalmes 2006). Capillary suction drainage occurs when the water saturation approaches a saturation value where the lamellae are no longer stable, as the capillary pressure exceeds the disjoining pressure and drains the lamellae (Farajzadeh *et al.* 2015; Falls *et al.* 1989). Capillary suction drainage causes two distinct foam flow regimes, further described below.

2.3 Flow regimes

Foam characterized as "strong" can be separated into two distinct regimes based on the gas fraction (f_g) , the low-quality and high-quality regime.

$$f_g = \frac{u_g}{u_g + u_w} \tag{5}$$

Where u_g and u_w is the superficial flow velocity for gas and water, respectively.

During steady-state flow of gas and water (no foam) an increase in the gas fraction will be accommodated by a change in both gas and water mobilities. The change in mobility occurs by a reduction in water saturation and subsequent increase in capillary pressure

(Valavanides 2018). However, an increase in gas fractional flow will not necessarily lead to a reduction of water saturation during steady-state foam flow.

At lower gas fractions, foam is in the low-quality regime, where foam exhibiting a shear-thinning behavior (Rossen & Wang 1999). Falls *et al.* (1989) postulated that any foam film (lamella) in a porous medium can withstand a maximum pressure drop. During foam flow in the low-quality regime, the pressure gradient will adjust to the maximum pressure drop that the foam films can withstand, termed the limiting pressure gradient (Vassenden & Holt 2000). This implies that the pressure gradient should be independent of the flow rate and that the gas relative permeability increases linearly with the flow rate, causing the shear thinning behavior (Rossen & Wang 1999).

At high gas fractions foam, is in the high-quality regime, where the water saturation is insensitive to changes in gas fraction (Vassenden & Holt 2000). The water saturation will approach a saturation value, denoted the foam breakdown saturation, S_w^*, where the corresponding capillary pressure, denoted the limiting capillary pressure (P_c^*), is close to the maximum disjoining pressure of the foam film (lamella). A minute increase in the capillary pressure will drain water from the foam films, and subsequently cause rupture (Falls *et al.* 1989; Farajzadeh *et al.* 2015). Any increase in gas fraction within the high-quality regime will, therefore, lead to virtually no changes in water saturation.

2.4 Modelling

Numerous foam models that use core-scale laboratory data to evaluate field-scale foam behavior are described in the literature and summarized by Ma *et al.* (2015) and Lotfollahi *et al.* (2016). There are two primary foam modeling approaches; population-balance foam models and local-equilibrium foam models. Population-balance foam models track the conservation of foam texture, i.e., bubble density (n_f), and the fraction between trapped and stationary foam to calculate gas mobility (Kovscek *et al.* 1995). Local-equilibrium models assume instantaneous foam properties (fixed foam texture) and are therefore less dynamic than population balance models, but require fewer parameters (Ma *et al.* 2015). Local-equilibrium models commonly modify the no-foam

gas relative permeability (k_{rg}) by a factor FM, inversely proportional to the mobility reduction factor (MRF) (Ma *et al.* 2015; Vassenden & Holt 2000; Cheng *et al.* 2000).

$$k_{rg}^{f}(S_w) = k_{rg}(S_w) * FM \quad (6)$$

where k_{rg}^{f} is the foam gas relative permeability at a water saturation S_w.

Three physical features of foam are important to observe in the experimental dataset and should be captured by the foam model:

i) The high- and low-quality regimes, separated by the transition gas fraction, where the mobility reduction of foam is largest.

ii) The shear-thinning behavior in the low-quality regime, due to the limiting pressure gradient (Rossen & Wang 1999).

iii) The abrupt reduction in foam strength in the high-quality regime, due to high capillary pressure (Falls *et al.* 1989).

Depending on the selected foam model, additional influencing factors on foam can be captured, such as: surfactant concentration, salt concentration, permeability, oil saturation and composition (Ma *et al.* 2015).

2.5 Common parameters

The various parameters used to quantify experimental foam data and their relationship often causes confusion and misunderstandings. This summary is, therefore included:

As previously discussed, foam influences both the effective gas-foam relative permeability (k_{rg}^{f*}) and the effective gas viscosity (μ_g^f). These parameters are, however, tied to each other through Darcy's law and cannot be determined independently from pressure gradient measurements (∇p_g). Commonly, either the viscosity or relative permeability is modified to capture the effect of foam in modeling or for quantitative comparison purposes.

Most quantification of foam strength relies on measured pressure gradients (∇p_g). The pressure gradient itself is the most straightforward quantitative assessment; however, the pressure gradient depends on flow velocity (u) and absolute permeability (k), and lack generality, often making it unsuitable for comparison purposes. Foam apparent viscosity (μ_{app}) accounts for differences in core permeability and flow velocity and is more commonly reported:

$$\mu_{app} = \frac{k}{u} * \nabla p_g \tag{7}$$

Mixing foam apparent viscosity (μ_{app}) with foam effective gas viscosity (μ_g^f) is a common pitfall. The foam effective gas viscosity is the viscosity of the flowing bubble trains, whereas the foam apparent viscosity is proportional to the pressure gradient (Equation 7), which also includes the effect of reduced effective gas-foam relative permeability (k_{rg}^{f*})(see Equation 3).

Foam apparent viscosity only relies on pressure gradients, without considering differences in saturation. The mobility reduction factor (MRF) may instead be used to compare the gas relative permeability, as a function of water saturation, in the presence of foam ($k_{rg}^f(S_w)$) with the gas relative permeability in the absence of foam ($k_{rg}(S_w)$). MRF is defined as:

$$MRF = \frac{k_{rg}(S_w)}{k_{rg}^f(S_w)} \tag{8}$$

The gas relative permeability in the absence (k_{rg}) and presence of foam (∇p_g) can be calculated from pressure gradients using the Darcy equation:

$$k_{rg} \; and \; k_{rg}^f = \frac{u_g * \mu_g}{\mathrm{k} * \nabla p_g} \tag{9}$$

When assuming negligible capillary pressure the gas pressure gradients (∇p_g) equals the measured pressure gradient (∇p).

MRF requires saturation measurements, which can be challenging to obtain with sufficient accuracy. Saturation measurements are also required for accurate foam modeling, and the output parameter (FM, see Equation 6) of several local-equilibrium foam models is the inverse of MRF.

Due to the importance of locating the high- and low-quality foam regime, steady-state co-injection foam experiments are commonly performed using a range of gas fractions. The data from steady-state co-injections are often reported as the foam apparent viscosity (μ_{app}) versus gas fraction (f_g) curves. Local-equilibrium foam models commonly modify the gas-relative permeability versus water saturation curves ($k_{rg}^f(S_w)$) (Equation 6) to capture the reduction in gas mobility by foam. Conversion between the two types of curves (apparent viscosity (μ_{app}) vs. gas fraction and gas-relative permeability vs. water saturation) are therefore often needed and are performed using the Buckley-Leverett equation for fractional flow:

$$f_g = 1 - \frac{1}{1 + \frac{k_{rg}^f * \mu_w}{\mu_g * k_{rw}}} \tag{10}$$

The apparent foam viscosity can be calculated as:

$$\mu_{app} = f_g * \frac{\mu_g}{k_{rg}^f} \tag{11}$$

3. Experimental summary

The laboratory experiments presented in this thesis were performed at two different length scales; the pore- and the Darcy-scale. Exact limitations are not clearly defined for each scale, however, "pore-scale" implies inter-pore measurements and observations, whereas "Darcy-scale" implies sufficient sample size that momentum balance calculation can be performed using the Darcy equation. Darcy-scale measurements are commonly obtained using cylindrical rock cores ranging from centimeters to meters in length, and may also be referred to as "core-scale". The porous material used was comparable for both scales: Bentheimer sandstone outcrop cores were used for the Darcy-scale experiments, whereas etched silicon wafer micromodels with a porous pattern representative of sandstone rock were used for the pore-scale experiments. Details regarding the production of the micromodels can be found in (Buchgraber *et al.* 2012). The chemical characteristics of the two materials (crystalline silicon and quartz) are similar and chemically inert to all injected fluids in this thesis. Dense CO_2 (ρ>0.80 g/ml) was used in all experiments.

Micromodel experiments

The foam experiments performed in the etched silicon wafer micromodel gave direct visual observation of CO_2 foam dynamics in porous media, constituting the pore-scale foam observations. The micromodel experiments were performed at 100 bar pore-pressure and 20 °C. Software for analyzing the micromodel images was developed together with Benyamin Benali and is described in Benali (2019). Additionally, necessary equipment for performing the micromodel experiments was designed as a part of the project, which includes: PEEK micromodel holder, flow-rig with low dead volumes, and backpressure regulation system.

Core flooding experiments

Darcy-scale foam experiments were obtained using Bentheimer sandstone cores. The Darcy-scale experiments were performed at 200 bar pore-pressure and 40 °C. The sandstone cores and the micromodel were used for several foam injections and cleaned

using organic solvents between foam injections. Permeability measurements were regularly performed, and no significant changes were observed.

Foam injection schemes

Two types of foam injections were employed: steady-state co-injection and unsteady-state injection. Baseline and reference experiments, without foaming agent added to the aqueous solution, were performed in addition to the foam injections. Steady-state co-injections were performed by simultaneous injection of CO_2 and foaming agent solution while varying the CO_2 fraction and flow velocity (Paper 4). Steady-state co-injections were only performed in Bentheimer sandstone cores, where steady-state foam characteristics were recorded at constant pressure gradient and saturation. The main motivation was to obtain measurements of gas mobility reduction by foam at various flow conditions. The results may be used as input to empirical foam models. Unsteady-state foam injections were performed by injection of CO_2 into Bentheimer sandstone cores (Paper 2 & 3) or micromodel pre-saturated (Paper 1) with foaming agent solution to investigate foam generation and decay. At the Darcy-scale foam generation can be recognized as an increase in foam apparent viscosity. Whereas, at the pore-scale, foam generation is directly observed as an increase in the number of bubbles, i.e., a change in foam-texture.

4. Results and discussion

This chapter summarizes the findings in Paper 1-5 and constitutes a multi-scale investigation of foam for CO_2 mobility control stabilized using non-ionic surfactants. The study includes investigations from pore-scale foam dynamics to field-scale implementation of CO_2-foam. The section is organized by subjects to discuss general findings across several publications.

4.1 Foam generation

Foam generation was studied during unsteady-state CO_2 injection at pore- and core-scale using micromodels (Paper 1) and core samples pre-saturated with foaming agent solution (Paper 2). At the Darcy-scale foam generation can be recognized as an increase in foam apparent viscosity, whereas at the pore-scale, foam generation is directly observed as an increase in the number of bubbles, i.e., a change in foam-texture.

4.1.1 Pore-scale visualization of foam generation

Pore-scale foam generation was observed in micromodels during unsteady-state performed at a constant CO_2 flow rate (4 $\mu L/min$) (Paper 1). High-resolution images (4 $\frac{\mu m}{pixel}$), were captured during CO_2 injections within a large field of view (22 X 26 mm). Image analysis software was developed to characterize and count foam bubbles as a function of time.

Foam generation dominated the initial part of the CO_2 injection, visible by a sharp increase in the number of bubbles: up to 40 times the number of bubbles recorded during baseline injection (Fig. 4). After approximately 5 PV of CO_2 injected, the number of bubbles started to decrease.

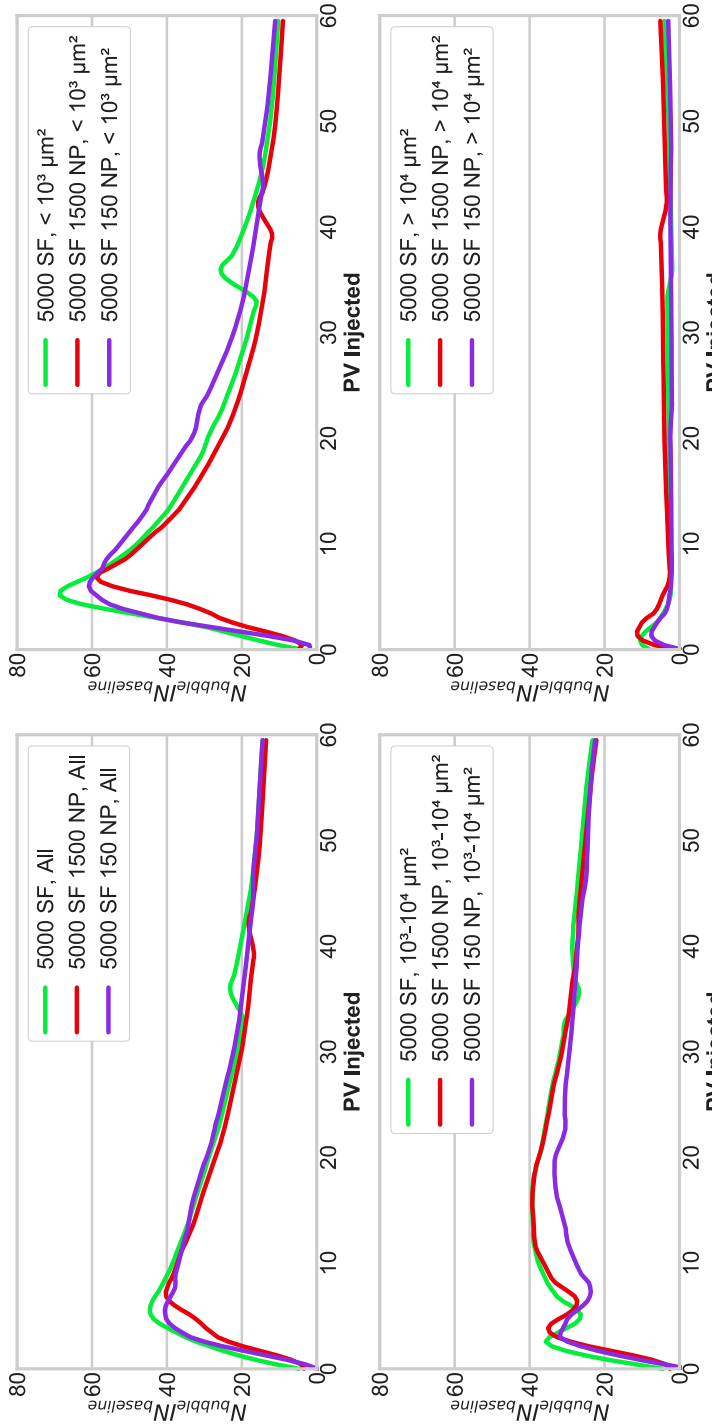

Fig. 4: Development in bubble number (normalized with respected to the baseline). The bubbles are sorted into logarithmical bubble size groups: Upper-right shows small bubbles ($< 10^3 \mu m^2$), lower-left shows intermediate bubbles ($10^3 - 10^4 \mu m^2$), lower-right shows large bubbles ($> 10^4 \mu m^2$). Upper-left includes all bubbles. Sorting the number of bubbles based on size shows that the number of intermediate size bubbles are increasing at the expense of small bubbles after 5 PV of CO_2 injection.

Bubble density maps (Fig. 5) show the distribution of foam bubbles in a micromodel, and revealed that foam generation primarily occurred by snap-off in the vicinity of a sharp permeability contrast. Foam generation, although initially low, increased rapidly when the injected CO_2 reached the boundary of the porous pattern. This boundary represents a sharp contrast in permeability and, therefore, a favorable location for snap-off (Rossen 1999; Shah *et al.* 2019). Fining of the foam texture occurred by backward propagation (from outlet to inlet), increasing the foam strength. Backward propagation fining was also previously reported (Simjoo & Zitha 2020; Almajid *et al.* 2019; Apaydin & Kovscek 2001), but the mechanisms are not clear. Foam transitioning from a weak to a strong foam state, or favorable conditions for snap-off in the transition zone have been proposed, but not supported (nor discarded) by the current observations. Backward propagation of the foam front indicated that snap-off was the prevailing foam generation mechanism because lamella mobilization and division require foam to be present up-stream and can only result in co-current propagation of foam.

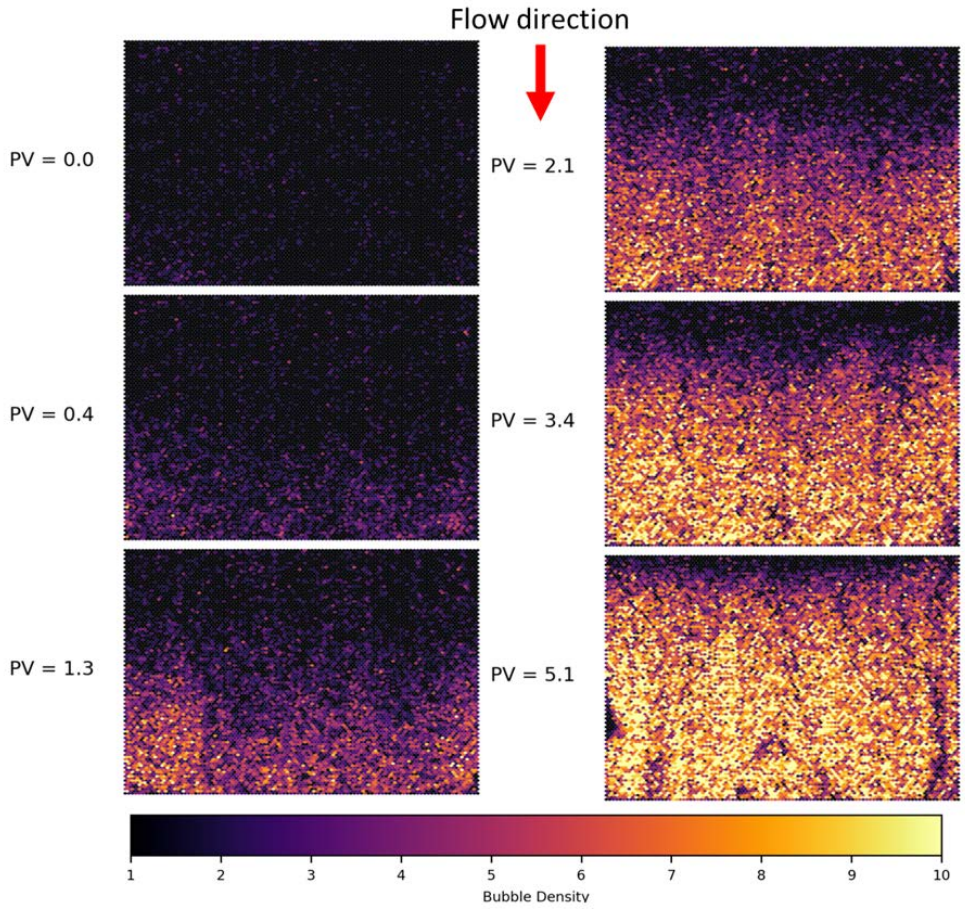

Fig. 5: Bubble density mapping shows foam generation during unsteady-state CO_2 injection in micromodel pre-saturated with SF5000 foaming agent solution. Foam generation initiated between 0.4 and 1.3 PV of CO_2 injected at the sharp permeability contrast between the porous pattern and outlet flow channel (bottom side of the density maps). Foam density was initially higher (brighter color) at the outlet side of the micromodel, but propagated backwards (outlet to inlet) to increase foam density throughout the micromodel. The resolution of the spatially resolved hexagonal binning plot is 150 X 90.

4.1.2 Darcy-scale foam generation

Foam was generated and foam apparent viscosity increased when CO_2 was injected and advanced through cores pre-saturated with foaming agent solution. During foam decay, the foam apparent viscosity decreased, i.e., the overall trend in foam apparent viscosity development resembles the pore-scale development in the number of bubbles during

unsteady-state foam injection. Three distinct categories of foam generation were defined based on the apparent viscosity (build-up of foam in the core) development versus time (pore volumes of CO_2 injected): Linear, Super-linear and Delayed (Paper 2).

Linear foam generation (a linear relationship between apparent viscosity and injected pore volumes of CO_2, Fig. 6) indicates that foam is generated close to the saturation front where injected CO_2 displaces foaming agent solution and remains stable behind the front. The gradient of the apparent viscosity curves (how fast the apparent viscosity increased) was found to depend on the CO_2 flow velocity. Linear foam generation was observed for sandstone saturated by foaming agent Brij L23 (Fig. 6), where one distinct slope (11 cP/PV) was observed at a low CO_2 flow velocity (2.1 ft/day) and two distinct slopes were observed when CO_2 flow velocity was initially high (slope of 43 cp/PV at 32.5 ft/day) and subsequently reduced (slope of 7 cP/PV at 2.1 ft/day).

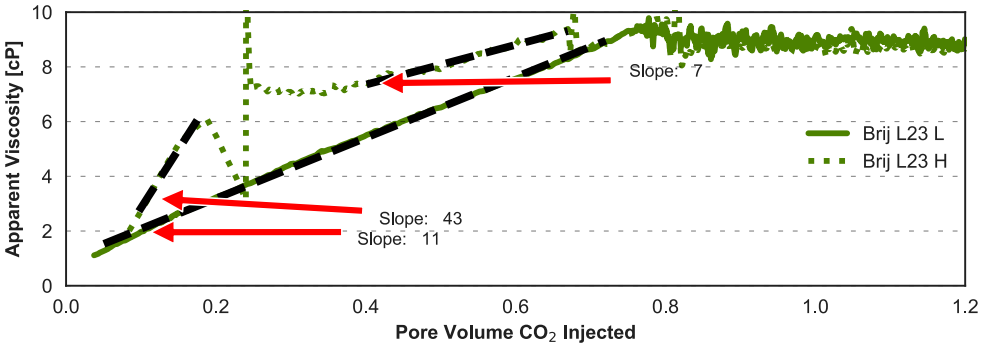

Fig. 6: **Foam generation at the Darcy-scale, shown by development in apparent viscosity during unsteady-state CO_2 injection. The linear foam generation slopes are marked by dashed lines. "L" and "H" denotes low and high flow velocities, respectively.**

Super-linear foam generation (a steepening apparent viscosity versus injected pore volumes of CO_2) is likely caused by a positive feedback process. Foam strength depends on the pressure gradient, simultaneously, the pressure gradient increases with increasing foam strength, and a positive feedback loop can occur. When a minimum pressure gradient is exceeded, the feedback loop may be self-sustained. Linear and Super-linear foam generation was observed using AOS surfactant (Fig. 7), depending on the CO_2 flow velocity. Linear foam generation was observed when CO_2 flow velocity was low

(2.1 ft/day), and Super-linear foam generation was observed using a high initial flow velocity (32.5 feet/day) during the first 0.25 PV injected. This observation indicates that the minimum required pressure gradient and a self-sustained feedback loop was achieved at high flow velocity, but not at low. The maximum foam strength (highest observed foam apparent viscosity) was higher during Super-linear foam generation; the foam generated at high flow velocity was 17 times stronger than foam generated at low flow velocity for the AOS surfactant.

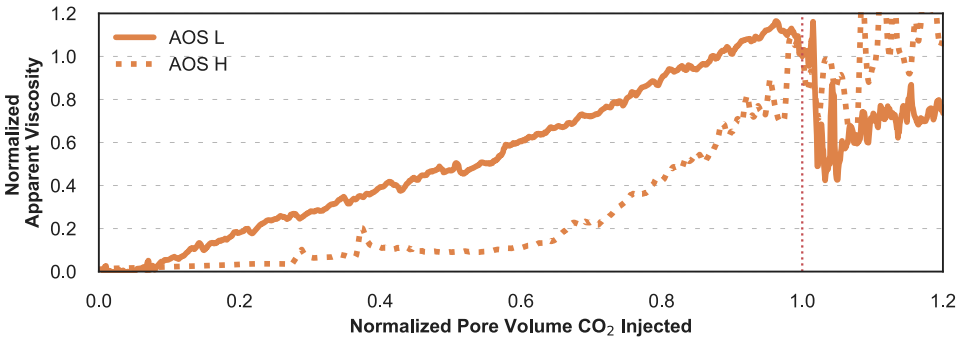

Fig. 7: **Foam generation was both linear (L) and super-linear (H) when sandstone was saturated by AOS surfactant before CO_2 injection. Apparent viscosity and pore volumes of CO_2 injected are normalized with respect to the values at gas break through.**

Delayed foam generation (apparent foam viscosity increases abruptly and rapidly after an extended period of CO_2 injection) indicates that foam is not generated continuously at the saturation front during CO_2 injection. *Delayed* foam generation was observed when sandstone was pre-saturated with foaming agent solutions Tergitol NP10 and Tergitol TMN10. The increase in apparent viscosity deviated from the linear and super-linear foam generation categories, as foam generation occurred abruptly and rapidly after an extended period of CO_2 injection (Fig. 8).

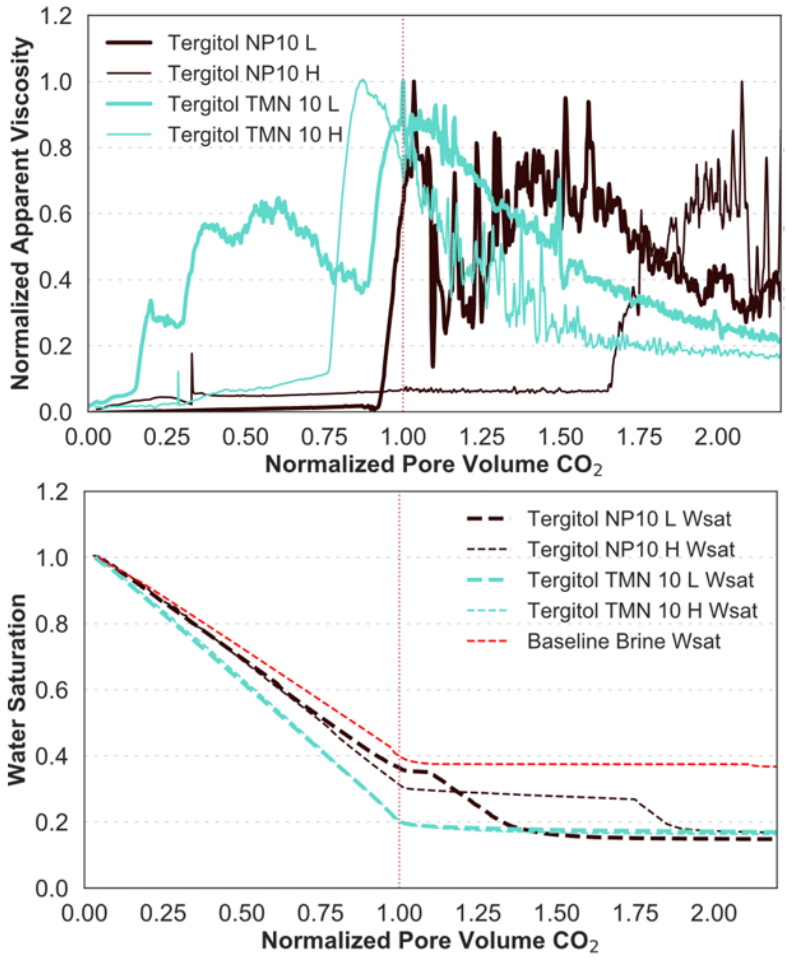

Fig. 8: **Delayed foam generation was observed during unsteady-state CO_2 injection into sandstone pre-saturated by surfactants Tergitol NP 10 and Tergitol TMN 10. The top figure shows apparent viscosity normalized to peak apparent viscosity, and the bottom figure shows water saturation development. The x-axes are shown as functions of normalized time (PV CO_2 injected normalized to gas breakthrough). Gas breakthrough (1 PV) is indicated by the vertical red line. The water saturation profile for baseline CO_2 injection (no surfactant) is included for comparison.**

The categories of foam generation could be connected to the characteristics for the different foaming agent solutions (summarized in Table 1):

i) The an-ionic AOS surfactant (Fig. 7) exhibited both Linear and Super-linear foam generation, depending on initial flow conditions.

ii) Different foam generation categories were observed for the five non-ionic surfactants (Linear, Super-linear, and Delayed), however, the foam generation category did not depend on initial flow conditions

Table 1. Foam generation categories for the foaming agent solutions during unsteady-state foam floods. The table includes the highest measured apparent viscosity for each foam flood (peak foam strength).

Foaming agent	Flow velocity	Foam category	App visc. [cP]
An-ionic, non CO_2-soluble			
AOS	L	Linear	7
	H	Super-linear	122
Non-ionic, partially CO_2-soluble			
Tergitol 15-S-9	L		2.2
	H		1.2
Igepal CO-720	L	Super-linear	80
	H	Super-linear	21.3
Brij L23	L	Linear	9.5
	H	Linear	10
Tergitol TMN 10	L	Delayed	24
	H	Delayed	52
Tergitol NP10	L	Delayed	100
	H	Delayed	86

4.2 Foam Decay

Foam decay was studied during unsteady-state CO_2 injection at pore- and core-scale using micromodels (Paper 1) and core samples pre-saturated with foaming agent solution (Paper 2 & 3). At the Darcy-scale foam decay can be recognized as a decrease in foam apparent viscosity. At the pore-scale foam decay can be directly observed as a decrease in the number of bubbles and simultaneous formation of open gas channels.

4.2.1 Surfactant stripping

The degree of CO_2 solubility (partitioning coefficient, kp) of non-ionic surfactants (used as foaming agents, Paper 2 & 4) is of special interest for foam decay. Surfactant stripping, where the surfactant concentration in the brine decreases due to mass transfer into the flowing CO_2, leads to a continuous reduction in surfactant concentration during CO_2 injection. A reduction in surfactant concentration is expected to contribute to foam decay, as foam strength relates to surfactant concentration. A simplified model (described in Paper 2) estimated and compared the continuous reduction in surfactant concentration with the development in apparent viscosity during CO_2 injection (Fig. 9). Foam decay observed in experiments was generally much slower than the estimated reduction in surfactant concentration, indicating that surfactant adsorbed to fluid interfaces and rock surfaces slowed the depletion of surfactant and, hence, foam decay. Therefore, foam generated by partially CO_2-soluble surfactants was found to be more efficient than expected in reducing and maintaining low gas mobility.

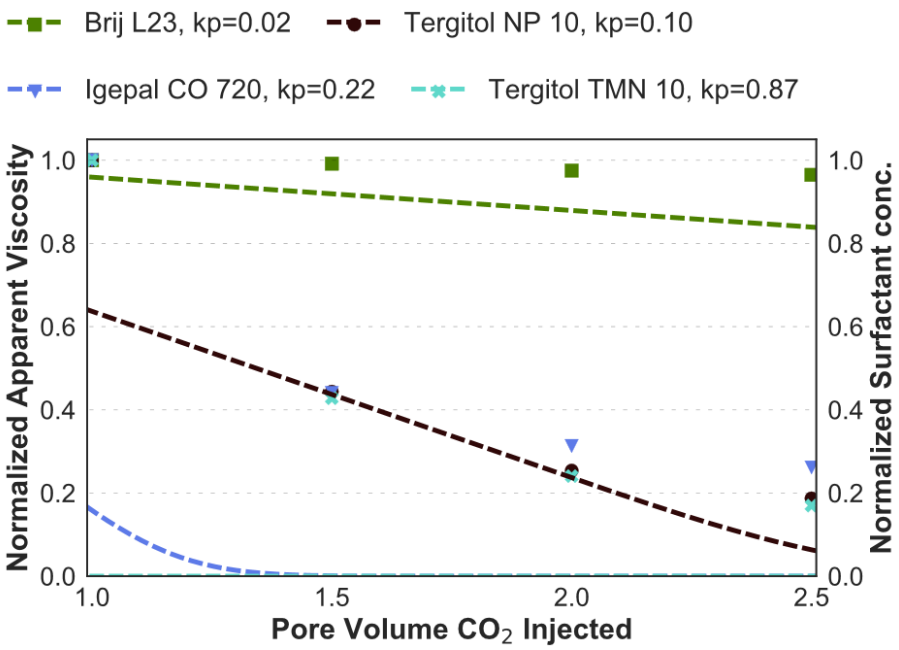

Fig. 9: Comparison between calculated surfactant concentrations using the surfactant mass balance model (dashed lines; normalized to concentration at CO_2 breakthrough) and measured apparent viscosity (points; normalized to the values measured at 1 PV injected).

4.2.2 Pore-scale foam decay

CO_2 flow through the pre-saturated micromodel occurred by moving bubble trains and open gas channels within flowing regions. The movement of bubble trains occurred with temporary flow suspension, restart, and irregular relocation (Fig. 10). The open gas channels extended several pore lengths and occurred by inadequate regeneration of foam. Open gas channels were irregularly filled with bubbles and reemerged in the same or new locations, exemplified in Fig. 9. Stationary foam close to open or partially filled channels changed from low energy configuration (no curvature, image A) to texture with less capillary resistance (with curvature, images C and D). Supporting that lamella located at lower energy configuration (at rest) will have a greater capillary resistance to remobilization (Jones *et al.* 2018a; Hou *et al.* 2013). Hence, when exposed to the same pressure gradient, lamella in stationary regions will not move, whereas lamella in the flowing region will move.

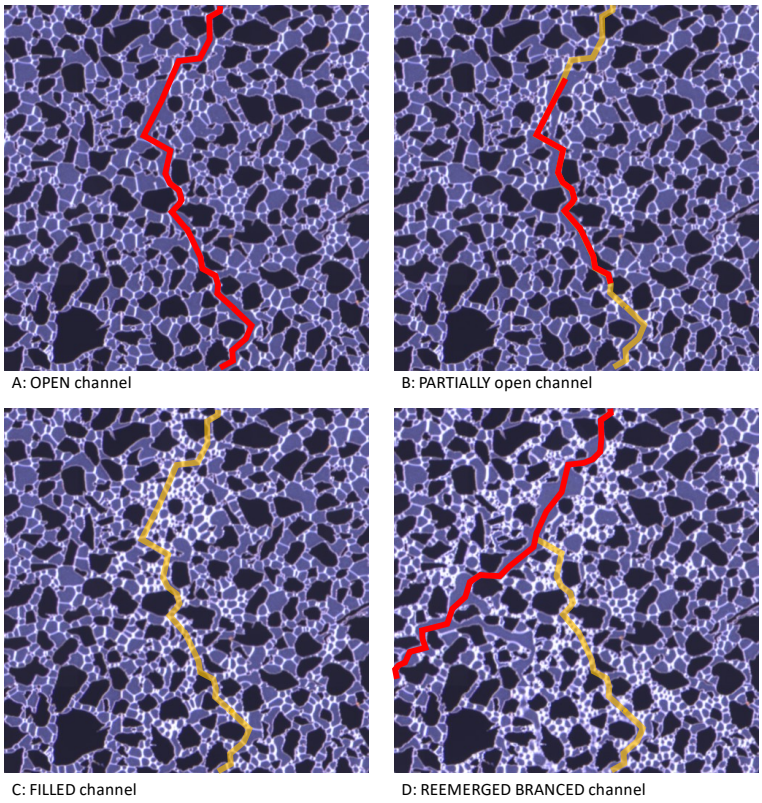

Fig. 10: Dynamics of open gas channels during bubble generation: red indicates path of an open channel (without bubbles) and orange indicates where the open channel is filled with bubbles. Sequential images show: a) path of an open channel (t = 33.8 PV); b) channel becomes partially open (t = 34.2 PV); c) channel becomes filled with bubbles (t = 34.7 PV); d) a new path emerge that branches from the original path, now partially filled with bubbles (t = 35.1 PV). The images are from the SF5000 injection at the same field of view (2.2 mm x 2.2 mm).

Hexagonal binning plots (Fig. 11) were used to map dynamic changes in bubble density, open gas channels, flowing bubbles and stationary bubbles. Flowing regions were identified by temporal changes in bubble position and size. Stationary regions were characterized by trapped bubbles (no temporal change in position and size) and were spatially resolved (Fig. 11) by combining the bubble density map and temporal changes: *trapped = density / (temporal changes +1)*. Open gas channels were defined as large bubbles exceeding a size of 25% of micromodel length. Flowing region and the open gas channels were based on observations between 5 image frames, corresponding to 1.7 PV CO_2 injected.

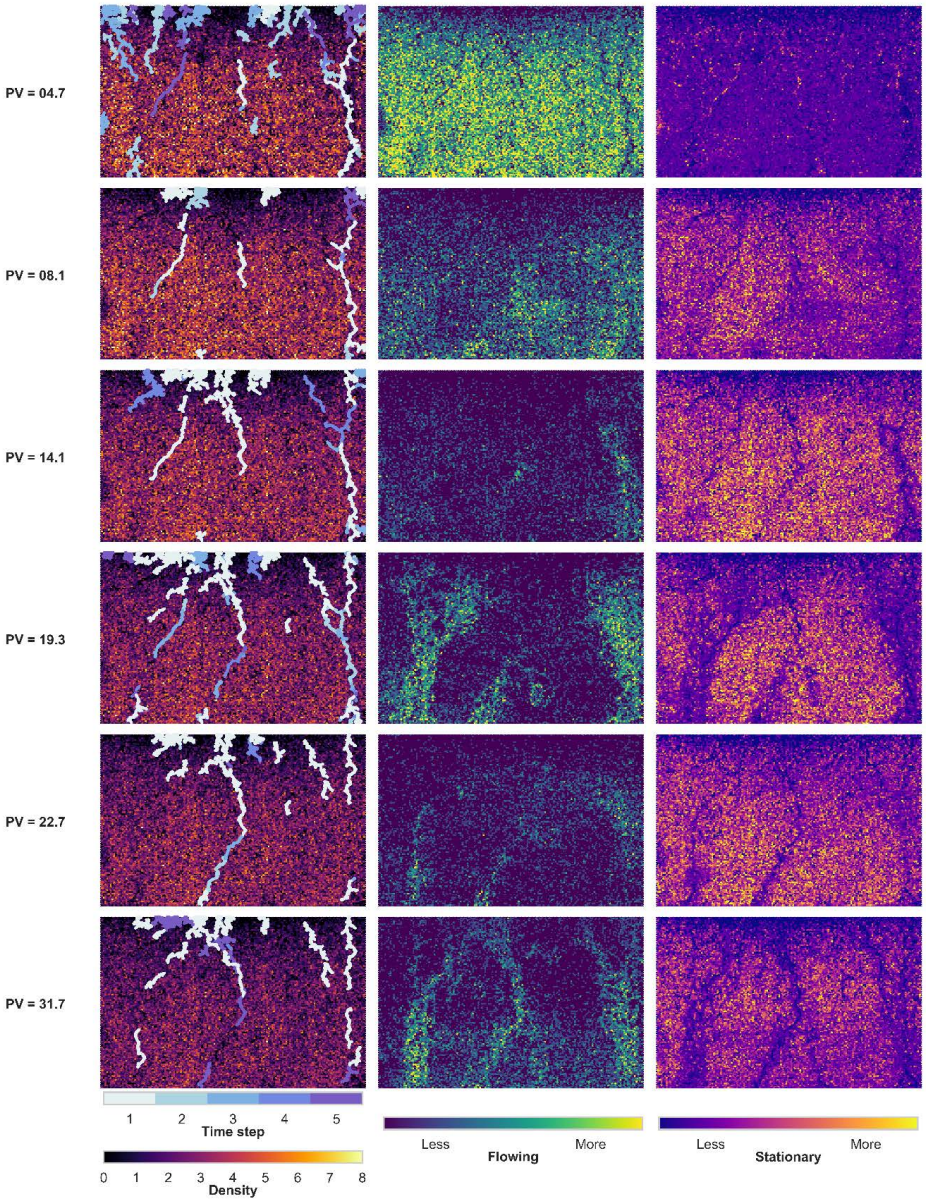

Fig. 11: **Dynamics of foam during decay, presented by three spatially resolved hexagonal binning plots: Left column, density of foam bubbles in the micromodel with mapped continuous gas channels (lines). Center, flowing foam. Right, trapped foam. The continuous gas channels, flowing foam and trapped foam were based on observations between 5 image frames, corresponding to 1.7 PV CO_2 injected. The micromodel was pre-saturated with the SF5000 foam agent solution prior to CO_2 injection, performed from top to bottom. The spatial resolution was 150 X 90mm.**

Calculation of gas mobility (Equation 3) requires knowledge of the reduction in gas effective permeability by trapped foam (k_g^{f*}) and the increase in effective gas viscosity by bubble trains (μ_g^f); however, open gas channels spanning the porous pattern (Fig.10) simplify the calculation, as the effective gas viscosity equals the no-foam gas viscosity ($n_f = 0$, Equation 2). An estimate of gas mobility in the presence of foam can therefore be obtained from the fraction of trapped gas, which reduces the effective gas permeability. The fraction of trapped gas was determined from the area constituting open gas channels (Fig. 12) versus time, but could alternatively be estimated from the area of the flowing regions (Fig. 11). Using Fig. 10 as a basis for calculation would, however, increase uncertainty because the area is determined over 1.7 PV of CO_2 injection, during which bubble trains and continuous gas channels irregularly relocate. Hence, the gas relative permeability (k_g^f) ranged between 0.008 and 0.017 (assuming a linear relationship between relative permeability and saturation at $S_g = 0.8$), corresponding to an apparent foam viscosity ranging between 5 - 10 cP. The estimated apparent viscosity is notably similar to the apparent viscosities observed after foam decay during core-scale foam injections (Chapter 4.2.3).

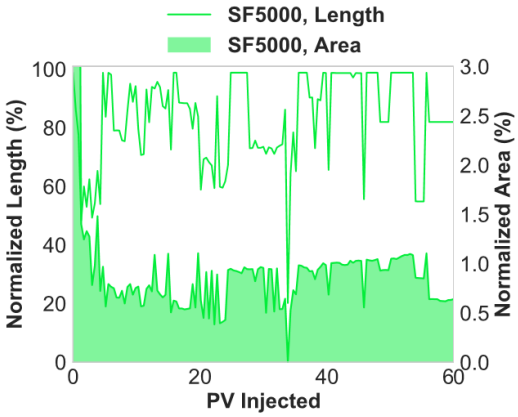

Fig. 12: **Quantification of open gas channel length and area. The length is normalized between inlet (0%) and outlet (100%) using solid lines. Channel area (filled region) is normalized with respect to the area of the pore space when the channel length exceeds 25%.**

There are three foam decay mechanisms in porous media: *i.* coarsening by diffusion (Ostwald ripening), *ii.* liquid film drainage by capillary forces, and *iii.* liquid film

drainage by gravity forces. The development in mean bubble area and the ratio $N_0/N(t)$ scaled linearly with time (PV injected) during pore-scale foam floods. Hence, the observed foam behavior agrees with Von Neumann's law describing coarsening of two-dimensional foams and indicates that coarsening by diffusion was the dominant decay mechanism (Fig. 13). $N(t)$ is the number of bubbles at time t and N_0 is the number of bubbles before foam decay becomes dominant, i.e., the highest number of observed bubbles. $N_0/\ N(t)$ of 1, hence, marks the transition when the rate of foam decay exceeds the rate of foam generation.

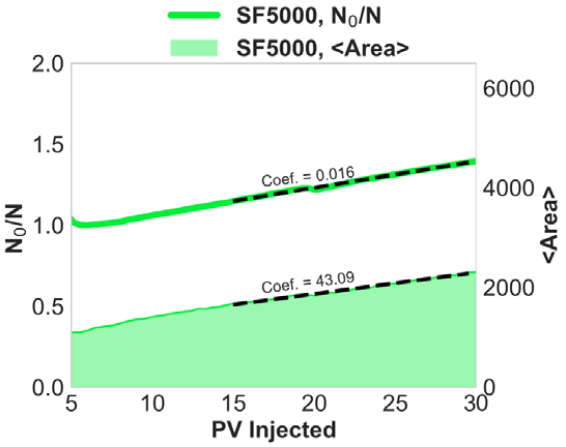

Fig. 13: **Foam decay occurred by Ostwald ripening. Both $N_0/N(t)$ and <A> scaled linearly with time, which agrees with Von Neumann's law 2D-foams. The associated regression coefficient (slope) is included above the curves.**

4.2.3 Darcy-scale foam decay

Foam decay was identified as a consistent decrease in apparent foam viscosity during unsteady-state foam injection on the Darcy-scale. Two distinct foam decay periods were observed: an initial period with rapid decrease and flowed by a period of slow decrease (Fig. 14). Pore-scale dynamivs potentially causing the two distinict foam decay periods will be elaborated in the next Chapter. Effect of residual oil was on foam decay was studied at the pore and Darcy-scale in Paper 3.

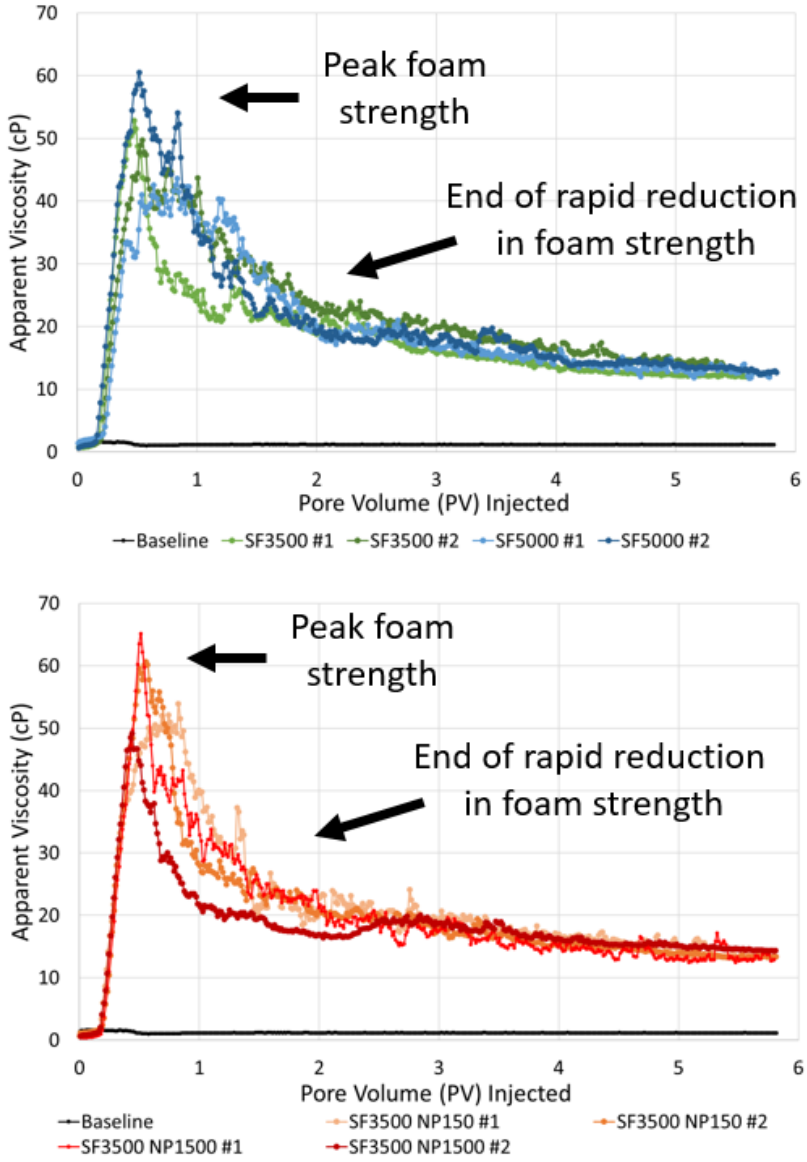

Fig. 14: **Apparent viscosity versus pore volume of CO_2 injected for the unsteady state CO_2 injections into cores pre-saturated with foaming solutions containing: (a) 3500 ppm (0.35 wt%) surfactant (green curves) and 5000 ppm (0.5 wt%) surfactant (blue curves); (b) hybrid foaming solutions containing 3500 ppm (0.35 wt%) surfactant and 150 ppm (0.015 wt%) nanoparticles (orange curves) and 3500 ppm (0.35 wt%) surfactant and 1500 ppm (0.15 wt%) nanoparticles (red curves). The purple curves show unsteady-state injections using brine (baseline) or nanoparticles as the foaming agent (NP5000).**

4.3 Linking foam dynamics across scales

The pore-scale investigation of foam performed using micromodels gave valuable information of foam dynamics and have extended the understanding of Darcy-scale foam observations. Commonly, interpretations across multiple scales, from to 2D pore-scale in micromodels to 3D Darcy-scale in rock samples are qualitative. However, the in-depth analysis of the pore-scale foam dynamics, supported with the framework developed for population balance foam models, revealed similar dynamics and quantitative estimates of foam strength.

The initial rapid decrease in apparent viscosity during Darcy-scale unsteady-state foam injection experiments (Fig. 13) may coincide with the formation of open gas channels spanning through the core. The slow decrease (following the initial rapid decrease) indicates established and stable open gas channels. The proposed link between the two scales is supported by similarity in measured Darcy-scale apparent viscosities after the initial rapid decrease (10-20 cP) (Fig. 13) and the pore-scale estimated apparent viscosity with open gas channels (5-10 cP).The latter slow foam decay is may caused by Oswald ripening, as observed during the micromodel foam injections.

The pore-level observations of open channels might reveal the mechanism causing the Super-linear and Linear foam generation categories. Linear foam generation potentially relates to an absence of flowing bubble trains, i.e., open channel(s) emerged immediately during foam generation. Super-linear foam generation potentially relates to the presence of flowing bubble trains during foam generation. The three experiments with Linear foam generation (Brij L23 H and L and AOS L, (Fig. 6 & Fig. 7) did not exhibit the two distinct decay periods (rapid and slow, see Fig. 13). The decrease in apparent foam viscosity occurred slowly and continuously in one period, resembling the later decay period observed in the remaining foam injections (Fig. 14). Additionally, the peak foam strength (highest recorded apparent viscosity) for the three respective foam injections was between 6-12 cP, similar to the pore-scale estimated apparent foam viscosity when open gas channels spanned the micromodel (5-10 cP). This indicated that Linear foam generation relates to an absence of flowing bubble trains, i.e., open gas

channel(s) was immediately present during Linear foam generation. Flowing bubble trains, increasing the effective gas viscosity, may have caused the higher foam strength observed during Super-linear foam generation. Rapid reduction in apparent viscosity may have resulted from the formation of open gas channels replacing the flowing bubble trains.

Further, backward propagating foam observed in micromodels (Fig. 5) may be similar to Delayed foam generation on the Darcy-scale. Delayed foam generation differs from the Linear and Super-linear categories, where foam generates at the advancing CO_2 saturation front, and is characterized by an abrupt and rapid increase in apparent foam viscosity after an extended period of CO_2 injection. Core scale foam injections using foaming agent Tergitol NP10 L (Fig. 8) were particularly indicative of backward propagating foam, as foam generation started when the injected CO_2 reached the outlet end face of the core (i.e. a sharp permeability contrast) and apparent foam viscosity increased abruptly. Several reports of backward propagating foam during Darcy-scale experiments are also found (Simjoo & Zitha 2020; Almajid *et al.* 2019; Apaydin & Kovscek 2001).

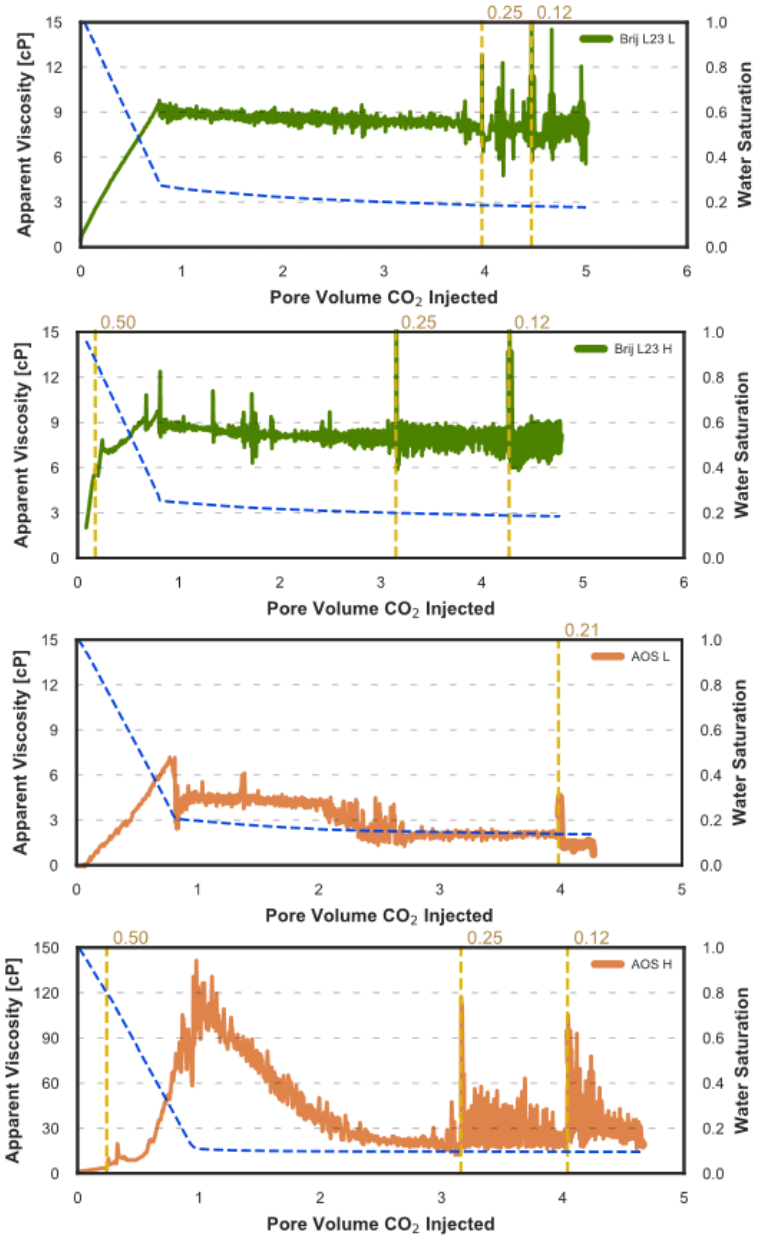

Fig. 15: **Apparent viscosities (solid colored lines) and water saturation (blue dashed lines) versus pore volumes of CO_2 injected for the Brij L23 and AOS foam injections. High (H) and low (L) initial flow rate is marked in the legend. Reduction in injection rate is shown using vertical yellow dashed lines, and the new rate (ml/min) is marked above. Both Brij L23 and the low initial flow rate AOS foam injections exhibits Linear foam generation, whereas the high initial flow AOS exhibits Super-linear foam generation.**

4.4 Steady-state co-injections and input for foam modeling

Steady-state co-injections, with simultaneous injection of CO_2 and foaming agent solution were performed in a Bentheimer sandstone core (Paper 4) using the same six commercially available surfactants as in Paper 2. All six commercially available surfactants generated foam. The experimental results were fitted to an implicit-texture local-equilibrium foam model, developed by Vassenden & Holt (2020) and denoted the V-H model. The foam model agreement demonstrated the extent of the experimental steady-state dataset, which should contain three physical features of foam when used as input for numerical models:

i) The high- and low-quality regimes, separated by the transition gas fraction, where the mobility reduction (apparent viscosity) of foam is largest.

ii) The shear-thinning behavior in the low-quality regime, due to the limiting pressure gradient (Rossen and Wang, 1999).

iii) The abrupt reduction in foam strength in the high-quality regime, due to high capillary pressure (Falls *et al.*, 1989).

Four of the six commercially available surfactants exhibited the three physical foam characteristics features during the steady-state co-injections and followed model assumption. The main observations were:

i) All three physical features were observed during steady-state co-injection using anionic AOS surfactant (Fig. 16).

ii) All three physical features were observed during steady-state co-injection using non-ionic Brij L23 surfactant. The distribution in water saturations and lack of data points showing shear-thinning behavior, however, indicate that most data points were obtained in the high-quality regime, or at the transition to the high-quality regime.

iii) All three physical features were observed during steady-state co-injection using non-ionic Igepal CO720 and Tergitol NP10 surfactants. A minor

adjustment in the reference water relative permeability curve was, however, needed to get a satisfactory match between the experimental datapoints and foam model curves.

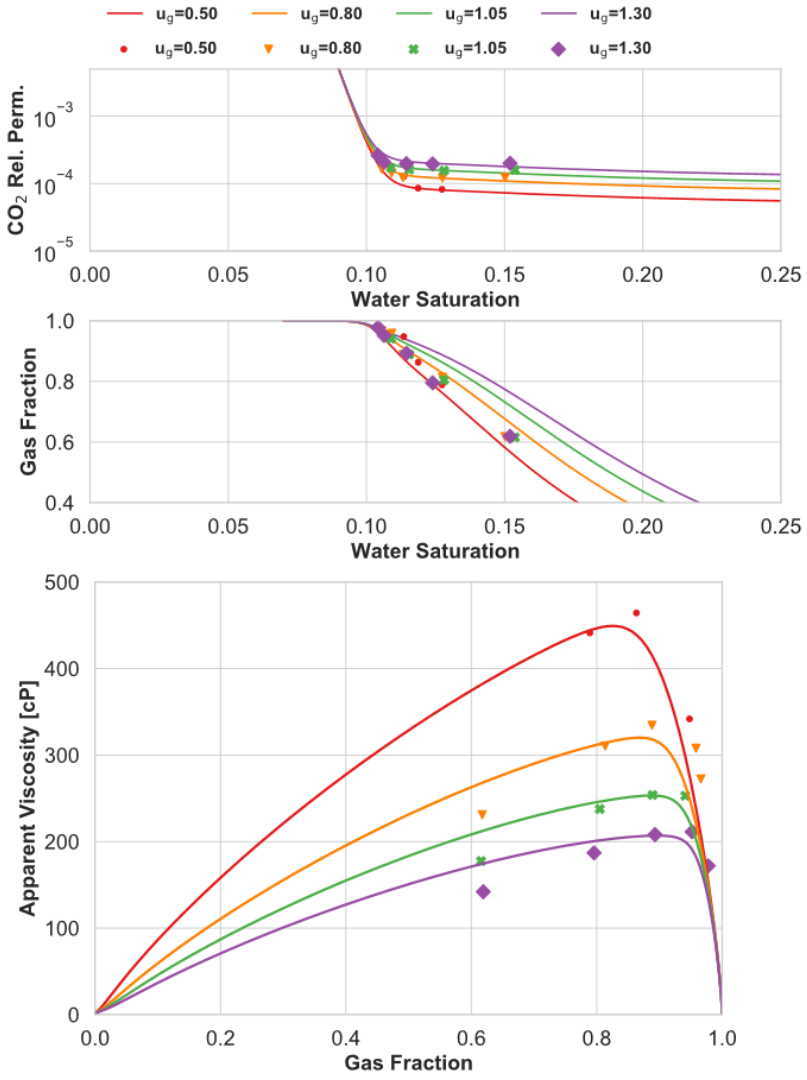

Fig. 16: Steady-state co-injection with CO_2 and anionic AOS surfactant. The V-H model (solid lines) was matched to experimental data (symbols). Top-left: CO_2 relative permeability versus water saturation. Bottom-left: Gas fractional flow versus water saturation. Right: Apparent viscosity versus gas fractional flow. The experimental data points at different gas flow velocities are shown using unique markers and colors.

Two of the non-ionic surfactants, Tergitol TMN 10 and Tergitol 5-S-9 exhibited a relationship between water saturation (S_w) and foam gas relative permeability (k_{rg}^f) that did not correspond with foam model assumptions. The water saturation is expected to decrease (or remain constant) when the gas fraction is increased during steady-state injections, thus the lowest water saturation observed should correspond to the highest injected gas fraction. For Tergitol TMN 10 (Fig. 17) and Tergitol 15-S-9 surfactant this behavior was not observed, as the lowest water saturations were measured at 0.8 and 0.9 gas fraction, and were higher at both lower (0.6) and higher (0.95) gas fraction.

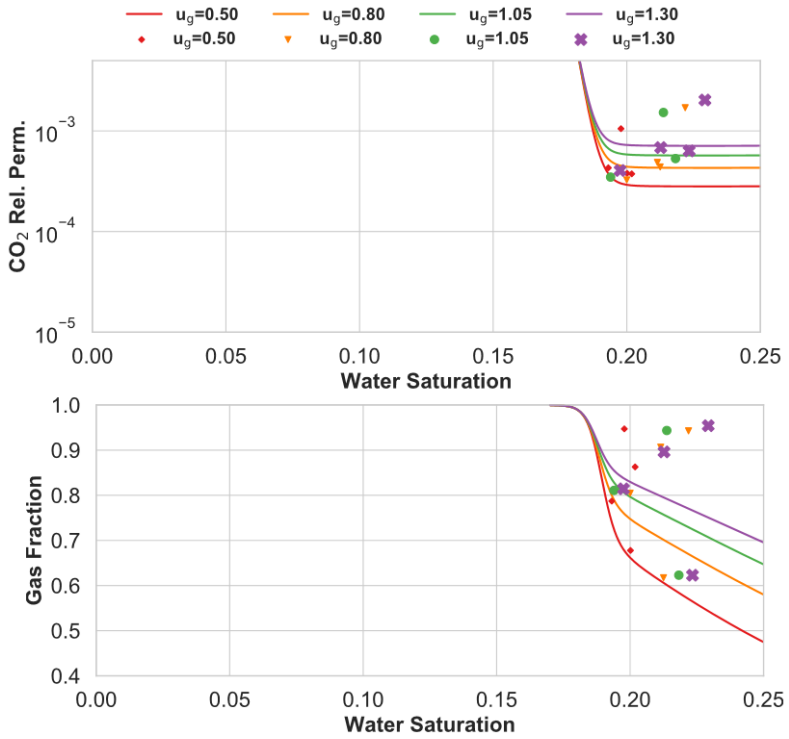

Fig. 17: Steady-state foam flood using the Tergitol TMN 10 (non-ionic). Left: Relative permeability versus water saturation. Right: Fractional flow (gas and water) versus water saturation. The experimental data points at different gas flow velocities are shown using unique shapes and colors. Modelled curves are shown using lines; gas flow velocities are shown using the same color-scheme as the experimental data points.

4.5 Performance of foaming agents

Peak foam apparent viscosity (cP) observed during steady-state and unsteady-state foam injections are compared in Fig. 18 and constitute a basis to discuss the performance of the different foaming agents. All of the tested surfactants generated foam during steady-state co-injection, resulting in apparent viscosity above 100 cP. The Tergitol 15-S-9 surfactant did not generate foam during the unsteady-state foam injections. The foam generation category also influenced the peak apparent viscosity, where Linear foam generation (marked * in Fig. 18) resulted in lower foam strength (<10 cP,) than Super-linear and Delayed foam generation. Silica nanoparticles added to the foaming agent solution had no significant effect on foam apparent viscosity during unsteady-state foam.

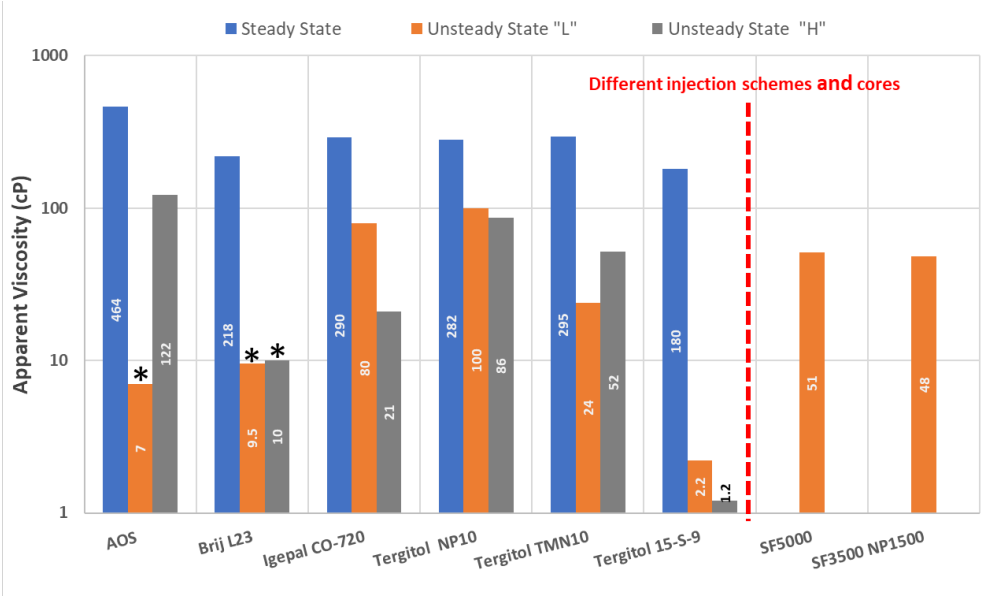

Fig. 18: Peak apparent viscosity observed for different foaming agent solutions during steady-state and unsteady-state foam injections. The SF5000 and SF3500 NP1500 foam injections were performed using different injection schemes and cores. The unsteady-state injections marked with * exhibited linear foam generation, which resulted in apparent viscosity below 10 cP.

Foam strength observed during unsteady-state foam injection was, as expected, lower than steady-state foam strength because:

i) Foam is more easily formed when both phases flow together in a confined volume.

ii) During unsteady-state injections, foam generation occur at the saturation front simultaneously as decay occur behind the saturation front. The transient foam properties cause higher foam strength (similar to steady-state co-injections) over a shorter distance of the core at any given time during the unsteady-state injections.

All tested surfactants could be used to form CO_2 foam, based on the steady- and unsteady foam characteristics, except Tergitol 15-S-9. Additional features of the surfactant and foam systems must be considered before use in field-scale applications, including:

i) Surfactant stability at reservoir conditions (salinity, temperature, and cloud point)

ii) Surfactant partitioning between CO_2 and water at reservoir conditions

iii) Adsorption of surfactant to rock surfaces

iv) Toxicity of surfactant

v) Foam stability in the presence of oil

vi) Minimum pressure gradients for foam generation

vii) Cost of surfactant

Surfactant cloud point and surfactant partitioning between CO_2 and water at varying temperature and pressure conditions were previously reported by (Barrabino *et al.*, 2020) for the six surfactants used in Paper 2 & 4. Tergitol 15-S-9 and Tergitol NP10 cloud point temperatures were reported to be low (below 60 °C), which implies poor applicability in many reservoirs. Igepal CO720 showed promising foam characteristics and partitioning coefficient, however, the presence of a benzene ring raises concern regarding potential toxicity. Tergitol TMN10 and Brij L23 may be the most promising non-fluorinated, non-ionic, partially CO_2 soluble surfactants for field-scale applications.

The surfactant used in the two laboratory studies presented in Paper 1 & 3, Surfonic L24-22, is chemically similar to the Brij L23. The laboratory results using the Surfonic L24-22 and Brij L23 surfactants supports the use highly ethoxylated linear alcohols for field-scale applications. Surfonic L24-22 is used in the field pilot presented in Paper 5; however, the reservoir pressure (180 bar) is insufficient to cause efficient partitioning into CO_2. For the field test the surfactant (Surfonic L24-22) is therefore considered water-soluble only. The Brij L23 is highly soluble in CO_2 at pressure above 300 bar (Barrabino *et al.* 2020), and is potentially applicable as a CO_2 soluble surfactant in north sea reservoirs.

4.6 Improved CO_2 storage capacity

The CO_2 storage capacity in geological formation is given by the size of the formation, mean porosity, how efficient formation fluids are displaced, and the density of CO_2 at pressure and temperature conditions of the formation. Injection of foam primarily aims to increase the volumetric sweep efficiency by improving the mobility ratio between the injected CO_2 and formation fluids. Reduction in residual water saturation was also consistently observed in the experiments presented in this thesis (Fig. 19), providing additional storage potential for CO_2. The water saturation reduction was attributed to increased microscopic water displacement (i.e., enhanced water mobilization at the pore level). The reduction in the residual water saturation is beneficial, as it increases the storage capacity in geological formations. Increases the storage capacity is particularly important for CO_2-EOR projects aiming to produce oil with a neutral carbon footprint. As oil with a neutral carbon footprint requires that the amount of CO_2 stored (during CO_2-EOR) accounts for the CO_2 released during combustion of the produced oil.

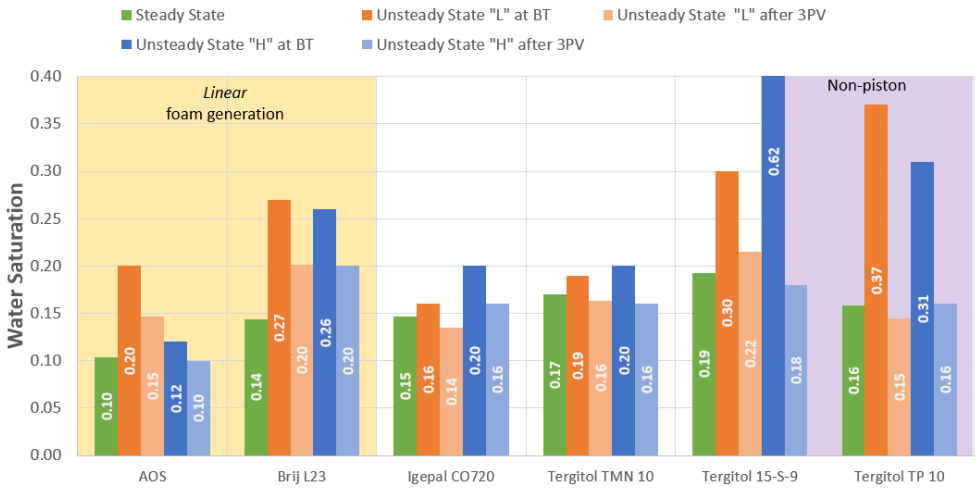

Fig. 19: Water saturations measured during steady-state and unsteady-state foam injections. Water saturations from the Unsteady state foam injection, both H and L, are shown at gas-breakthrough (BT) and after three pore volumes of CO_2 injection (3PV). Foam injections exhibiting linear foam generation (unsteady-state) and non-piston like water displacement (unsteady-state) or performed in a shorter core are marked.

Capillary desaturation curves illustrate that the residual saturation decrease when the capillary number increases (Eq 2). A clear trend between the capillary number (N_{ca}) and residual water saturation after unsteady-state foam injection was observed (Fig. 20). Foams are particularly effective in reducing the capillary number (N_{ca}), as the viscosity (μ) is increased, simultaneously, the interfacial tension (σ) is reduced when surfactants are used as the foaming agents.

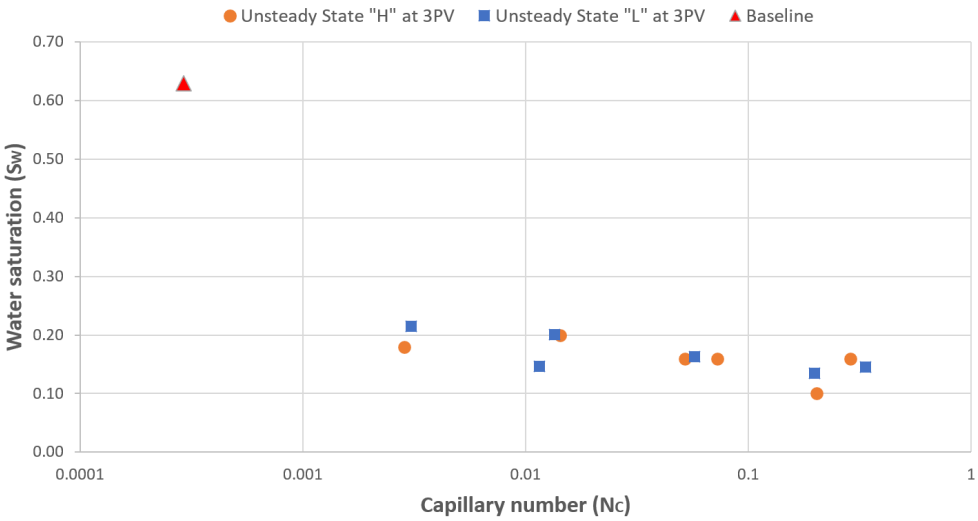

Fig. 20: Capillary desaturation curve for the unsteady-state foam injections using the six commercial surfactants presented in Paper 2. The water saturation (y-axis) was measured after three pore volumes of CO_2 injected. The capillary number is calculated using equation 2, using the highest measured foam apparent viscosity for each foam injection and measured interfacial tension (IFT) for the given surfactant-CO_2 systems (Table 2). Orange markers are measured at high flow velocities, blue markers at low flow velocities and the red marker is the baseline injection performed without a foaming agent.

Table 2. Interfacial tension (IFT) at equilibrium conditions for all CO_2- surfactant systems. The measurements were performed at same pressure and temperature conditions as the core flooding experiments (40 °C and 200 bar) by Albert Barrabino (SINTEF).

	IFT [mN/m]
Brij L23	5.12
Tergitol 15-S-9	3.06
Tergitol TMN 10	2.18
Igepal CO 720	2.95
Tergitol NP 10	5.22
Igepal CA 720	3.00
AOS	4.41

Strong foam generation is beneficial for CO_2 storage, causing a fast and thereby efficient displacement of water (Paper 2). The two unsteady-state foam injections performed using the Tergitol NP10 surfactant demonstrated that increased pressure gradients by foam caused a fast reduction in water saturation. Both foam injections exhibited delayed foam generation and the displacement of water was initially inefficient, with breakthrough water saturations close to the baseline CO_2 injection (**Fig. 21**). After delayed foam generation, the water saturation was stepwise reduced to a end-point water saturation ~50% lower than the baseline.

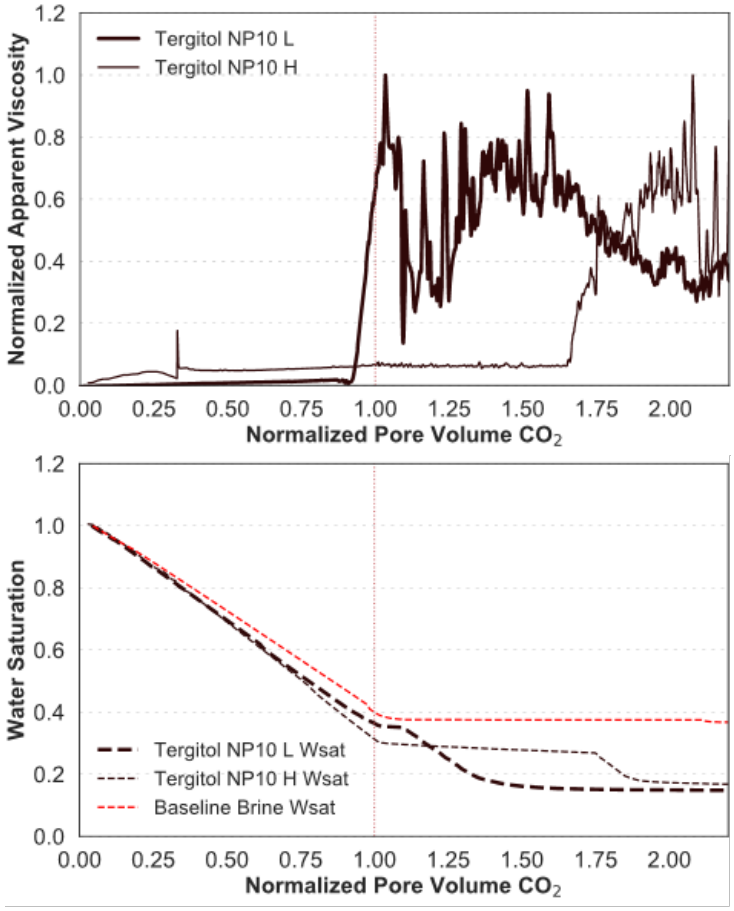

Fig. 21: Delayed foam generation was observed during CO_2 injection using surfactants Tergitol NP 10. The left figure shows apparent viscosity normalized to peak apparent viscosity, and the right figure shows water saturation development, both as functions of normalized time (PV CO_2 injected normalized to gas breakthrough). Gas breakthrough (1 PV) is indicated by the vertical red line. The water saturation profile for baseline CO_2 injection (no surfactant) is included for comparison.

4.7 CO_2-foam from pore- and Darcy- to field-scale

Reservoirs are large (km) with complex geometries and commonly have a heterogeneous distribution of flow properties (permeability). Direct replication of reservoirs is impractical to perform in a controlled laboratory environment. Displacement processes in reservoirs are, therefore, assessed using numerical models. In the context of field-scale numerical models, empirical data from the pore- and the Darcy-scale serve two purposes: developing numerical models and populating working models with input parameters. The previous sections contain examples of both purposes, discussed below.

Foam behavior that models potentially are able to capture is described in the previous sections, including

i) Foam generation mechanisms (Paper 2),
ii) continuous open channels (Paper 1),
iii) non-monotonic decreases in water saturation (Paper 4).

Simplifications are, however, often necessary to avoid complex models and to fit the lab-scale dynamics into a mathematical framework. Distinguishing between important foam behavior that must be captured by models and behavior that can be ignored is not straightforward. Foam performance validation has more confidence if field-scale data is available. A foam field-pilot has therefore been performed as part of the project *CO_2 Storage from Lab to On-Shore Field Pilots Using CO_2-Foam for Mobility Control in CCUS*. The pilot provides experience with field-scale foam injection operations, demonstrates the feasibility of CO_2-mobility control using foam, and provides valuable data to validation foam models.

Reservoir numerical models solve mass and momentum balance calculations and require empirical data as input parameters to fine-tuning for specific cases. Darcy-scale experiments provide mass and momentum balance measurements during flow in porous media and are therefore used extensively to populate working numerical models with,

porosity, permeability, end-point saturations, relative permeability- and capillary pressure -curves. The Darcy-scale experiments presented in this dissertation were performed in sandstone representative for north-sea reservoirs and are useful for feasibility studies of CO_2-EOR with mobility control using foam. Reservoir simulations can be performed using the foam model calibrations based on steady-state co-injection data presented in Paper 4. Similar foam model calibrations experiments were performed as a part of the preparation program prior CO_2 foam field pilot and provide empirical input for the numerical model used to interpret the field-pilot (Alcorn *et al.* 2019).

4.7.1 Preliminary field-pilot results

The field pilot is performed as a surfactant-alternating-gas injection (SAG), where each cycle constitutes approximately 10 days of surfactant injection and approximately 20 days of CO_2 injection. Surfactant injection rate is 500 bbl/day at 0.5wt% concentration and CO_2 injection rate is 1200 mcf/day. The field-pilot is still on-going and initial results are promising, but inconclusive. Interpretation of the observations, aided with numerical simulations, are ongoing.

A bottom hole pressure (BHP) gauge ("pressure bomb") was installed in the injection well two weeks prior to the start of the field pilot. The pressure data was used to calculate the CO_2 injectivity index ($Mscf/psi$) prior to the field pilot (Baseline) and during the field pilot CO_2 slugs (Fig. 22). The initial CO_2 injectivity, directly after surfactant injection, were reduced by nearly 70% compared with the baseline period. The CO_2 injectivity increased during CO_2 injection periods, likely due to foam dry-out (capillary suction coalescence) or generation of continuous open gas channels through the surfactant-bank. A short water-alternating-gas (WAG) injection is planned at the end of the SAG injection to compare the effect of foam with any potential reduction in relative permeability due to the presence of water.

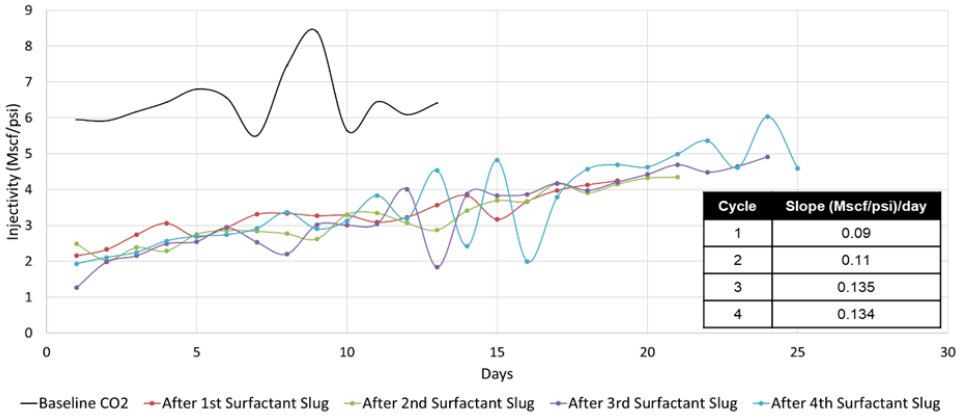

Fig. 22: Injectivity index during the baseline CO_2 period (black curve) and during each CO_2 slug after surfactant slug injection (red, green, purple, and blue curves). The rate of change (slope) for each slug is shown in the right inset.

Injection profiles were frequently collected during the duration of the field pilot (Fig. 24). The injection profiles show where injected fluids are flowing into the formation, and are used to assess if foam causes diversion of flow from high permeability streaks to other zones of the reservoir in the near well area. The initial injection profiles show that both CO_2 and water/surfactant is primarily flowing into the high permeability streak (from 5465 ft to 5471 ft). Later injection profiles show increased flow in layers adjacent to the high permeability streak, indicating flow diversion and increased sweep. The injections profiles indicate insignificant gravity segregation close to the injection well as the surfactant solution enter the same flow zone as CO_2. Reduction in CO_2 injectivity, combined with flow diversion, indicates foam generation. Analysis of field response is ongoing as more production data becomes available.

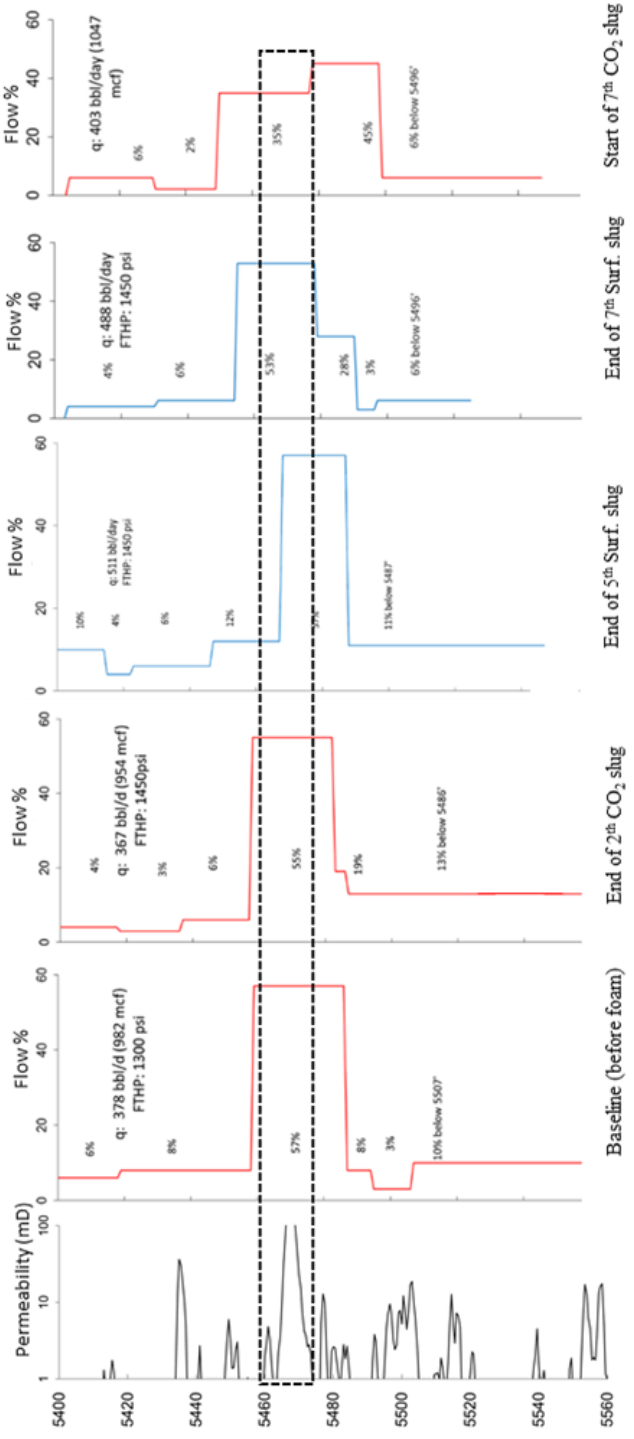

Fig. 23: Injection profiles from before the pilot (May 2019), at the end of second CO_2 slug (July2019), at the end of the fifth and seventh surfactant slugs (Oct 2019, Dec 2019), and at the start of the seventh CO_2 slug (Dec 2019). Blue profiles indicate water (surfactant solution) injection, whereas red indicates CO_2. A permeability log for the pilot injection well is also shown at far left. The dashed area represents the high permeability streak from 5465 ft to 5471 ft.

Oil production from the field-pilot pattern is maintained through the project, whereas gas and water production has decreased by 40% and 20% (Fig. 24). Production and injection wells adjacent to pilot-well (L14, Fig. 24) affects the performance and production response of the pilot-well. Therefore, numerical simulations are performed to understand the behavior of the complete pilot pattern area and assess the effect of foam.

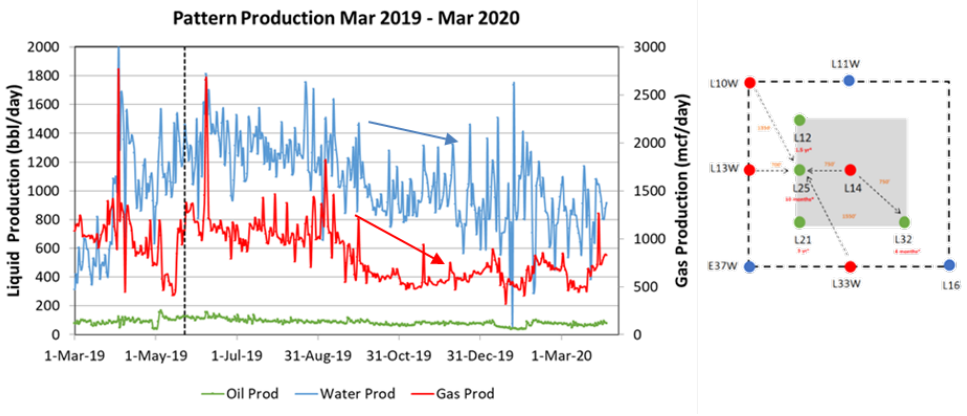

Fig. 24: Oil, water, and gas production rates from the pilot pattern production wells (L25, L32, L21, and L12) from March 2019 to March 2020. Liquid production (oil and water) is shown on the primary y-axis, whereas gas production is shown on the secondary y-axis. The black dashed line shows the start of pilot on 23 May 2019. The foam pilot pattern is shown at right, where L14 is the pilot injector.

5. Conclusions

Utilization of CO_2 for EOR has been suggested to catalyze the implementation of large-scale carbon capture and storage of CO_2 on the Norwegian continental shelf by establishing the necessary infrastructure and drive technology development. However, the potential economic revenue from CO_2-EOR has yet been insufficient for the industry. An inherent challenge during CO_2-EOR and CO_2 storage is poor sweep efficiency due to the low viscosity of CO_2 at reservoir conditions compared with formation fluids (brine and oil). This work presents a comprehensive multi-scale investigation of CO_2-foam as a technological solution that can improve the sweep efficiency and make CO_2-EOR implementation feasible at industrial scale. Five scientific papers form the foundation of this dissertation: Pore-scale foam dynamics (Paper 1), Darcy-scale foam generation and decay in the absence (Paper 2) and presence of oil (Paper 3), steady-state foam characteristics (Paper 4), and field-scale implementation of CO_2-foam (Paper 5). As compiled work, the dissertation strengthens the conclusion presented in the individual scientific papers, but also draw additional conclusions based on findings across them. The main conclusions are summarized:

- CO_2-foam extends the lifetime of existing, mature oil-fields by producing inaccessible oil, and increases the amount of storable CO_2 in the reservoir by displacing water. Depending on crude oil composition, CO_2-foam may produce crude oil with a reduced carbon footprint; where the amount of CO_2 stored accounts for CO_2 released during combustion of produced oil. Improved CO_2-EOR with mobility control using CO_2-foam should be considered as one of several technologies to limit global warming to 1.5 °C.

- Five commercially available non-ionic non-fluorinated surfactants that are partially soluble in CO_2 have been evaluated as CO_2 foam stabilizers. Darcy-unsteady-state foam injection reviled generation and decay behavior, whereas Darcy-scale steady-state foam experiments provided valuable data for fine-tuning reservoir scale numerical simulators. The dataset is applicable for feasibility studies of CO_2-foam application in Norwegian continental shelf

reservoirs and might advance the implementation of CO_2-EOR with associated storage.

- Deeper understanding of porous media foam flow physics was achieved through complementary, pore- and Darcy-scale experiments reported in this thesis. It was established that formation of continuous and open gas channels was essential for foam generation- and decay behavior. The improved understanding of multi-scale foam dynamics will improve current foam modeling tools when implemented.

- Preliminary results from an ongoing US CO_2-foam field pilot are promising and demonstrate reduced CO_2 injectivity and increased CO_2 sweep efficiency. Conclusive results require in-depth analysis, aided with numerical simulations, of emerging field-performance indicators that is currently not available as part of this thesis. Nevertheless, the pilot project demonstrates the feasibility of CO_2-mobility control using foam and provides experience with field-scale foam injection operations. Hopefully, a successful demonstration of CO_2-foam, coupled with available, high-quality laboratory datasets, can encourage implementation of CO_2-EOR on the Norwegian continental shelf.

6. Symbols and Nomenclature

f_g	Gas fraction
k	Absolute permeability
k_{rCO_2}	CO_2 relative permeability (without foam)
k_{rg}^{f}	Gas-foam relative permeability
k_{rg}^{f*}	Effective gas-foam relative permeability
k_{rw}	Water relative permeability
MRF	Mobility reduction factor
N	Number of bubbles
N_0	Highest number of bubbles
N_{ca}	Capillary number
n_f	Flowing foam bubble density
P_c^*	Limiting capillary pressure
∇P	Pressure gradient
u_g	Superficial gas flow velocity
u_w	Superficial water flow velocity
v_f	Interstitial velocity
S_g	Gas saturation
S_{fg}	Flowing foam pseudo saturation
S_{tg}	Trapped foam pseudo saturation
S_w	Water saturation
S_w^*	Foam breakdown saturation
λ_g	CO_2 mobility
μ_{app}	Foam Apparent viscosity
μ_{CO2}	CO_2 viscosity
μ_g^*	Foam effective gas viscosity
μ_w	Water viscosity
σ	Interfacial tension

AOS	Alpha olefin sulfonates
BHP	Bottom hole pressure
BECCS	Carbon capture and storage from biomass
CCS	Carbon capture and storage
CCUS	Carbon capture and utilization
CDR	Carbon dioxide removal
GOR	Gas-oil production ratios
HDI	Human Development Index
IEA	International Energy Agency
IPCC	Intergovernmental Panel on Climate Change
SAG	Surfactant-Alternating-Gas
SG	Continuous Surfactant-Gas injection
WAG	Water-alternating-gas
WASG	Water-Alternating-Gas-with-Surfactant-in-Gas

7. References

Adkins, S.S., Chen, X., Chan, I., Torino, E., Nguyen, Q.P., Sanders, A.W., Johnston, K.P.: Morphology and Stability of CO2-in-Water Foams with Nonionic Hydrocarbon Surfactants. *Langmuir* **26**(8), 5335-5348 (2010a). doi: https://doi.org/10.1021/la903663v

Adkins, S.S., Chen, X., Nguyen, Q.P., Sanders, A.W., Johnston, K.P.: Effect of branching on the interfacial properties of nonionic hydrocarbon surfactants at the air–water and carbon dioxide–water interfaces. *Journal of Colloid and Interface Science* **346**(2), 455-463 (2010b). doi: https://doi.org/10.1016/j.jcis.2009.12.059

Alcorn, Z.P., Fredriksen, S.B., Sharma, M., Rognmo, A.U., Føyen, T.L., Fernø, M.A., Graue, A.: An Integrated Carbon-Dioxide-Foam Enhanced-Oil-Recovery Pilot Program With Combined Carbon Capture, Utilization, and Storage in an Onshore Texas Heterogeneous Carbonate Field. *SPE-190204-PA* **22**(04), 1449-1466 (2019). doi: https://doi.org/10.2118/190204-PA

Anthonsen, K.L., Aagaard, P., Bergmo, P.E.S., Gislason, S.R., Lothe, A.E., Mortensen, G.M., Snæbjörnsdóttir, S.Ó.: Characterisation and Selection of the Most Prospective CO2 Storage Sites in the Nordic Region. *Energy Procedia* **63**, 4884-4896 (2014). doi: https://doi.org/10.1016/j.egypro.2014.11.519

Arneth, A., F. Denton, F. Agus, A. Elbehri, K. Erb, B. Osman Elasha, M. Rahimi, M. Rounsevell, A. Spence, R. Valentini: Framing and Context. In: Climate Change and Land: an IPCC special report on climate change, desertification, land degradation, sustainable land management, food security, and greenhouse gas fluxes in terrestrial ecosystems In: P.R. Shukla, J.S., E. Calvo Buendia, V. Masson-Delmotte, H.-O. Pörtner, D.C. Roberts, P. Zhai, R. Slade, S. Connors, R. van Diemen, M. Ferrat, E. Haughey, S. Luz, S. Neogi, M. Pathak, J. Petzold, J. Portugal Pereira, P. Vyas, E. Huntley, K. Kissick, M. Belkacemi, J. Malley (ed.). (2019)

Balat, H., Öz, C.: Technical and Economic Aspects of Carbon Capture an Storage — A Review. *Energy Exploration & Exploitation* **25**(5), 357-392 (2007). doi: https://doi.org/10.1260/014459807783528883

Barrabino, A., Holt, T., Lindeberg, E.: Partitioning of non-ionic surfactants between CO2 and brine. *Journal of Petroleum Science and Engineering* **190**, 107106 (2020). doi: https://doi.org/10.1016/j.petrol.2020.107106

Benali, B.: Quantitative Pore-Scale Analysis of CO2 Foam for CCUS. University of Bergen (2019)

Bickle, M.J.: Geological carbon storage. *Nature Geoscience* **2**(12), 815-818 (2009). doi: https://doi.org/10.1038/ngeo687

Blaker, T., Celius, H.K., Lie, T., Martinsen, H.A., Rasmussen, L., Vassenden, F.: Foam for Gas Mobility Control in the Snorre Field: The FAWAG Project. Paper presented at the SPE Annual Technical Conference and Exhibition,

Houston, Texas, 1999/1/1/ 1999 of Conference. doi: https://doi.org/10.2118/56478-MS

Buchgraber, M., Al-Dossary, M., Ross, C.M., Kovscek, A.R.: Creation of a dual-porosity micromodel for pore-level visualization of multiphase flow. *Journal of Petroleum Science and Engineering* **86-87**, 27-38 (2012). doi: https://doi.org/10.1016/j.petrol.2012.03.012

Chen, M., Yortsos, Y.C., Rossen, W.R.: Insights on foam generation in porous media from pore-network studies. *Colloids and Surfaces A: Physicochemical and Engineering Aspects* **256**(2), 181-189 (2005). doi: https://doi.org/10.1016/j.colsurfa.2005.01.020

Chen, Y., Elhag, A.S., Cui, L., Worthen, A.J., Reddy, P.P., Noguera, J.A., Ou, A.M., Ma, K., Puerto, M., Hirasaki, G.J., Nguyen, Q.P., Biswal, S.L., Johnston, K.P.: CO2-in-Water Foam at Elevated Temperature and Salinity Stabilized with a Nonionic Surfactant with a High Degree of Ethoxylation. *Industrial & Engineering Chemistry Research* **54**(16), 4252-4263 (2015). doi: https://doi.org/10.1021/ie503674m

Cheng, L., Reme, A.B., Shan, D., Coombe, D.A., Rossen, W.R.: Simulating Foam Processes at High and Low Foam Qualities. Paper presented at the SPE/DOE Improved Oil Recovery Symposium, Tulsa, Oklahoma, 2000/1/1/ 2000 of Conference. doi: https://doi.org/10.2118/59287-MS

Chou, S., Vasicek, S., Pisio, D., Jasek, D., Goodgame, J.: CO2 Foam Field Trial at North Ward-Estes. Paper presented at the SPE Annual technical conference and exhibition, 1992 of Conference. doi: https://doi.org/10.2118/24643-MS

Elsharkawy, A.M., Poettmann, F.H., Christiansen, R.L.: Measuring CO2 Minimum Miscibility Pressures: Slim-Tube or Rising-Bubble Method? *Energy & Fuels* **10**(2), 443-449 (1996). doi: https://doi.org/10.1021/ef940212f

Ettehadtavakkol, A., Lake, L.W., Bryant, S.L.: CO2-EOR and storage design optimization. *International Journal of Greenhouse Gas Control* **25**, 79-92 (2014). doi: https://doi.org/10.1016/j.ijggc.2014.04.006

Falls, A.H., Musters, J.J., Ratulowski, J.: The Apparent Viscosity of Foams in Homogeneous Bead Packs. *SPE Reservoir Engineering* **4**(02), 155-164 (1989). doi: https://doi.org/10.2118/16048-PA

Farajzadeh, R., Eftekhari, A.A., Dafnomilis, G., Lake, L.W., Bruining, J.: On the sustainability of CO2 storage through CO2 – Enhanced oil recovery. *Applied Energy* **261**, 114467 (2020). doi: https://doi.org/10.1016/j.apenergy.2019.114467

Farajzadeh, R., Lotfollahi, M., Eftekhari, A.A., Rossen, W.R., Hirasaki, G.J.H.: Effect of Permeability on Implicit-Texture Foam Model Parameters and the Limiting Capillary Pressure. *Energy & Fuels* **29**(5), 3011-3018 (2015). doi: https://doi.org/10.1021/acs.energyfuels.5b00248

Fried, A.N.: Foam-Drive Process for Increasing the Recovery of Oil. In. University of North Texas Libraries, Washington D.C., (1961)

Friedmann, F., Chen, W.H., Gauglitz, P.A.: Experimental and Simulation Study of High-Temperature Foam Displacement in Porous Media. *SPE Reservoir Engineering* **6**(01), 37-45 (1991). doi: https://doi.org/10.2118/17357-PA

Fulcher, R.A., Jr., Ertekin, T., Stahl, C.D.: Effect of Capillary Number and Its Constituents on Two-Phase Relative Permeability Curves. *SPE-2116-PA* **37**(02), 249-260 (1985). doi: https://doi.org/10.2118/12170-PA

Gauglitz, P.A., Friedmann, F., Kam, S.I., Rossen, W.R.: Foam generation in homogeneous porous media. *Chemical Engineering Science* **57**(19), 4037-4052 (2002). doi: https://doi.org/10.1016/S0009-2509(02)00340-8

Grimstad, A.-A., Bergmo, P.E.S., Nilsen, H.M., Klemetsdal, Ø.: CO2 Storage with Mobility Control. Paper presented at the 14th Greenhouse Gas Control Technologies Conference Melbourne, 21-26 October 2018

Guo, H., Dou, M., Hanqing, W., Wang, F., Yuanyuan, G., Yu, Z., Yansheng, W., Li, Y.: Proper Use of Capillary Number in Chemical Flooding. *Journal of Chemistry* **2017**, 4307368 (2017). doi: https://doi.org/10.1155/2017/4307368

Henry, R.L., Fisher, D.R., Pennell, S.P., Honnert, M.A.: Field Test of Foam to Reduce CO2 Cycling. Paper presented at the SPE/DOE Improved Oil Recovery Symposium, 1996 of Conference. doi: https://doi.org/10.2118/35402-MS

Hirasaki, G.J., Lawson, J.B.: Mechanisms of Foam Flow in Porous Media: Apparent Viscosity in Smooth Capillaries. *Society of Petroleum Engineers Journal* **25**(02), 176-190 (1985). doi: https://doi.org/10.2118/12129-PA

Hoefner, M., Evans, E.: CO2 Foam: Results From Four Developmental Field Trials. *SPE Reservoir Engineering* **10**(04), 273-281 (1995). doi: https://doi.org/10.2118/27787-PA

IEA: World Energy Outlook 2019. In, vol. Paris. IEA, (2019)

IPCC: Summary for Policymakers. In: Global Warming of 1.5°C. An IPCC Special Report on the impacts of global warming of 1.5°C above pre-industrial levels and related global greenhouse gas emission pathways, in the context of strengthening the global response to the threat of climate change, sustainable development, and efforts to eradicate poverty. In: Masson-Delmotte, V., P. Zhai, H.-O. Pörtner, D. Roberts, J. Skea, P.R. Shukla, A. Pirani, W. Moufouma-Okia, C. Péan, R. Pidcock, S. Connors, J.B.R. Matthews, Y. Chen, X. Zhou, M.I. Gomis, E. Lonnoy, T. Maycock, M. Tignor, and T. Waterfield (ed.). p. 32. World Meteorological Organization, Geneva, Switzerland, (2018)

Kam, S.I., Rossen, W.R.: A Model for Foam Generation in Homogeneous Media. *SPE-195310-PA* **8**(04), 417-425 (2003). doi: https://doi.org/10.2118/87334-PA

Kearns, J., Teletzke, G., Palmer, J., Thomann, H., Kheshgi, H., Chen, Y.-H.H., Paltsev, S., Herzog, H.: Developing a Consistent Database for Regional Geologic CO2 Storage Capacity Worldwide. *Energy Procedia* **114**, 4697-4709 (2017). doi: https://doi.org/10.1016/j.egypro.2017.03.1603

Kontogeorgis, G.M., Kiil, S.: *Colloid Stability – Part II*. In: Introduction to Applied Colloid and Surface Chemistry. pp. 243-268. (2016)

Kovscek, A.R., Patzek, T.W., Radke, C.J.: A mechanistic population balance model for transient and steady-state foam flow in Boise sandstone. *Chemical Engineering Science* **50**(23), 3783-3799 (1995). doi: https://doi.org/10.1016/0009-2509(95)00199-F

Kovscek, A.R., Radke, C.J.: *Fundamentals of Foam Transport in Porous Media*. In: Foams: Fundamentals and Applications in the Petroleum Industry, vol. 242. Advances in Chemistry, vol. 242, pp. 115-163. American Chemical Society, (1994)

Kovscek, A.R., Tang, G.Q., Radke, C.J.: Verification of Roof snap off as a foam-generation mechanism in porous media at steady state. *Colloids and Surfaces A: Physicochemical and Engineering Aspects* **302**(1), 251-260 (2007). doi: https://doi.org/10.1016/j.colsurfa.2007.02.035

Lake, L.W., Johns, R.T., Rossen, R.W., Pope, G.A.: *Fundamentals of Enhanced Oil Recovery*. Society of Petroleum Engineers, Richardson (2014)

Langston, M.V., Hoadley, S.F., Young, D.N.: Definitive CO2 Flooding Response in the SACROC Unit. Paper presented at the SPE Enhanced Oil Recovery Symposium, Tulsa, Oklahoma, 1988/1/1/ 1988 of Conference. doi: https://doi.org/10.2118/17321-MS

Le, V.Q., Nguyen, Q.P., Sanders, A.: A Novel Foam Concept With CO2 Dissolved Surfactants. Paper presented at the SPE Symposium on Improved Oil Recovery, Tulsa, Oklahoma, USA, 2008/1/1/ 2008 of Conference. doi: https://doi.org/10.2118/113370-MS

Lee, S., Kam, S.I.: *Chapter 2 - Enhanced Oil Recovery by Using CO2 Foams: Fundamentals and Field Applications*. In: Sheng, J.J. (ed.) Enhanced Oil Recovery Field Case Studies. pp. 23-61. Gulf Professional Publishing, Boston (2013)

Lindeberg, E., Grimstad, A.-A., Bergmo, P., Wessel-Berg, D., Torsæter, M., Holt, T.: Large Scale Tertiary CO2 EOR in Mature Water Flooded Norwegian Oil Fields. *Energy Procedia* **114**, 7096-7106 (2017). doi: https://doi.org/10.1016/j.egypro.2017.03.1851

Lipponen, J., McCulloch, S., Keeling, S., Stanley, T., Berghout, N., Berly, T.: The Politics of Large-scale CCS Deployment. *Energy Procedia* **114**, 7581-7595 (2017). doi: https://doi.org/10.1016/j.egypro.2017.03.1890

Lotfollahi, M., Farajzadeh, R., Delshad, M., Varavei, A., Rossen, W.R.: Comparison of implicit-texture and population-balance foam models. *Journal of Natural Gas Science and Engineering* **31**, 184-197 (2016). doi: https://doi.org/10.1016/j.jngse.2016.03.018

Ma, K., Ren, G., Mateen, K., Morel, D., Cordelier, P.: Modeling Techniques for Foam Flow in Porous Media. *SPE-195310-PA* **20** (2015). doi: https://doi.org/10.2118/169104-PA

Mac Dowell, N., Fennell, P.S., Shah, N., Maitland, G.C.: The role of CO2 capture and utilization in mitigating climate change. *Nature Climate Change* **7**(4), 243-249 (2017). doi: https://doi.org/10.1038/nclimate3231

Marchalot, J., Lambert, J., Cantat, I., Tabeling, P., Jullien, M.C.: 2D foam coarsening in a microfluidic system. *EPL (Europhysics Letters)* **83**(6), 64006 (2008). doi: https://doi.org/10.1209/0295-5075/83/64006

McLendon, W.J., Koronaios, P., McNulty, S., Enick, R.M., Biesmans, G., Miller, A.N., Salazar, L.C., Soong, Y., Romanov, V., Crandall, D.: Assessment of CO2-Soluble Surfactants for Mobility Reduction using Mobility Measurements and CT Imaging. Paper presented at the SPE Improved Oil Recovery Symposium, Tulsa, Oklahoma, USA, 2012/1/1/ 2012 of Conference. doi: https://doi.org/10.2118/154205-MS

Moffitt, P., Pecore, D., Trees, M., Salts, G.: East Vacuum Grayburg San Andres Unit, 30 Years of CO2 Flooding: Accomplishments, Challenges and Opportunities. Paper presented at the SPE Annual Technical Conference and Exhibition, 2015 of Conference. doi: https://doi.org/10.2118/175000-MS

Nguyen, P., Fadaei, H., Sinton, D.: Pore-Scale Assessment of Nanoparticle-Stabilized CO2 Foam for Enhanced Oil Recovery. *Energy & Fuels* **28**(10), 6221-6227 (2014). doi: https://doi.org/10.1021/ef5011995

Radke, C.J., Gillis, J.V.: A Dual Gas Tracer Technique for Determining Trapped Gas Saturation During Steady Foam Flow in Porous Media. Paper presented at the SPE Annual Technical Conference and Exhibition, New Orleans, Louisiana, 1990/1/1/ 1990 of Conference. doi: https://doi.org/10.2118/20519-MS

Ransohoff, T.C., Radke, C.J.: Mechanisms of Foam Generation in Glass-Bead Packs. *SPE Reservoir Engineering* **3**(02), 573-585 (1988). doi: https://doi.org/10.2118/15441-PA

Rognmo, A.U., Horjen, H., Fernø, M.A.: Nanotechnology for improved CO2 utilization in CCS: Laboratory study of CO2-foam flow and silica nanoparticle retention in porous media. *International Journal of Greenhouse Gas Control* **64**, 113-118 (2017). doi: https://doi.org/10.1016/j.ijggc.2017.07.010

Rossen, W.R.: Foam Generation at Layer Boundaries in Porous Media. *SPE-195310-PA* **4**(04), 409-412 (1999). doi: https://doi.org/10.2118/59395-PA

Rossen, W.R.: A critical review of Roof snap-off as a mechanism of steady-state foam generation in homogeneous porous media. *Colloids and Surfaces A: Physicochemical and Engineering Aspects* **225**(1), 1-24 (2003). doi: https://doi.org/10.1016/S0927-7757(03)00309-1

Rossen, W.R., Gauglitz, P.A.: Percolation theory of creation and mobilization of foams in porous media. *AIChE Journal* **36**(8), 1176-1188 (1990). doi: https://doi.org/10.1002/aic.690360807

Rossen, W.R., Kibodeaux, K.R., Shi, J.X., Zeilinger, S.C., Lim, M.T.: Injectivity and Gravity Override in Surfactant-Alternating-Gas Foam Processes. Paper

presented at the SPE Annual Technical Conference and Exhibition, Dallas, Texas, 1995/1/1/ 1995 of Conference. doi: https://doi.org/10.2118/30753-MS

Rossen, W.R., Wang, M.W.: Modeling Foams for Acid Diversion. *SPE-195310-PA* **4**(02), 92-100 (1999). doi: https://doi.org/10.2118/56396-PA

Saint-Jalmes, A.: Physical chemistry in foam drainage and coarsening. *Soft Matter* **2**(10), 836-849 (2006). doi: https://doi.org/10.1039/B606780H

Shah, S.Y., Wolf, K.-H., Pilus, R.M., Rossen, W.R.: Foam Generation by Capillary Snap-Off in Flow Across a Sharp Permeability Transition. *SPE-195310-PA* **24**(01), 116-128 (2019). doi: https://doi.org/10.2118/190210-PA

Shi, J.X., Rossen, W.R.: Improved Surfactant-Alternating-Gas Foam Process to Control Gravity Override. Paper presented at the SPE/DOE Improved Oil Recovery Symposium, Tulsa, Oklahoma, 1998/1/1/ 1998 of Conference. doi: https://doi.org/10.2118/39653-MS

Shokrollahi, A., Arabloo, M., Gharagheizi, F., Mohammadi, A.H.: Intelligent model for prediction of CO2 – Reservoir oil minimum miscibility pressure. *Fuel* **112**, 375-384 (2013). doi: https://doi.org/10.1016/j.fuel.2013.04.036

Stone, H.L.: Probability Model for Estimating Three-Phase Relative Permeability. *SPE-2116-PA* **22**(02), 214-218 (1970). doi: https://doi.org/10.2118/2116-PA

Svensson, R., Odenberger, M., Johnsson, F., Strömberg, L.: Transportation systems for CO2—application to carbon capture and storage. *Energy Conversion and Management* **45**(15), 2343-2353 (2004). doi: https://doi.org/10.1016/j.enconman.2003.11.022

Valavanides, M.S.: Review of Steady-State Two-Phase Flow in Porous Media: Independent Variables, Universal Energy Efficiency Map, Critical Flow Conditions, Effective Characterization of Flow and Pore Network. *Transport in Porous Media* **123**(1), 45-99 (2018). doi: https://doi.org/10.1007/s11242-018-1026-1

Vassenden, F., Holt, T.: Experimental Foundation for Relative Permeability Modeling of Foam. *SPE-190204-PA* **3**(02), 179-185 (2000). doi: https://doi.org/10.2118/62506-PA

Vassenden, F., Holt, T., Ghaderi, A., Solheim, A.: Foam Propagation on Semi-Reservoir Scale. *SPE-190204-PA* **2**(05), 436-441 (1999). doi: https://doi.org/10.2118/58047-PA

Wu, X.F., Chen, G.Q.: Global primary energy use associated with production, consumption and international trade. *Energy Policy* **111**, 85-94 (2017). doi: https://doi.org/10.1016/j.enpol.2017.09.024

Xing, D., Wei, B., McLendon, W.J., Enick, R.M., McNulty, S., Trickett, K., Mohamed, A., Cummings, S., Eastoe, J., Rogers, S., Crandall, D., Tennant, B., McLendon, T., Romanov, V., Soong, Y.: CO2-Soluble, Nonionic, Water-Soluble Surfactants That Stabilize CO2-in-Brine Foams. *SPE-195310-PA* **17**(04), 1172-1185 (2012). doi: https://doi.org/10.2118/129907-PA

Xing, D., Wei, B., Trickett, K., Mohamed, A., Eastoe, J., Soong, Y., Enick, R.M.: CO2-Soluble Surfactants for Improved Mobility Control. Paper presented at the SPE Improved Oil Recovery Symposium, Tulsa, Oklahoma, USA, 2010/1/1/ 2010. doi: https://doi.org/10.2118/129907-MS

Zeng, Y., Ma, K., Farajzadeh, R., Puerto, M., Biswal, S.L., Hirasaki, G.J.: Effect of Surfactant Partitioning Between Gaseous Phase and Aqueous Phase CO_2 Foam Transport for Enhanced Oil Recovery. *Transport in Porous Media* **114**(3), 777-793 (2016). doi: https://doi.org/10.1007/s11242-016-0743-6

Scientific Papers

International Journal of Greenhouse Gas Control 96 (2020) 103016

Contents lists available at ScienceDirect

International Journal of Greenhouse Gas Control

journal homepage: www.elsevier.com/locate/ijggc

Increased CO_2 storage capacity using CO_2-foam

T. Føyen[a,b,*], B. Brattekås[a], M.A. Fernø[a], A. Barrabino[b], T. Holt[b]

[a] Department of Physics and Technology University of Bergen, Norway
[b] SINTEF Industry, Norway

ARTICLE INFO

Keywords:
Carbon capture storage and utilization
CO_2 Storage Capacity
Decreased residual water saturations
Foam generation
Surfactant partitioning
Foam apparent viscosity
Non-ionic surfactants

ABSTRACT

Reduction of the CO_2 mobility is beneficial during subsurface sequestration of anthropogenic CO_2 in saline aquifers and hydrocarbon reservoirs by mitigating flow instabilities leading to early gas breakthrough and poor sweep efficiency. Injection of CO_2 foam is a field-proven technology for gas mobility control. Foam generation and coalescence are compared between six commercially available surfactants with a range in CO_2 solubility, during unsteady state injection of dense CO_2-foam in a long sandstone outcrop core (1.15 m). Foam generation categories and foam decay were defined based on the observed changes in foam apparent viscosity during generation and coalescence. The degree of CO_2 solubility influenced apparent viscosity development and peak foam strength for the tested surfactants. Variations in foam peak strength resulted in a range of water saturations at CO_2 breakthrough (up to 24 percentage points difference observed experimentally), with implications for the CO_2 storage capacity.

1. Introduction

Sequestration of anthropogenic CO_2 in subsurface geological formations is considered necessary in most scenarios to limit global warming to 1.5 °C (IPCC, 2018) and to meet the emission goals set forward by the Paris Agreement. For decades CO_2 has been pumped into geological formations containing hydrocarbons with the focus of enhancing the oil recovery (EOR) with variable degree of success (Lake et al., 2019), and without the focus of maximizing sequestered CO_2 in the formation. Co-optimizing CO_2 EOR, both in terms of oil produced and volumes of CO_2 stored, may act as a stepping-stone for large-scale sequestration of CO_2, because CO_2 EOR tackles the current largest obstacle to implementation; it represents an economic opportunity for the industry. The Carbon-Capture, Utilization and Storage (CCUS) value chain renders CO_2 sequestration cost efficient by establishing the necessary infrastructure and driving technology development (Ettehadtavakkol et al., 2014; Lindeberg et al., 2017).

The sweep efficiency during CO_2-EOR operations or aquifer CO_2 sequestration may be low. The low viscosity of CO_2 at reservoir conditions compared to the displaced brine and oil can cause viscous fingering, leading to early CO_2 breakthrough and high gas oil production ratios (Jones et al., 2016; Lee and Kam, 2013). Sweep efficiency challenges are further amplified in presence of reservoir heterogeneities, and result in low utilization of the injected CO_2 with lower-than-expected oil recovery, less CO_2 sequestered, and additional costs from the need to separate and recycling the produced gas. CO_2 mobility control is necessary to improve the sweep efficiency, and may be achieved using direct CO_2 thickeners (Cummings et al., 2012; Lee et al., 2014; Zhang et al., 2011) or CO_2 foam (Enick et al., 2012; Haugen et al., 2014; Vitoonkijvanich et al., 2015).

Foam can be described as discontinued gas phase, separated by a continuous thin liquid film called lamellae. Gas-flow resistance in each individual lamella is controlled by two different mechanisms: the drag associated with the viscous shear between a flowing/moving lamella (Hirasaki and Lawson, 1985), and the force needed to push a lamella through a pore throat (Falls et al., 1989). Foams are thermodynamically unstable systems and they require a stabilizer (foaming agent). The lamellae stabilization can be achieved by using surfactants or nanoparticles (Nguyen et al., 2014; Rognmo et al., 2017). Foam reduces the gas mobility more in high permeability zones relative to low permeability zones, and thus smoothen permeability contrasts (Bertin and Kovscek, 2003; Vassenden and Holt, 2000). When stable foam is present in high permeability zones fluids may be diverted into regions that have not previously been swept (Alcorn et al., 2019). The foaming agent

Abbreviations: CO_2, carbon dioxide; EOR, enhanced oil recovery; CCUS, carbon capture, utilization and storage; SAG, surfactant alternating gas; WASG, water alternating surfactant gas; SG, surfactant gas; BT, gas break through; PV, pore volume; AOS, Alpha olefin sulfonate; k, permeability; μapp, apparent viscosity; ∇p, pressure gradient; u, Darcy velocity; IFT, interfacial tension; kp, partition coefficient; Wt.%, weight percentage; $m_s^{x,t}$, mass of surfactant; $m_{CO_2}^{x-1,t-1}$, surfactant dissolved in CO_2; $m_{s,W}^{x,t-1}$, surfactant dissolved in Water; ρ_{CO_2}, CO_2 Density; S_W, water saturation

* Corresponding author at: Department of Physics and Technology University of Bergen, Norway.
E-mail address: tore.foyen@sintef.no (T. Føyen).

https://doi.org/10.1016/j.ijggc.2020.103016
Received 28 November 2019; Received in revised form 3 March 2020; Accepted 6 March 2020

must be selected for each specific case by evaluating factors such as the chemical stability at reservoir conditions, environmental concerns due to potential toxicity, economical aspects governed by price and volume of the foaming agent needed, in addition to the foaming agent ability to generate a sufficiently strong and stable foam.

Foams are dispersed systems and can only be generated when both the gaseous (dispersed) and aqueous (continuous) phases are present in the pore space, with a sufficient water fraction and concentration of foaming agent. Different injection strategies have been proposed to fulfil these requirements. Continuous foam injection, where the aqueous and gaseous phases are co-injected, is rarely used in the field (Rossen, 1995), due to operational constraints and potential injectivity issues. The most used foam injection process is Surfactant-Alternating-Gas (SAG) that mitigates the reduced injectivity expected during co-injection by generating a weaker foam near the injection well (Rossen et al., 1995), in addition to decreasing gravity override (Shan and Rossen, 2004; Shi and Rossen, 1998). When gravity-driven segregated flow occurs, interaction between the surfactant (foaming agent, aqueous phase) and gas will be limited because the phases are flowing in separate zones of the reservoir, observed by Vassenden et al. (1999) at the semi-reservoir scale.

Two modified foam injection processes have been proposed, where CO_2 soluble surfactants are dissolved in the gaseous phase to act as the foaming agent, Water-Alternating-Gas-with-Surfactant-in-Gas (WASG), and continuous Surfactant-Gas injection (SG) (Le et al., 2008). Use of CO_2 soluble surfactants may improve the utilization of the foaming agent. Foam and surfactant transport simulations during WASG by Zeng et al. (2016) concluded that the distribution of surfactant throughout the reservoir was improved when the surfactant partitions equally between the gaseous and aqueous phases (i.e. the surfactant had a partitioning coefficient of unity). Foam strength is dependent on surfactant concentration (Jones et al., 2016). McLendon et al. (2014) and Xing et al. (2012) observed a higher foam strength when using partially CO_2 soluble surfactants dissolved in both injected phases (brine and CO_2), compared to foam floods where only one of the injected phases contained surfactant. The lower foam strength may be explained by a decreasing surfactant concentration within the pore space because partitioning occurs when surfactant is only present in one phase.

This paper investigates the effect of foam on the CO_2 storage capacity during unsteady state foam floods. Results from a laboratory evaluation of six commercially available surfactants, used to generate CO_2-foam at reservoir conditions are presented. Dense CO_2 was injected into a long sandstone core initially saturated by each surfactant to investigate foam generation and decay. The same sandstone core was used for all foam floods, thoroughly cleaned between each surfactant. Uncertainties associated with core material heterogeneity and varying experimental conditions were thus diminished. A model to estimate surfactant stripping was developed and expected surfactant stripping was compared with measured foam decay.

2. Methods and materials

2.1. Rock material

The unsteady state injections were performed in a cylindrical, outcrop Bentheimer sandstone core (Table 1). Porosity was determined by weight measurements, and the liquid absolute permeability was calculated using Darcy's law with three injection rates. A single core was used during all injections to eliminate the impact from changing core properties. The core was cleaned and re-saturated with surfactant before each CO_2 injection.

Table 1
Core properties.

Length (cm)	114.8 ± 0.01
Diameter (cm)	3.79 ± 0.01
Pore Volume (ml)	301.8 ± 0.5
Porosity	0.232
Permeability (Darcy)	± 0 .15

Table 2
Composition of synthetic seawater. All salts were EMSURE salts (Merck Millipore) supplied by VWR.

Component	Concentration [wt. %]
Deionized water	96.2
NaCl	2.31
$CaCl_2 \cdot 2H_2O$	0.19
$MgCl_2 \cdot 6H_2O$	0.90
KCl	0.07
Na_2SO_4	0.33

2.2. Fluid preparation

Synthetic seawater (brine) was prepared by dissolving salts into deionized water (Table 2) and filtered through a 0.45 µm cellulose acetate filter to remove possible large particles. Five commercially available non-ionic surfactants were purchased from Sigma-Aldrich and used as foaming agents (Table 3). A $C_{14\text{-}16}$ alpha olefin sulphonate (AOS) was kindly supplied by the Stepan Company and was used as a reference anionic surfactant. Measured CO_2 partitioning coefficients (kp), *i.e.* the distribution of the surfactant between CO_2 and brine at equilibrium were used to investigate this effect on foam behaviour. A constant surfactant concentration (0.5 wt. %) in synthetic seawater was used for all surfactant solutions. The surfactant solutions were flushed with Argon to remove dissolved oxygen and stored under an Argon atmosphere. CO_2 of 99.9999 % purity was used during foam injection.

The partitioning coefficients were measured using an internally stirred windowed variable volume pVT cell from D. B. Robinson (Barrabino et al., 2020). The surfactant concentrations were determined using HPLC (Beranger and Holt, 1986). The measurements of partitioning coefficient were performed using 0.5 wt. % surfactant solutions that constituted 25 % of the total system volume, thus CO_2 constituted 75 % (Fig. 1). This volume distribution is similar to foam flooding, where end point surfactant solution saturation ranged between 9.5–21.5 % pore volume (PV).

2.3. Experimental procedure

To reduce radial CO_2 diffusion the core was wrapped in a 0.025 mm thick nickel foil before instalment in the Viton rubber sleeve in the biaxial core holder (Fig. 2). Methanol was injected to increase pore pressure, fill pore space with a liquid and to calculate porosity by measuring the difference of methanol injected and produced (adjusted for system dead volumes). Methanol was miscible displaced by several

Table 3
Surfactants used as the foaming agents. Partitioning coefficient were measured at 40°C and 200 bar.

Commercial Name	Type	kp [wt. %/wt. %]
Anionic, not CO_2-soluable		
BIO-TERGE® AS-40 (AOS)	$C_{14\text{-}16}$ sodium olefin sulfonate	0
Non-ionic, partially CO_2-soluble		
Tergitol 15-S-9	Branched alkyl ethoxylate	1.45 ± 0.14
Tergitol TMN 10	Branched alkyl ethoxylate	0.87 ± 0.01
Tergitol NP 10	Branched alkylphenol ethoxylate	0.10 ± 0.00
Igepal CO 720	Linear nonylphenol ethoxylate	0.22 ± 0.00
Brij L23	Lauryl ethoxylate.	0.02 ± 0.00

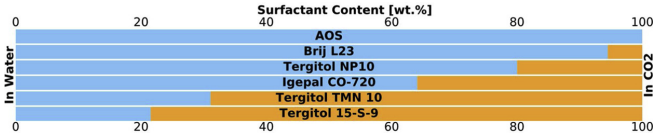

Fig. 1. The distribution of the surfactants between synthetic sea water (blue) and CO_2 (orange) at 40°C and 200 bar. AOS is not soluble in CO_2 and its content in CO_2 is therefore zero.

pore volumes of brine. The pore pressure was 200 bar and the overburden confinement pressure was 268 bar during injection of surfactant solutions and CO_2. The temperature in the heated zone was 40°C when non-ionic surfactant solutions (CO_2-soluble surfactants) were injected and 80°C when the anionic surfactant was used.

The core was fully saturated with surfactant solution when CO_2 was injected to investigate foam generation and decay. A gravity stabilized (top to bottom) CO_2 injection (as shown in Fig. 2) was used. The inline humidifier (placed upstream of the core) saturated the injected CO_2 with water vapour. Produced fluids were separated at atmospheric conditions, where the aqueous phase was collected in a graded cylinder and the produced CO_2 was vented through a two-column water adsorption unit (W. A. Hammond Drierite Comp. Ltd.). The combined mass of the produced liquids and vapour were logged on a balance, enabling calculation of the average water saturation in the core during CO_2 injections. The differential pressure across the core was logged versus time using three Fuji differential pressure transmitters of different pressure ranges (320 mbar, 5 bar and 20 bar), and reported as foam apparent viscosity μ_{app}.

$$\mu_{app} = \frac{k}{u} * \nabla p \tag{1}$$

In Eq. (1) k is the permeability, $\underline{u}$ is the Darcy velocity and ∇p is the pressure gradient.

The core temperature and inlet-, outlet-, back-pressure regulator and confinement pressures were also logged versus time during the experiments.

Two CO_2 injection schemes were used for each surfactant solution; the L-scheme and the H-scheme (Fig. 3). In the L-scheme, denoted *low* and abbreviated "L", a Darcy velocity of 2.1 ft/day (0.63 m/day) was applied during the initial part of the flooding; whereas a 32.5 ft/day (9.9 m/day) Darcy velocity, denoted *high* and abbreviated "H", was used during the initial part of the H-scheme. The injection rate was reduced within each scheme when the differential pressure and core saturation were converging towards stable conditions. For each surfactant one foam flood was performed for both injection schemes (L and H); thus, in total 12 unsteady state foam floods. The CO_2 injections with surfactant solution initially in the pore space were benchmarked against a run with brine (denoted baseline). The baseline was performed at 2.1 ft/day Darcy velocity.

The following procedure was used for all unsteady state CO_2 foam floods:

1) A minimum of 2.5 PV surfactant solution (min. 3773 mg of surfactant) was injected to satisfy surfactant adsorption, displace the brine and fully saturate the pore space with surfactant solution. Surfactant adsorption was measured in separate experiments.
2) *CO_2 was injected into the top of the vertically aligned core, using rates corresponding to either L-scheme or H-scheme injection (Fig. 3).
3) The core was cleaned by injecting solutions of 2-propanol and water and SSW (further described below), and finally re-saturated with brine.
4) Step 1) – 3) was repeated for all surfactant solutions.

2.4. Core cleaning

Surfactant solution and CO_2 was removed from the core and the flow lines between the foam floods by injection of water-based 2-propanol solutions and SSW. This involved injection of first a 2-propanol/water azeotrope (87.7 wt. % 2-propanol) followed by SSW. For some of the experiments a mixture of 0.5 wt.% NaCl with 30 wt.% 2-propanol was injected prior to SSW, and several injection cycles were done. The cleaning continued until no surfactant could be observed in the produced SSW and consistent water permeabilities were measured (2.91 ± 0.15) Darcy. The baseline CO_2 injection (no surfactant present) was performed between two of the foam injections. Foam generation was not observed during this experiment.

2.5. Surfactant mass model

A one-dimensional, piston-like displacement surfactant mass model was set up to estimate in-situ surfactant concentration and surfactant stripping during CO_2 injection. The saturation front advances one cell per time step with two possible water saturations: $S_w = S_{wr}$ behind the front and $S_w = 1$ ahead of the saturation front. S_{wr} is the residual water saturation after CO_2 flooding. The model assumes that both fluids are incompressible and that the surfactant distribution between the two phases is at local equilibrium. Surfactant adsorption and desorption at the rock-fluid interface are neglected. The total surfactant mass in a cell x at the time t ($m_s^{x,t}$) equals the sum of surfactant mass dissolved in CO_2 flowing from the upstream cell ($m_{CO_2}^{x-1,\,t-1}$) and the surfactant mass

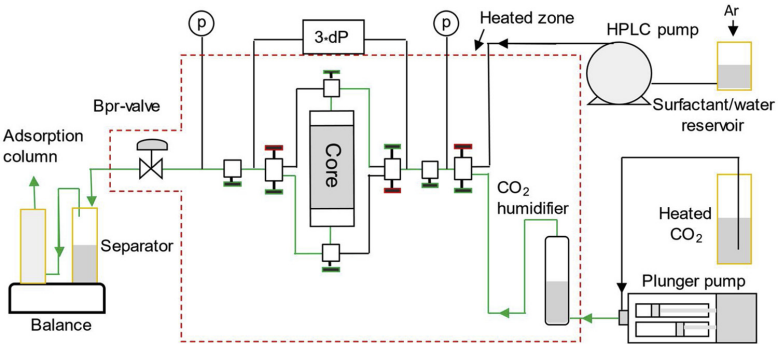

Fig. 2. Experimental setup used for the unsteady state foam experiments. Lines marked green indicates where fluids were flowing during CO_2 injection: Pure CO_2 from the Quizix Q5210 plunger pump was injected via the CO_2 humidifier and through a series of needle valves (marked green for open, red for closed) to the top of the core. Produced fluids from the bottom of the core was depressurized through the back-pressure regulator valve (BPR-valve) and collected in the separator and adsorption column placed on the balance. The HPLC pump was used to injected aqueous solutions (brine, surfactant solutions and cleaning fluids).

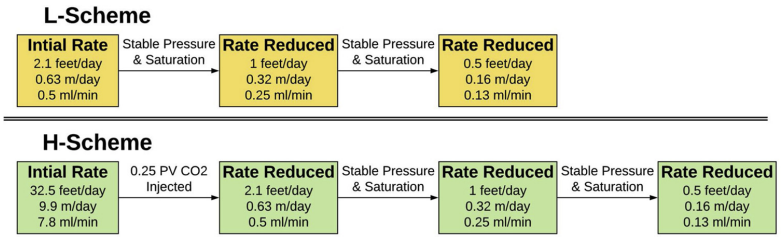

Fig. 3. L- and H- Injection schemes for foam floods. The injection rates are shown as Darcy velocities in field units ($feet/day$) or metric units (m/day) and as volumetric injection rates (ml/min). Criteria for rate change are included.

dissolved in the irreducible aqueous phase ($m_{s,W}^{x,t-1}$):

$$m_s^{x,t} = m_{s,CO_2}^{x-1,\,t-1} + m_{s,W}^{x,t-1} \tag{2}$$

The surfactant mass in residual water is assumed stagnant in the model, and the CO_2 flowing into the first cell does not contain surfactant.

Behind the saturation front, the surfactant partitions between both aqueous and gaseous phases. By assuming partitioning at local equilibrium, the relationship between the concentrations of surfactant in the two phases is given by the partitioning coefficient k_p, defined as:

$$k_p = \frac{\frac{m_{s,CO_2}}{m_{s,CO_2} + m_{CO_2}}}{\frac{m_{s,W}}{m_{s,W} + m_W}} \tag{3}$$

here m_{s,CO_2} and $m_{s,SW}$ are the masses of surfactant dissolved in the CO_2 and aqueous phase, and m_{CO_2} and m_W are the masses of CO_2 and aqueous phase, respectively. For low surfactant concentrations, the partitioning coefficient can be expressed as:

$$k_p = \frac{\frac{m_{s,CO_2}^{x,t}}{\rho_{CO_2}(1-S_W)}}{\frac{m_{s,W}^{x,t}}{(S_W)}} \tag{4}$$

where ρ_{CO_2} is the CO_2 density, the brine density is set to unity and the water saturation is S_W.

The mass of surfactant in each cell, $m_s^{x,t}$,is given by Eq. (2). The new distribution of surfactant can be calculated in water and CO_2 (at equilibrium) can be calculated by rewriting Eq. (4), giving:

$$m_{s,CO_2}^{x,t} = \frac{\frac{k_p * \rho_{CO_2}(1-S_W)}{S_W} * m_s^{x,t}}{\frac{k_p * \rho_{CO_2}(1-S_W)}{S_W} + 1} \tag{5}$$

The calculations were done for every individual cell (in total 100 cells) for each time step (0.01 PV). The total mass of surfactant present in the system, and in each phase, at a time t can be found by summarizing the individual surfactant mass of each cell.

3. Results

Experimental results from 13 core flooding experiments are given in the Fig. 4. The measured differential pressures recorded during the floods are converted to apparent viscosities using Eq. (1). The apparent viscosities versus pore volumes of CO_2 injected are plotted with a specific colour for each surfactant used consistently through the paper. The average water saturations are plotted using blue dashed lines. Reduction in rates are marked using yellow numbers (ml/min) and vertical lines. Data are available at http://doi.org/10.17632/4mp24c4jf7.1, an open-source online data repository hosted at Mendeley Data (Føyen and Holt, 2020).

Common observations for most of the floods seen in Fig. 4 are that the water saturation decreases linearly to low values (< 0.2) at breakthrough of CO_2. The linear decreases indicate that foam was generated and propagated with the same rate as the injected CO_2. Some experiments exhibited a different behaviour, however. For the H-Scheme injection with Tergitol 15-S-9 only weak foam was formed, resulting in non-piston like displacement with a early breakthrough of CO_2 production, and the low water saturation was obtained first after 1.5 PV injected CO_2. For the L-Scheme injection with Tergitol NP 10 CO_2 breakthrough occurred at 0.63 PV but strong foam was generated shortly after. The H-Scheme exhibited a similar but pronounced behaviour. CO2 breakthrough occurred at 0.69 PV. At 1.36 PV strong foam suddenly formed, and the water saturation quickly decreased to less than 0.2.

4. Discussion

4.1. Enhanced CO_2 storage using foam

The CO_2 storage capacity is here defined as the fraction of pore volume accessible for storing CO_2. The CO_2 storage capacity increased when foam was generated compared to baseline CO_2 injection without foam (Fig. 5). On average, the water saturation after 3 pore volumes of CO_2 injection ($S_{W,3PV}$) was 0.16 for the four surfactants that generated strong foam at the onset (foam generation characteristics discussed in detail below) compared to 0.34 for the baseline. Hence, the CO_2 storage capacity increased with 27 % when CO_2-foam was generated during CO_2 injection. A similar value was observed for CO_2 storage capacity at gas breakthrough (light blue) for most foam floods (except non-piston floods, marked by the red square **in** Fig. 5): The water saturation at breakthrough of CO_2, $S_{W,BT}$, was 0.21 with foam generation and 0.38 for the baseline; also a 27 % increase. The water saturation reduction observed during foam generation was attributed to increased microscopic water displacement (*i.e.* enhanced water mobilization at pore level) and can be considered as a secondary foam effect. The enhanced macroscopic sweep efficiency, the primary objective of foam injection, cannot be observed in a homogeneous sandstone core and downward injection.

A piston-like displacement of water was observed when foam was generated during CO_2 injection, with a sharp transition from water production to mainly gas production after gas breakthrough (Fig. 6). Water production continued after gas breakthrough, resulting in an additional CO_2 storage capacity of on average 6% for the foam floods (compared to 4% for the baseline).

Strong foam generation at the onset of CO_2 injection is beneficial for CO_2 storage, as the water saturation is reduced and, hence, the fraction of pore space occupied by CO_2 increases (Fig. 7). The difference between water saturations at gas breakthrough ($S_{W,BT}$) and end of injection ($S_{W,3PV}$) represents the efficiency of the CO_2-foam displacement process: a small difference indicates an efficient displacement of water and is preferable for optimizing CO_2 storage. In addition to foam generation, giving high pressure gradients, water saturation was possibly further reduced by reduced capillary forces as surfactants decrease the water/CO_2 interfacial tension (Lake et al., 2014). This becomes evident when comparing the baseline (no surfactant present, $S_{W,3PV} = 0.34$) to

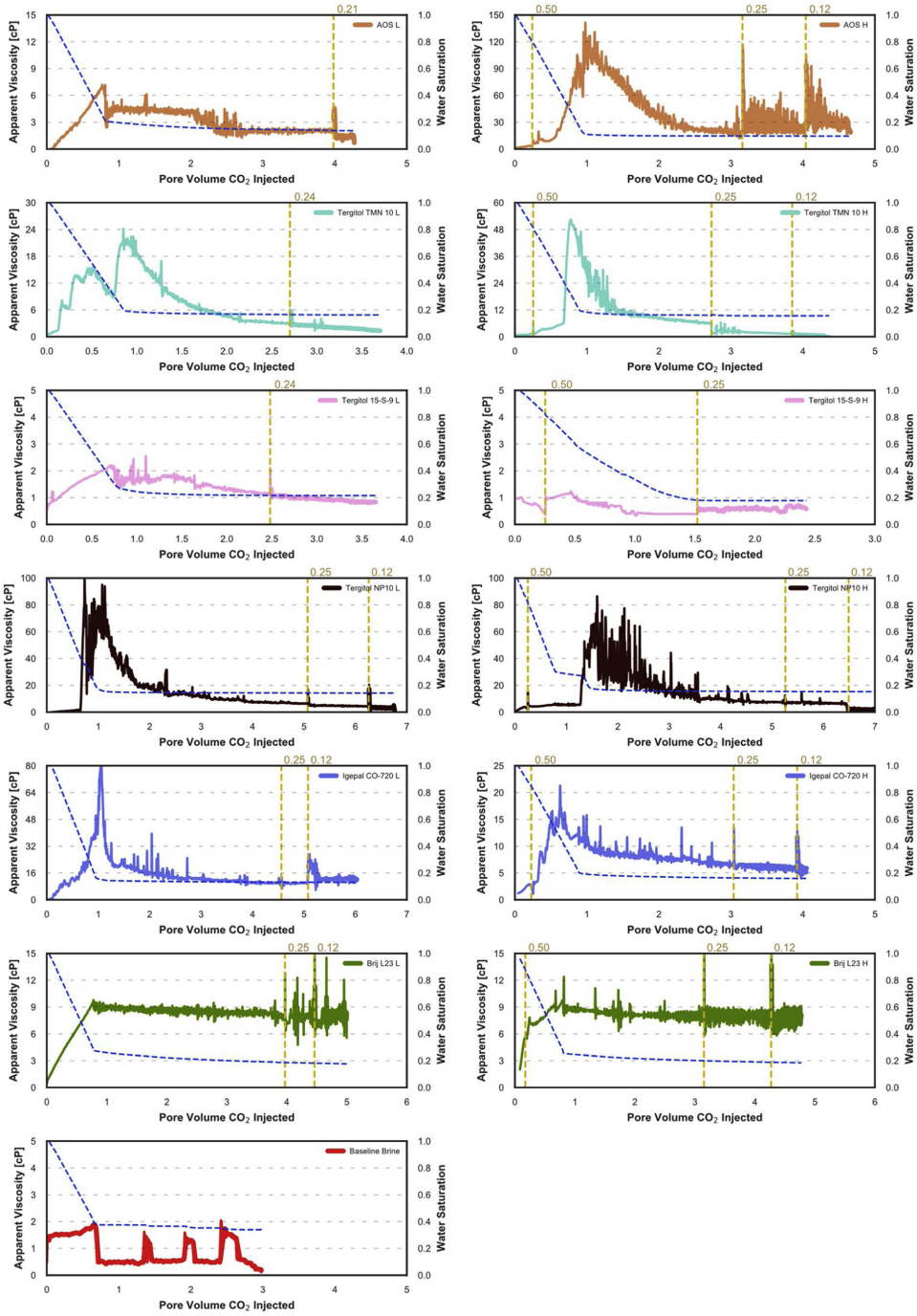

Fig. 4. Apparent viscosities (solid coloured lines) and water saturation (blue dashed lines) versus pore volumes of CO_2 injected for the foam and the baseline experiments. Left column L-scheme, right column H-scheme. Reduction in injection rate is shown using vertical yellow dashed lines, and the new rate (ml/min) is marked above.

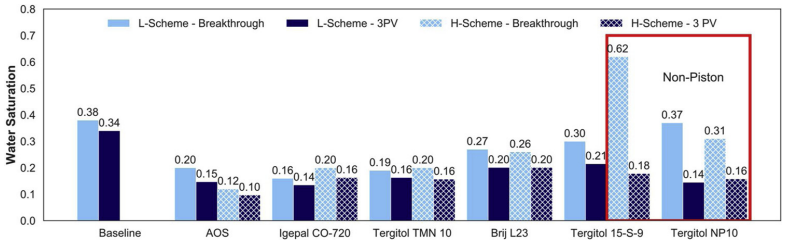

Fig. 5. Water saturations at gas breakthrough (light blue) and end of CO_2 injection (dark blue) using six commercial surfactants to generate CO_2-foam. Water saturations achieved with foam are compared to baseline CO_2 injection (no foam generated). Two CO_2 injection strategies were used: L-scheme (solid columns) and H-scheme (cross-hatched columns) for each of the six surfactants. Most CO_2-injections resulted in instant foam generation and a piston-like displacement of water, but three injections (H-scheme for Tergitol 15-S-9; L- and H-scheme for Tergitol NP10) exhibited non-piston displacement. The difference from piston-like and non-piston displacements (red rectangle) is discussed at length below.

Tergitol 15-S-9 (surfactant present, $S_{W,3PV} = 0.21$). The measured apparent viscosities for baseline and Tergitol 15-S-9 are similar (below 2 cP), but (L-scheme) end water saturations are different. Hence, the water displacement efficiency cannot be ascribed to increased differential pressures alone, but the interfacial tension reduction also contributes to low water saturations.

4.2. Onset foam generation

CO_2 foam generation, visualized by apparent viscosity calculated from differential pressure measurements (*cf.* Eq. (1)), occurred at the onset for most of the reported CO_2 injections. Foam apparent viscosity is expected to increase from the onset during unsteady state foam floods, when CO_2 advances through the core to generate foam and the viscous resistance increases. After CO_2 breakthrough the foam apparent viscosity is expected to decrease due to foam coalescence when the water saturation is reduced towards the critical saturation for the existence of foam (Vassenden and Holt, 2000), and for the CO_2 soluble surfactants; depletion of surfactant. The highest measured apparent viscosity (referred to here as *peak*) was therefore expected to be observed close to CO_2 breakthrough. Foam generation was further categorized based on the rate of apparent viscosity increase before CO_2 breakthrough:

Linear: constant foam strength behind the saturation front.

Super-linear: positive feedback by pressure gradients.

Linear apparent viscosity development demonstrates that foam is generated close to the piston-like saturation front and remained stable behind the front. The *super-linear* increase in apparent viscosity could occur due to positive feedback by pressure gradients, *i.e.* the strength of the foam depends on the pressure gradient, and the pressure gradient increases with increasing foam strength. Positive feedback is consistent with the observation of minimum pressure gradients for foam generation reported by Yu et al. (2018). The minimum pressure gradients may vary between foam systems and can be different for the surfactants described here. The AOS foam floods demonstrate both foam generation categories (Fig. 8); linear during the L-scheme foam flood and super-linear for the H-scheme. The initial short (0.25 PV injected) high injection rate period during the AOS H-scheme flooding caused a pressure gradient sufficient to generate foam 17 times stronger than what was measured during the AOS L-scheme flooding. The AOS surfactant had the highest foam strength ratio of all the surfactants tested (Table 4).

The gradient of increase in apparent viscosity was dependent on the flow velocity for the Brij L23 surfactant. The Brij L 23 H-scheme flood (Fig. 9) exhibited two separate linear gradients in increasing apparent viscosity; one prior to and one after rate reduction, of 42 and 7 cP/PV, respectively. At equal rate the H- and L-scheme linear gradients were comparable (7 cP/PV for the H-scheme and 11 cP/PV for the L-scheme). The foam generation category for both Brij L 23 foam floods was linear, although a higher gradient of increase in apparent viscosity was achieved during initial high rate injection (at a higher pressure gradient). The foam generated at the onset was, however, not strong enough to trigger a self-sustained feedback loop, hence the slope of apparent viscosity increase became close to the L-scheme at equal rates. Both Igepal CO-720 floods exhibited super-linear behaviour. The apparent viscosities for the two Tergitol 15-S-9 experiments were low, 2 cP for the L-scheme, and 1 cP for the H-scheme, which was only slightly larger than the baseline apparent viscosity (0.5 cP).

4.3. Delayed foam generation

The two Tergitol NP10 foam floods displayed delayed foam generation and did not follow the overall trend in Fig. 6. Delayed foam generation is defined here as an abrupt and rapid increase in apparent viscosity after an extended period of CO_2 injection where the foam generation was initially limited (less than 10 % of peak value). The development in apparent viscosity during delayed foam generation deviates from the linear or super-linear foam generation categories and the foam generation does not necessarily occur at the saturation front.

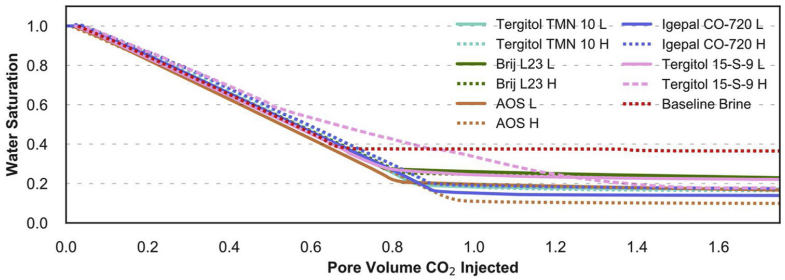

Fig. 6. Shows the water saturation versus pore volume CO_2 injected for the experiments behaving "piston-like". Tergitol 15-S-9 included to demonstrate a non-piston displacement with a non-linear reduction in water saturation when plotted against pore volumes CO_2 injected.

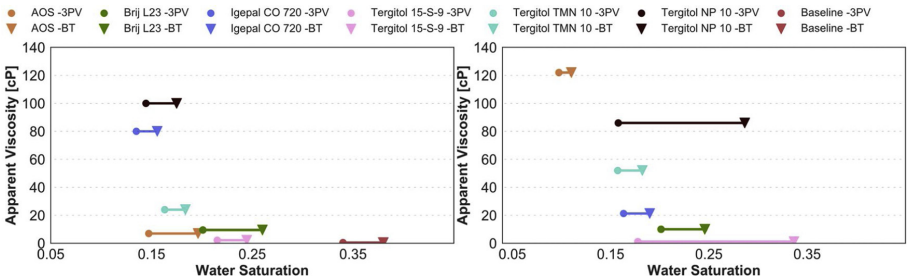

Fig. 7. Peak apparent viscosity versus water saturation at gas breakthrough (*Bt*, triangles) and after 3 PV of CO_2 injected (circles) during L-scheme (left) and H-scheme (right) for six commercial surfactants. Overall high peak apparent viscosities at breakthrough result in low water saturation and is beneficial for CO_2 storage capacity. The difference between water saturations at gas breakthrough and end of injection is indicated with a line between triangles and circles for each surfactant: short line represents an efficient displacement of water. Surfactants with delayed foam generation (Tergitol NP10 and 15-S-9) do not follow the overall trend as peak apparent viscosity occurs after gas breakthrough.

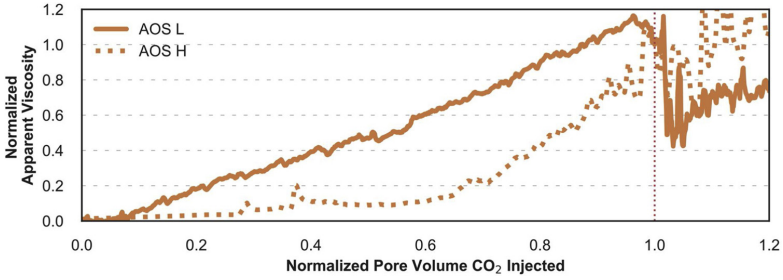

Fig. 8. Foam generation categories behaviours shown as development in apparent viscosity when CO_2 is injected exemplified by the two AOS foam floods: linear development (AOS L) and super-linear development (AOS H). Both apparent viscosity and pore volumes of CO_2 are normalized with respect to the values at gas break through.

Delayed generation of foam until gas breakthrough (Fig. 10: Tergitol NP 10, L-scheme) or later (Tergitol NP 10, H-scheme) caused an inefficient displacement of water, where the breakthrough saturation was closer to the baseline CO_2 injection. Additional storage of CO_2 was, however, achieved after foam generation due to a rapid increase in apparent viscosity and following stepwise mobilization of water. The Tergitol TMN 10 foam floods also displayed delayed foam generation, but foam generated before gas breakthrough (< 0.1 PV injected for L-scheme and 0.67 PV injected for the H-scheme) and efficient and linear reductions in water saturation were observed.

The mechanisms that determine whether foam generation occurs at the onset or is delayed are not clear. Reproducibility between all foam floods was ensured, because the same core was used, and the experimental conditions were equal and stable (except for the higher temperature used for the experiments with AOS). Variations in *e.g.* pore structure can therefore not explain the variation in foam generation behaviour. The reproducible conditions facilitate screening of surfactant (type and property) influence on foam generation- although this correlation is not straight forward. It is, however, interesting to observe that both surfactants generated foam within the same category during both L- and H-scheme floods (Table 5).

4.4. Foam decay

During unsteady-state foam floods, foam coalesce by reduction in water saturation and reduced surfactant concentration with increasing CO_2 saturation and throughput. Foam decay is identified here as consistently decreasing apparent viscosities after foam generation (Fig. 11). The CO_2 foam apparent viscosity decreased as more CO_2 was injected during L-scheme injections. The same trend was observed using the H-scheme but was less prominent. Tergitol NP 10 represents an obvious deviation from the trend due to delayed foam generation, and the low

Table 4
Foam generation categories for four surfactants used during unsteady state foam floods. The table includes the highest measured apparent viscosity for each foam flood (peak foam strength), when it was recorded (PV CO_2 injected at peak foam strength). The ratio between foam strengths during high (H) and low (L) rate foam floods are also given.

Foam flood:		Foam category	Peak foam strength:		Foam strength ratio [H/L]
Surfactant type	Injection Scheme		App visc. [cP]	Time [PV CO_2 inj.]	
AOS	L	Linear	7	0.77	17.4
	H	*Super-linear*	122	1.05	
Tergitol 15-S-9	L		2.2	0.71	0.56
	H		1.2	0.47	
Igepal CO-720	L	*Super-linear*	80	1.10	0.27
	H	*Super-linear*	21.3	0.60	
Brij L23	L	Linear	9.5	0.78	1.05
	H	Linear	10	0.80	
Baseline	L	–	0.5	–	

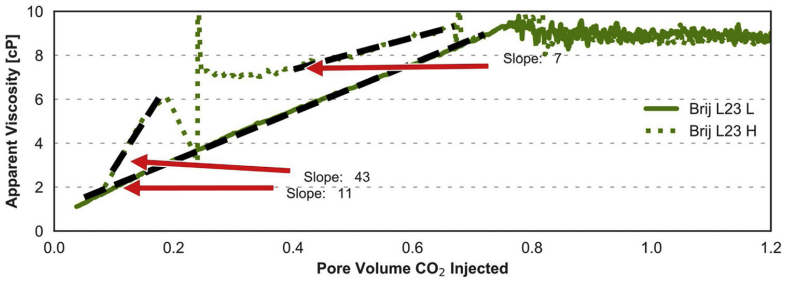

Fig. 9. Development in apparent viscosity (cP) during foam generation for the two Brij L23 experiments. The slopes of increase in apparent viscosity cP/PV are marked by dashed lines. The L-scheme had one distinct slope from the start of the experiment to gas breakthrough. The H-scheme had two distinct slopes; one prior to and one after rate reduction.

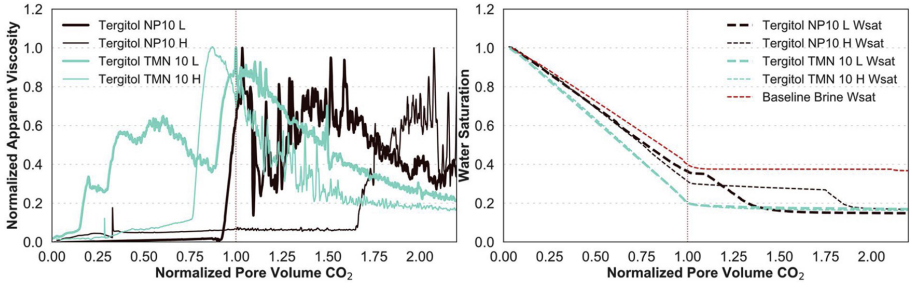

Fig. 10. Delayed foam generation was observed during CO_2 injection using surfactants Tergitol NP 10 and Tergitol TMN 10. The left figure shows apparent viscosity normalized to peak apparent viscosity, and the right figure shows water saturation development, both as functions of normalized time (PV CO_2 injected normalized to gas breakthrough). Gas breakthrough (1 PV) is indicated by the vertical red line. The water saturation profile for baseline CO_2 injection (no surfactant) is included for comparison.

Table 5
Foam generation categories for two surfactants used during unsteady state foam floods. The table includes the highest measured apparent viscosity for each foam flood (peak foam strength), when it was recorded (PV CO_2 injected at peak foam strength). The ratio between foam strengths during high (H) and low (L) rate foam floods are also given.

Foam flood:		Foam category	Peak foam strength:		Foam strength ratio [H/L]
Surfactant type	Injection Scheme		App visc [cP]	Time [PV CO2 inj]	
Tergitol TMN 10	L	Delayed	24	0.85	2.2
	H	Delayed	52	0.78	
Tergitol NP10	L	Delayed	100	0.75	0.86
	H	Delayed	86	1.60	
Baseline			0.5		

apparent viscosity observed when 1 PV CO_2 injected, resulting in foam coalescence to starting at 1.5 PV CO_2 for the H-scheme. Igepal CO-720 generated a weaker foam in the H-scheme CO_2 injection compared to the L-scheme, thus foam decay is more evident at low flow rates.

4.5. CO_2 solubility and surfactant stripping

Foam apparent viscosity depends on several factors, of which the surfactant concentration is vital (Jones et al., 2016). Surfactant stripping, where the surfactant concentration in the brine decreases due to partitioning into the CO_2, leads to reduced surfactant concentrations during unsteady state foam floods. This is of special interest when foam decay is considered. The surfactant mass balance model was used to calculate the concentration of non-ionic, partially CO_2-soluble surfactants in the core during CO_2 injection using experimentally measured partitioning coefficients (Fig. 12). The surfactant mass dissolved in CO_2 depends directly on the partitioning coefficient for each surfactant.

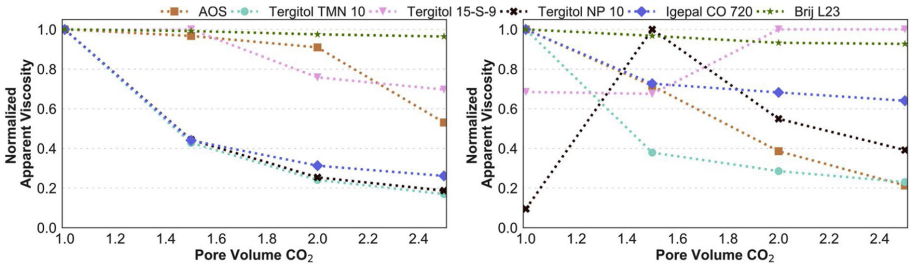

Fig. 11. Apparent viscosities plotted versus pore volumes of CO_2 injected using the L-scheme (left) and H-scheme (right). The apparent viscosities are normalized to the values measured at 1 PV injected for all experiments except Tergitol 15-S-9 H-scheme normalized at 2 PV injected and Tergitol NP10 H-scheme normalized at 1.5 PV injected.

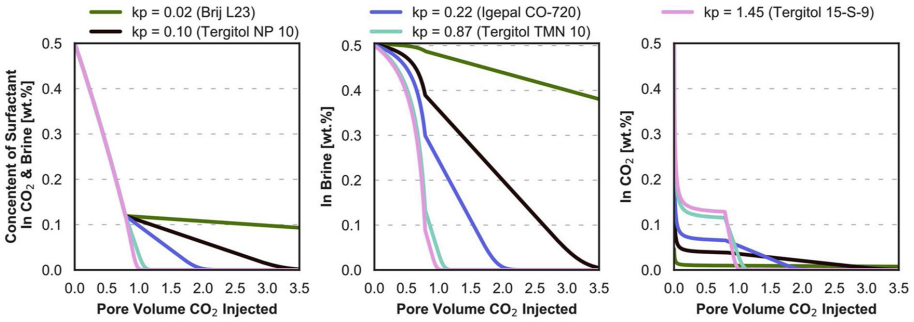

Fig. 12. Calculated total surfactant concentration (left) as a function of pore volumes CO_2 injected for different partitioning coefficient (kp). The partitioning coefficients used correspond to experimentally determined values for the five partially CO_2-soluble surfactants (see Table 3). The brand names are indicated for each kp. Surfactant concentrations in brine (middle) and CO_2 (right) are also shown. The residual water saturation was 0.2, and CO_2 density was 0.840 g/ml.

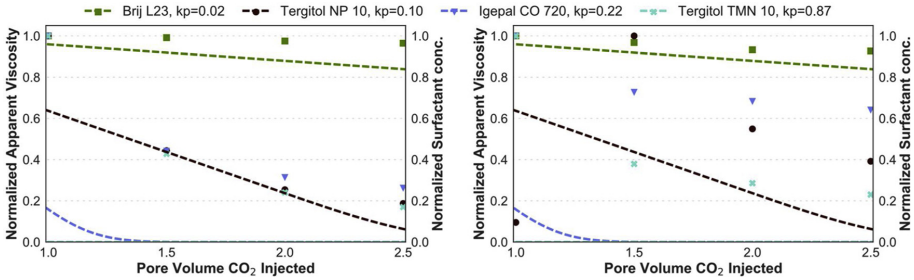

Fig. 13. Comparison between calculated surfactant concentrations using the surfactant mass balance model (dashed lines; normalized to concentration at CO_2 breakthrough) and measured apparent viscosity (points; normalized to the values measured at 1 PV injected for all experiments except Tergitol NP10 H-scheme normalized at 1.5 PV injected).

Before CO_2 breakthrough (at 0.8 PV CO_2 injected) the total surfactant concentration decreased linearly as surfactant-free CO_2 displaced the surfactant-rich brine in a piston-like manner. After CO_2 breakthrough the model assumes stagnant residual water, hence CO_2 is the only flowing phase. The model estimates a swift (low concentrations close to 1 PV injected) reduction in aqueous phase concentration due stripping of surfactants with high partitioning coefficients (kp > 0.22). Using a low (kp = 0.02) partitioning coefficient (Brij L23) resulted in a surfactant displacement that was nearly unaffected by stripping, and the total surfactant solution concentration remained almost constant after CO_2 breakthrough. In comparison, for high partitioning coefficients (Tergitol 15-S-9 and TMN 10) the total surfactant concentrations were essentially reduced to 0 after less than 1.25 pore volumes of CO_2 injected. Model results were compared with measured foam decay data (Fig. 13) using partitioning coefficients kp = 0.02 - 0.87, where foam decay is represented as normalized apparent viscosity. For surfactants not influenced by stripping (Brij L23) the model match experimental data well for both L- and H-scheme CO_2 injection. For the surfactants where surfactant stripping becomes important (high kp: Tergitol TMN10 and Igepal CO-720), the match is poor because the model estimates that surfactant concentrations reach 0 before 2 PV CO_2 injected whereas the measured apparent viscosities remained above 20 % of peak value after 2 PV CO_2 injected for both injection schemes.

Surfactant at the water-gas interface (*i.e.* lamellae) provides the lamella of self-healing capacity (Gibbs-Marangoni elasticity) which is the most important mechanism that stabilizes foam (Georgieva et al., 2009). The present model assumes local equilibrium for surfactant partitioning but does not account for surfactant adsorption on rock surfaces or at fluid interfaces. The kinetics of surfactant transport between the interfaces, the bulk fluids and the rock are not captured in the simplified model. Furthermore, adsorbed surfactant act as reservoirs of surfactant not included in the mass balance. Their magnitudes depend on the level of adsorption that can vary significantly depending on the type of surfactant. Additional complicating factors are that both the partitioning coefficients, the adsorption and foam strength depend on the surfactant concentration. The latter factor was observed for two of the present surfactants in steady state foam injection experiments (80 % foam quality, 200 bar and 40 °C) where the apparent viscosity measured for Igepal CO 720 at 0.013 wt.% surfactant was 12 % of the value measured for 0.5 wt. %. For Brij L23 the apparent viscosity measured at 0.010 wt.% surfactant was 71 % of the value measured for 0.5 wt. % (data not yet published).

All the simplifications inherent in the present model is demonstrated by results seen in Fig. 13. When the model predicts zero surfactant concentration in the core significant apparent viscosities are still observed. This show that surfactant was present in the core stabilising foam for several PVs of CO_2 injected after gas breakthrough.

The ability of surfactant to continue foam stabilization despite surfactant stripping can be beneficial during field scale application of CO_2 soluble surfactants, where the limited volume of injected surfactant (significantly less than one pore volume) can possibly be more efficiently utilized. Analyses using improved models that include the physical phenomena discussed above should be done in order to understand and reproduce the observed behaviour. This will also require additional laboratory data input such as the concentration dependence of the surfactant partitioning coefficients, surfactant adsorption/desorption isotherms and foam strength at variable surfactant concentrations. The kinetics of surfactant partitioning between fluids (the local equilibrium assumption) should also be studied. The kinetics can be important for laboratory time scale experiments but possibly less

important for reservoir scale behaviour.

5. Conclusions

CO_2-foam floods were stabilized by five non-ionic surfactants with varying degree of CO_2 solubility (partitioning coefficients) and one anionic surfactant insoluble in CO_2. The main observations during unsteady state foam floods were:

- All the tested surfactants generated foam, but the foam strength expressed as apparent viscosities varied depending on the surfactant used. For the anionic surfactant the initial injection rate of CO_2 affected the apparent viscosity significantly but had less impact for the non-ionic surfactants.
- Three categories of foam generation behaviour were observed. The build-up of foam in the core as function of the amount of CO_2 injected was characterised as linear, super-linear and delayed. The mechanism controlling foam generation category must be connected to the surfactant type and properties, as the core and experimental conditions were similar during 12 foam floods.
- Surfactant stripping into the flowing CO_2 caused continuous reductions in the surfactant concentration in the brine. This mass transfer was estimated using a simplified model. The observed foam decays were generally much slower than the estimated reductions in surfactant concentration. Surfactant adsorption on rock surfaces and at fluid interfaces were not included in the model. Adsorbed surfactant will act as reservoirs of surfactant depend on the level of adsorption. Additional complicating factors are that both the partitioning coefficients, the adsorption and foam strength depend on the surfactant concentration. A more detailed model of the physical phenomenon taking place is thus needed in order to fully understand the observed behaviours.
- Generation of foam combined with reduced water/CO_2 interfacial tensions during CO_2-foam floods yielded decreased residual water saturations compared to the baseline experiment without surfactant. This improvement in microscopic displacement comes in addition to the improved volumetric sweep expected by foam, implying increased storage capacity for sequestered CO_2.

Data availability

Datasets from the 13 core floods related to this article can be found at http://doi.org/10.17632/4mp24c4jf7.1, an open-source online data repository hosted at Mendeley Data (Føyen and Holt, 2020).ng.

CRediT authorship contribution statement

T. Føyen: Investigation, Formal analysis, Visualization, Writing - original draft. **B. Brattekås:** Writing - review & editing. **M.A. Fernø:** Writing - review & editing, Formal analysis. **A. Barrabino:** Investigation, Writing - review & editing. **T. Holt:** Project administration, Investigation, Writing - review & editing.

Declaration of Competing Interest

None.

Acknowledgements

Financial support from the Research Council of Norway is acknowledged for three ongoing projects: Improved performance of CO_2 EOR and underground storage by mobility control of CO_2 project no. 267859; Nanoparticles to Stabilize CO_2-foam for Efficient CCUS in Challenging Reservoirs project no. 268216; Subsurface Carbonate CO_2 Storage and Security project no. 280341; and for funding of PhD candidate Tore Føyen.

Appendix A. Supplementary data

Supplementary material related to this article can be found, in the online version, at doi:https://doi.org/10.1016/j.ijggc.2020.103016.

References

Alcorn, Z.P., Fredriksen, S.B., Sharma, M., Rognmo, A.U., Føyen, T.L., Fernø, M.A., Graue, A., 2019. An Integrated Carbon-Dioxide-Foam Enhanced-Oil-Recovery Pilot Program With Combined Carbon Capture, Utilization, and Storage in an Onshore Texas Heterogeneous Carbonate Field. Society of Petroleum Engineershttps://doi.org/10.2118/190204-PA.

Barrabino, A., Holt, T., Lindeberg, E., 2020. Partitioning of non-ionic surfactants between CO2 and brine. J. Pet. Sci. Eng. https://doi.org/10.1016/j.petrol.2020.107106.

Beranger, A., Holt, T., 1986. Middle and heavy α-olefin sulfonates. Tenside detergents 23, 247–254.

Bertin, H.J., Kovscek, A.R., 2003. Foam mobility in heterogeneous porous media. Transp. Porous Media 52, 17–35. https://doi.org/10.1023/A:1022312225868.

Cummings, S., Xing, D., Enick, R., Rogers, S., Heenan, R., Grillo, I., Eastoe, J., 2012. Design principles for supercritical CO2 viscosifiers. Soft Matter 8, 7044–7055. https://doi.org/10.1039/C2SM25735A.

Enick, R.M., Olsen, D.K., Ammer, J.R., Schuller, W., 2012. In: Mobility and Conformance Control for CO2 EOR via Thickeners, Foams, and Gels – A Literature Review of 40 Years of Research and Pilot Tests, SPE Improved Oil Recovery Symposium. Society of Petroleum Engineers, Tulsa, Oklahoma, USA. pp. 12. https://doi.org/10.2118/154122-MS.

Ettehadtavakkol, A., Lake, L.W., Bryant, S.L., 2014. CO2-EOR and storage design optimization. Int. J. Greenh. Gas Control. 25, 79–92. https://doi.org/10.1016/j.ijggc.2014.04.006.

Falls, A.H., Musters, J.J., Ratulowski, J., 1989. The Apparent Viscosity of Foams in Homogeneous Bead Packs. SPE-18069-PA 4. pp. 155–164. https://doi.org/10.2118/16048-PA.

Føyen, T., Holt, T., 2020. Core floods, increased CO2 storage capacity using CO2-foam, Mendeley Data. https://doi.org/10.17632/4mp24c4jf7.1.

Georgieva, D., Cagna, A., Langevin, D., 2009. Link between surface elasticity and foam stability. Soft Matter 5, 2063–2071. https://doi.org/10.2118/16048-PA.

Haugen, Å., Mani, N., Svenningsen, S., Brattekås, B., Graue, A., Ersland, G., Fernø, M.A., 2014. Miscible and immiscible foam injection for mobility control and EOR in fractured oil-wet carbonate rocks. Transp. Porous Media 104, 109–131. https://doi.org/10.1007/s11242-014-0323-6.

Hirasaki, G.J., Lawson, J.B., 1985. Mechanisms of Foam Flow in Porous Media: Apparent Viscosity in Smooth Capillaries. SPE-12129-PA 25. pp. 176–190. https://doi.org/10.2118/12129-PA.

IPCC, 2018. In: Masson-Delmotte, V., Zhai, P., Pörtner, H.-O., Roberts, D., Skea, J., Shukla, P.R., Pirani, A., Moufouma-Okia, W., Péan, C., Pidcock, R., Connors, S., Matthews, J.B.R., Chen, Y., Zhou, X., Gomis, M.I., Lonnoy, E., Maycock, T., Tignor, M., Waterfield, T. (Eds.), Summary for Policymakers, In: Global Warming If 1.5 C. An IPCC Special Report on the impacts of global warming of 1.5C above pre-industrial levels and related global greenhouse pathways, in the context of strengthening the global reponse to threat of climate change, sustainable development, and effort to eradicate poverty, Geneva, Switzerland, pp. 1–30.

Jones, S.A., Laskaris, G., Vincent-Bonnieu, S., Farajzadeh, R., Rossen, W.R., 2016. Effect of surfactant concentration on foam: From coreflood experiments to implicit-texture foam-model parameters. J. Ind. Eng. Chem. 37, 268–276. https://doi.org/10.1016/j.jiec.2016.03.041.

Lake, L.W., Johns, R.T., Rossen, R.W., Pope, G.A., 2014. Fundamentals of Enhanced Oil Recovery, second ed. Society of Petroleum Engineers, Richardson.

Lake, L.W., Lotfollahi, M., Bryant, S.L., 2019. Chapter 2 - CO2 enhanced oil recovery experience and its messages for CO2 storage. In: Newell, P., Ilgen, A.G. (Eds.), Science of Carbon Storage in Deep Saline Formations. Elsevier, pp. 15–31. https://doi.org/10.1016/B978-0-12-812752-0.00002-2.

Le, V.Q., Nguyen, Q.P., Sanders, A., 2008. A Novel Foam Concept With CO2 Dissolved Surfactants, SPE Symposium on Improved Oil Recovery. Society of Petroleum Engineers, Tulsa, Oklahoma, USA, pp. 15. https://doi.org/10.2118/113370-MS.

Lee, S., Kam, S.I., 2013. Chapter 2 - enhanced oil recovery by using CO2 foams: fundamentals and field applications. In: Sheng, J.J. (Ed.), Enhanced Oil Recovery Field Case Studies. Gulf Professional Publishing, Boston, pp. 23–61. https://doi.org/10.1016/B978-0-12-386545-8.00002-6.

Lee, J.J., Cummings, S., Dhuwe, A., Enick, R.M., Beckman, E.J., Perry, R., O'Brien, M., Doherty, M., 2014. In: Society of Petroleum Engineers, Tulsa, Oklahoma, USA. Development of Small Molecule CO2 Thickeners for EOR and Fracturing, SPE Improved Oil Recovery Symposium 18https://doi.org/10.2118/169039-MS.

Lindeberg, E., Grimstad, A.-A., Bergmo, P., Wessel-Berg, D., Torsæter, M., Holt, T., 2017. Large Scale Tertiary CO2 EOR in Mature Water Flooded Norwegian Oil Fields. Energy Procedia 114, 7096–7106. https://doi.org/10.1016/j.egypro.2017.03.1851.

McLendon, W.J., Koronaios, P., Enick, R.M., Biesmans, G., Salazar, L., Miller, A., Soong, Y., McLendon, T., Romanov, V., Crandall, D., 2014. Assessment of CO2-soluble non-ionic surfactants for mobility reduction using mobility measurements and CT imaging. J. Pet. Sci. Eng. 119, 196–209. https://doi.org/10.1016/j.petrol.2014.05.010.

Nguyen, P., Fadaei, H., Sinton, D., 2014. Pore-scale assessment of nanoparticle-stabilized CO2 foam for enhanced oil recovery. Energy Fuels 28, 6221–6227. https://doi.org/10.1021/ef5011995.

Rognmo, A.U., Horjen, H., Fernø, M.A., 2017. Nanotechnology for improved CO2 utilization in CCS: laboratory study of CO2-foam flow and silica nanoparticle retention in

porous media. Int. J. Greenh. Gas Control. 64, 113–118. https://doi.org/10.1016/j.ijggc.2017.07.010.
Rossen, W.R., 1995. Foams in Enhanced Oil Recovery, Foams: Theory: Measurements: Applications. Marcel Dekker, New York, pp. 413–464.
Rossen, W.R., Kibodeaux, K.R., Shi, J.X., Zeilinger, S.C., Lim, M.T., 1995. Injectivity and Gravity Override in Surfactant-Alternating-Gas Foam Processes, SPE Annual Technical Conference and Exhibition. Society of Petroleum Engineers, Dallas, Texas, pp. 12. https://doi.org/10.2118/30753-MS.
Shan, D., Rossen, W.R., 2004. Optimal Injection Strategies for Foam IOR. SPE-180051-PA 9. pp. 132–150.
Shi, J.X., Rossen, W.R., 1998. In: Improved Surfactant-Alternating-Gas Foam Process to Control Gravity Override, SPE/DOE Improved Oil Recovery Symposium. Society of Petroleum Engineers, Tulsa, Oklahoma. pp. 132–150. https://doi.org/10.2118/88811-PA.
Vassenden, F., Holt, T., 2000. Experimental Foundation for Relative Permeability Modeling of Foam. SPE-58047-PA 3. pp. 179–185. https://doi.org/10.2118/62506-PA.
Vassenden, F., Holt, T., Ghaderi, A., Solheim, A., 1999. Foam Propagation on Semi-Reservoir Scale. SPE-58047-PA 2. pp. 436–441. https://doi.org/10.2118/58047-PA.
Vitoonkijvanich, S., AlSofi, A.M., Blunt, M.J., 2015. Design of foam-assisted carbon dioxide storage in a North Sea aquifer using streamline-based simulation. Int. J. Greenh. Gas Control. 33, 113–121. https://doi.org/10.2118/58047-PA.
Xing, D., Wei, B., McLendon, W.J., Enick, R.M., McNulty, S., Trickett, K., Mohamed, A., Cummings, S., Eastoe, J., Rogers, S., Crandall, D., Tennant, B., McLendon, T., Romanov, V., Soong, Y., 2012. CO2-Soluble, Nonionic, Water-Soluble Surfactants that Stabilize CO2-in-Brine Foams. SPE-180051-PA 17. pp. 1172–1185. https://doi.org/10.2118/129907-PA.
Yu, G., Rossen, W.R., Vincent-Bonnieu, S., 2018. Foam Generation with Flow Rate: Effect of Surfactant Concentration and Gas Fraction, SPE EOR Conference at Oil and Gas West Asia. Society of Petroleum Engineers, Muscat, Oman, pp. 13. https://doi.org/10.2118/190398-MS.
Zeng, Y., Ma, K., Farajzadeh, R., Puerto, M., Biswal, S.L., Hirasaki, G.J., 2016. Effect of surfactant partitioning between gaseous phase and aqueous phase on CO2 foam transport for enhanced oil recovery. Transp. Porous Media 114, 777–793. https://doi.org/10.1007/s11242-016-0743-6.
Zhang, S., She, Y., Gu, Y., 2011. Evaluation of polymers as direct thickeners for CO2 enhanced oil recovery. J. Chem. Eng. Data 56, 1069–1079. https://doi.org/10.1021/je1010449.

nanomaterials

MDPI

Article

Pore- and Core-Scale Insights of Nanoparticle-Stabilized Foam for CO_2-Enhanced Oil Recovery

Zachary Paul Alcorn [1,*], Tore Føyen [1,2], Jarand Gauteplass [1], Benyamine Benali [1], Aleksandra Soyke [1] and Martin Fernø [1]

[1] Department of Physics and Technology, University of Bergen, 5007 Bergen, Norway; tore.foyen@uib.no (T.F.); Jarand.Gauteplass@uib.no (J.G.); Benyamine.benali@uib.no (B.B.); aleksandra.soyke@uib.no (A.S.); Martin.Ferno@uib.no (M.F.)

[2] SINTEF Industry, Norway

* Correspondence: zachary.alcorn@uib.no

Received: 4 September 2020; Accepted: 17 September 2020; Published: date

Abstract: Nanoparticles have gained attention for increasing the stability of surfactant-based foams during CO_2 foam-enhanced oil recovery (EOR) and CO_2 storage. However, the behavior and displacement mechanisms of hybrid nanoparticle–surfactant foam formulations at reservoir conditions are not well understood. This work presents a pore- to core-scale characterization of hybrid nanoparticle–surfactant foaming solutions for CO_2 EOR and the associated CO_2 storage. The primary objective was to identify the dominant foam generation mechanisms and determine the role of nanoparticles for stabilizing CO_2 foam and reducing CO_2 mobility. In addition, we shed light on the influence of oil on foam generation and stability. We present pore- and core-scale experimental results, in the absence and presence of oil, comparing the hybrid foaming solution to foam stabilized by only surfactants or nanoparticles. Snap-off was identified as the primary foam generation mechanism in high-pressure micromodels with secondary foam generation by leave behind. During continuous CO_2 injection, gas channels developed through the foam and the texture coarsened. In the absence of oil, including nanoparticles in the surfactant-laden foaming solutions did not result in a more stable foam or clearly affect the apparent viscosity of the foam. Foaming solutions containing only nanoparticles generated little to no foam, highlighting the dominance of surfactant as the main foam generator. In addition, foam generation and strength were not sensitive to nanoparticle concentration when used together with the selected surfactant. In experiments with oil above miscibility conditions, foam was readily generated using all the tested foaming solutions. Core-scale foam-apparent viscosities with oil were nearly three times as high as experiments without oil present due to the development of stable oil/water emulsions and their combined effect with foam for reducing CO_2 mobility

Keywords: nanoparticles; foam; CO_2 EOR; CO_2 mobility control

1. Introduction

An energy transition to a net-zero society is a global challenge in need of affordable, low-risk technologies. Carbon capture, utilization and storage (CCUS) is a crucial technology for substantial emission cuts for many energy-intensive industries to achieve the ambitious climate goals of the Paris Agreement [1]. CCUS involves capturing CO_2 from industrial sources and injecting it into subsurface reservoirs for simultaneous storage and energy production, via CO_2-enhanced oil recovery (EOR). Permanent CO_2 storage coupled with CO_2 EOR can provide affordable and reliable energy for our developing world while reducing the life-cycle carbon emissions of fossil fuels.

CO_2 EOR has been developed and widely implemented over the past 50 years. CO_2 is an excellent solvent in EOR processes because it is miscible with most crude oils at reservoir conditions. Above miscibility conditions, CO_2 swells the oil and reduces its viscosity resulting in increased recovery. Laboratory corefloods have reported high microscopic displacement efficiency and oil recoveries of nearly 100% [2]. However, field-scale operations often report lower than expected recoveries due to poor sweep efficiency and high CO_2 mobility [3,4]. These issues stem from reservoir heterogeneity and the low viscosity and density of CO_2 compared to reservoir fluids.

CO_2 foam can mitigate the impacts of high CO_2 mobility and reservoir heterogeneity by effectively increasing CO_2 viscosity, reducing its relative permeability and diverting CO_2 flow from high permeability zones [5]. CO_2 foam is generated in porous media by injecting foaming solution with CO_2, either simultaneously or in alternating slugs. The foam is a dispersion of CO_2 in liquid where stable liquid films, called lamellae, block some of the pathways for CO_2 flow [6]. Lamellae are commonly stabilized by surfactants. However, surfactant-stabilized foams can break down in the reservoir due to surfactant adsorption, the presence of oil, and at elevated temperatures and salinities. Therefore, their ability to reduce CO_2 mobility can be limited. The addition of silica nanoparticles to the surfactant-stabilized CO_2 foam has been shown to increase the strength and stability of the foam system and provide increased oil recovery [7,8].

Spherical silica nanoparticles are the most commonly used for EOR applications [9]. They are particles with a size up to 100 nm with intrinsic properties different from those found in the bulk of the material due to their high surface-to-volume ratio. Stable emulsions are generated using nanoparticles because a rigid monolayer is formed on the droplet surface because the particles are irreversibly attached to the interface. These emulsions may withstand high-temperature reservoir conditions without agglomeration and the nanoparticles may be further surface-treated to improve stability in harsh conditions. In addition, the small size of the particles, two orders of magnitude smaller than colloidal particles, make them suitable for flow through small pore throats in rock [10,11].

Whether stabilized by surfactants, nanoparticles, or a combination of both, bulk foams are typically composed of bubbles smaller than the containers they are within whereas foam in porous media is composed of bubbles about the same size or larger as the pore space [12]. For foam to generate, lamella creation must exceed lamella destruction. Capillary forces dominate lamella creation by three main mechanisms: leave behind, snap-off and lamella division [5,13].

An issue with foam for EOR applications is the impact of oil on foam (lamellae) stability. Many studies report that oil hinders foam generation and can destabilize already generated foam [14–16]. However, these findings are mostly based upon bulk tests at immiscible conditions with surfactant-stabilized foam, which may not necessarily represent foam in porous media and miscibility conditions for CO_2 and oil. In any case, foam behavior in the presence of oil involves several interactions between the foam, oil, and rock, which may be either detrimental or beneficial to the foam process [17,18]. These interactions include emulsification–imbibition, pseudo emulsions, and entering and spreading [19,20].

In the absence of oil, foam coalescence can reduce the number of bubbles by two mechanisms: texture (bubble size) coarsening by diffusion, often referred to as Ostwald ripening, or capillary suction drainage [21]. Diffusion occurs by the transport of gas from smaller bubbles to larger bubbles, with lower internal pressure, which results in fewer bubbles [22,23]. Capillary suction drainage occurs when the water saturation approaches a saturation value where the lamellae are no longer stable, as the capillary pressure exceeds the maximum disjoining pressure of the foam film and drains the lamellae [24,25].

The majority of earlier work has focused on foam generation and the coalescence of surfactant-stabilized CO_2 foams in the absence and presence of oil at immiscible conditions. However, much less is known about the role of nanoparticles in the absence and presence of oil at miscible conditions. Thus, this study aimed to thoroughly characterize the dominant foam generation mechanisms and determine the role of nanoparticles for stabilizing CO_2 foam and reducing CO_2 mobility. In addition, we shed light on the influence of oil on foam generation and stability. We present a pore- to core-

scale characterization of hybrid nanoparticle–surfactant foam formulation for CO_2 mobility control for CO_2 EOR and CO_2 storage. Experimental results compared the hybrid foaming solution to foam stabilized by only surfactant or nanoparticles, in the presence and absence of oil.

2. Materials and Procedures

2.1. Pore-Scale System

Two foaming agents were used to study foam generation, stability and coalescence. One was a nonionic surfactant (Huntsman *Surfonic L24-22*), a linear ethoxylated alcohol. The other foaming agent was a surface-modified spherical silica nanoparticle (Nouryon *Levasil CC301*). Foaming solutions were made by dissolving each foaming agent, either separately or combined, in 35,000 ppm NaCl brine at the concentrations shown in Table 1. CO_2 with 99.999% purity was used. The pore space was cleaned between injection cycles using 2-proponal-water azeotrope (IPA). For experiments in the presence of oil, a refined oil (n-Decane, $C_{10}H_{22}$) was used to obtain first-contact miscibility with CO_2.

Table 1. Composition of the foaming solutions used in pore- and core-scale experiments.

Foaming Agents	Concentration, *Component*	Scale
Nanoparticle (NP)	1500 ppm, *Levasil CC301*	Pore
Surfactant (SF)	3500 ppm, *Surfonic L24-22*	Core
	5000 ppm, *Surfonic L24-22*	Pore and Core
Hybrid (SF + NP)	3500 ppm, *Surfonic L24-22* + 1500 ppm, *Levasil CC301*	
	5000 ppm, *Surfonic L24-22* + 1500 ppm, *Levasil CC301*	Pore
	5000 ppm, *Surfonic L24-22* + 150 ppm, *Levasil CC301*	
	3500 ppm, *Surfonic L24-22* + 150 ppm, *Levasil CC301*	Core

The micromodel was composed of a rectangular etched silicon wafer with an irregular porous structure bonded to a transparent borosilicate glass with dimensions of 26.96 mm × 22.50 mm (Figure 1) and a constant etching depth of 30 μm. The pore pattern was a simplified two-dimensional projection of real pore structures with connected pores that allow flow with discontinuous, irregularly shaped grains that provide tortuosity. The chemical composition of the crystalline silicon and borosilicate glass are similar to sandstone and are chemically inert to the injected fluids. Complete manufacturing procedures can be found elsewhere [26,27].

The micromodel had a porosity of 61%, permeability of 3000 mD and pore volume (PV) of 11.1 μL. The porous pattern (27,000 grains) had 36 (4 × 9) repetitions of a pore network with 749 unique grains. The grain size distribution of the 749-grain pattern ranged between 100 and 79,000 μm^2 and the pore throat width distribution ranged from 10 to 200 μm. Flow ports were located at each corner of the micromodel with the inlet at ports 1 and 2 and the outlet at ports 3 and 4. The micromodel was positioned in the bottom part of a two-piece polyether ether ketone (PEEK) plastic micromodel holder. The top part had an open window for direct visual observation. The micromodel holder was placed on a motorized stage below a microscope (Axio Zoom. V16, Zeiss). The microscope software controlled the zoom, focus, illuminator intensity, imaging, and the motorized stage. Additional details on the micromodel set-up can be found in [28].

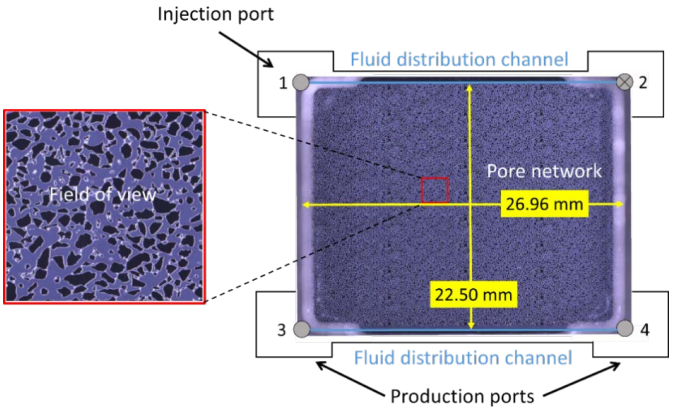

Figure 1. Dimensions of the micromodel, location of the flow ports and the fluid distribution channels. The focused field of view is shown on the left. Injection was into port 1 and production was from ports 3 and 4. Port 2 was closed. The entire pore network consisted of 36 repetitions of a single 749-grain pore pattern. The grain size distribution ranged from 100 to 79,000 μm^2 and the pore throat distribution ranged from 10 to 200 μm. The average pore throat length was 89 μm.

2.2. Pore-Scale Procedure

The micromodel system was pressurized to 100 bars using a backpressure system at 25 °C for experiments in the absence and presence of oil. For experiments in the absence of oil, foaming solution was first injected to completely saturate the micromodel before injecting dense (liquid) phase CO_2 at a constant volumetric flow rate of 4 μL/min. The foaming solutions consisted of 1500 ppm nanoparticles, 5000 ppm surfactant, and two hybrid solutions with 5000 ppm surfactant combined with 1500 ppm or 150 ppm nanoparticles. An overview of the foaming solutions are listed in Table 1. A baseline, without foaming solution, was also conducted for comparison. For experiments in the presence of oil, the micromodel was initially saturated with distilled water before injecting six pore volumes of oil. Distilled water was then injected for an additional six pore volumes to achieve residual oil saturation. The micromodel was then saturated with the hybrid 3500 ppm surfactant and 1500 ppm nanoparticle foaming solution before CO_2 injection began at a constant rate of 1 μL/min. For all experiments, CO_2 was injected in port 1 (inlet), port 2 was closed and ports 3 and 4 (outlet) were open and kept at 100 bars using the backpressure system (Figure 1). The microscope settings (light intensity, aperture, and shutter time) were optimized for image processing and remained constant. Images were acquired of the entire micromodel with high spatial resolution (4.38 μm/pixel) by stitching multiple overlapping images. The image acquisition time of the porous pattern (121 separate images) was 73 s. A focused field of view was selected, which was representative of the remainder of the micromodel, for detailed analysis and to minimize the capillary end effects. Raw images from the experiments show the grains as dark and opaque and the pore space in a grayish-blue hue. The gas/liquid interfaces (lamellae) were white due to the diffusive ring-illuminator of the microscope. Foam generation and coalescence were also analyzed by utilizing the Python Library OpenCV [29] to identify bubble number and size.

2.3. Core-Scale System

The core-scale experiments used the same brine as the pore-scale work. In experiments with only surfactant in the foaming solution, a 3500 ppm or 5000 ppm concentration was used. In experiments with the hybrid foaming solutions, a 3500 ppm surfactant concentration was used with either 1500 ppm or 150 ppm nanoparticles to evaluate the concentration sensitivity for foam stabilization. See Table 1 for an overview of the foaming solutions. A single outcrop Bentheimer sandstone core was used for all experiments to eliminate the impacts of variable core properties. The core was cleaned

and dried before being 100% saturated with brine under vacuum. Porosity and pore volumes were calculated based on the weight differential before and after saturation. Absolute permeability was measured between each experiment by injecting brine until a stable differential pressure was obtained for three different injection rates. The permeability of the core was 1400 millidarcy with a porosity of 24% (Table 2).

Table 2. Core properties of the Bentheimer sandstone used in the experimental work.

Core Properties	Value
Length (cm)	24.6 ± 0.01
Diameter (cm)	3.64 ± 0.01
Pore Volume (mL)	68.23
Porosity	0.24
Permeability (mD)	1400

2.4. Core-Scale Procedure

The brine-saturated sandstone core was wrapped in a 0.1-mm thick nickel foil to reduce the radial CO_2 diffusion into the confinement oil before installation into the Viton rubber sleeve. The core was then mounted in a vertically oriented Hassler-type core holder and placed inside a heating cabinet. Experimental conditions were set to 40 °C and 200 bars with a net overburden pressure of 70 bars. At these conditions, CO_2 is supercritical and has a similar density as in the pore-scale experiments. A differential pressure transducer and two absolute pressure transducers monitored pressure response at the inlet and outlet. Figure 2 shows the experimental set-up, modified from [30].

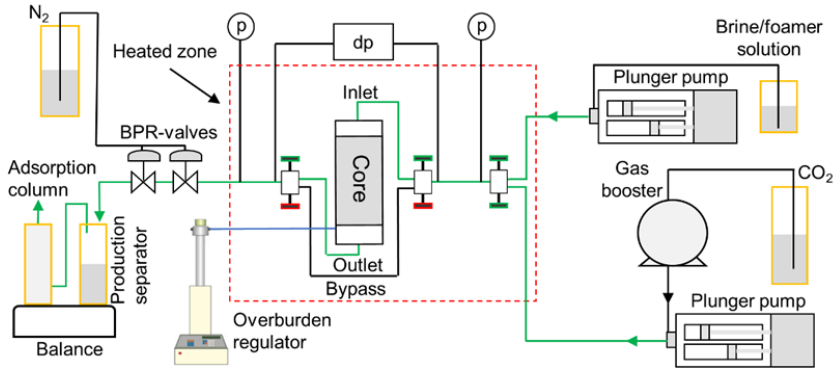

Figure 2. Experimental setup used for the core-scale foam experiments. Green lines indicate the fluid flow directions during the injection of CO_2 and the foaming solution. Pure CO_2 was pressurized by a gas booster and injected using a Quizix Q6000-10k plunger pump. Foaming solutions were injected using a Quizix Q5000-10k plunger pump. Injection was performed through a series of needle valves (marked green for open, red for closed) to the top of the core. Produced fluids were depressurized downstream through a series of backpressure regulator (BPR) valves and measured in the production separator and associated water adsorption column using a digital balance. Modified from [30].

Foam apparent viscosity is a measure of foam generation, strength and stability. An increase in apparent viscosity indicates a generation of foam and a higher value of apparent viscosity corresponds to a stronger foam. Foam apparent viscosity (μ_{app}) was quantified from the experimental superficial velocities and measured pressure drop [31] by

$$\mu_{app} = \frac{k\nabla p}{(u_l + u_g)} \quad (1)$$

where k is the absolute permeability of the porous media, ∇p is the measured pressure gradient and u_l and u_g are the superficial velocities of liquid and gas, respectively [32]. The effect of nanoparticles

on foam strength and stability was evaluated by comparing dynamic experimental apparent viscosity results using foaming solutions with and without nanoparticles.

The injection scheme for the core-scale experiments in the absence of oil was adapted from [33]. First, a minimum of three PVs of foaming solution was injected to satisfy adsorption, displace the initial brine and fully saturate the pore space. Then, CO_2 was injected from the top of the vertically mounted core at a superficial velocity of 4 ft/day for approximately six PVs. Unsteady state apparent foam viscosities were calculated as a function of time (PVs injected) using Equation (1). A minimum of two experiments were performed for each individual foaming solution. A baseline experiment, without foaming solution, was also conducted for comparison. The core was cleaned between experiments by injecting solutions of IPA before being re-saturated with brine and then foaming solution.

The core-scale procedure in the presence of oil was developed to obtain approximately 30% residual oil before evaluating foam generation and stability. First, a primary drainage with n-Decane for nearly one PV was conducted followed by a waterflood for one PV. Foaming solution was then injected for at least three PVs at a low and high rate. Finally, CO_2 was continuously injected at 4 ft/day for 10 to 14 PVs. A minimum of two experiments was performed for each individual foaming solution.

3. Results and Discussion

3.1. Pore-Scale: Foam in the Absence of Oil

Figure 3 shows pore-scale images from four experiments with different foaming solutions. Three time steps are shown which correspond to pre-foam generation (PV = 1.3), peak foam generation and post-foam generation (PV = 20.1). The images show a focused field of view with CO_2 injection from the top to the bottom for each image. The dark opaque areas are grains, the grayish-blue open areas are the pore space and the thin white films are lamellae.

The experiment with only nanoparticles present (1500 NP) generated weak foam as indicated by the continuous distribution of open flow paths and very few lamellae or bubbles (Figure 3, left column). Thus, CO_2 mobility remained high and was comparable to the baseline without any foaming agent. CO_2 injection with the three surfactant-laden foaming solutions resulted in the generation of densely distributed, finely textured foam, which significantly reduced CO_2 mobility during the peak foam generation stage (5000 SF, 5000 SF + 1500 NP and 5000 SF + 150 NP). Individual bubbles were located near the ends of pore throats and several bubbles filled individual pore bodies, suggesting snap-off as the primary foam generation mechanism. Because the pore bodies had a larger area than the pore throats, repeated snap-off occurred until the pore body was filled with bubbles, a phenomenon also described by [34]. Dynamic observations also revealed many individual lamellae spanning across pore throats. These lamellae may have formed from the leave-behind mechanism because CO_2 was injected into a surfactant saturated porous media in a drainage-like process. The rise in capillary pressure during drainage can cause lamellae generation by both leave-behind and snap-off as gas enters the pore network [35].

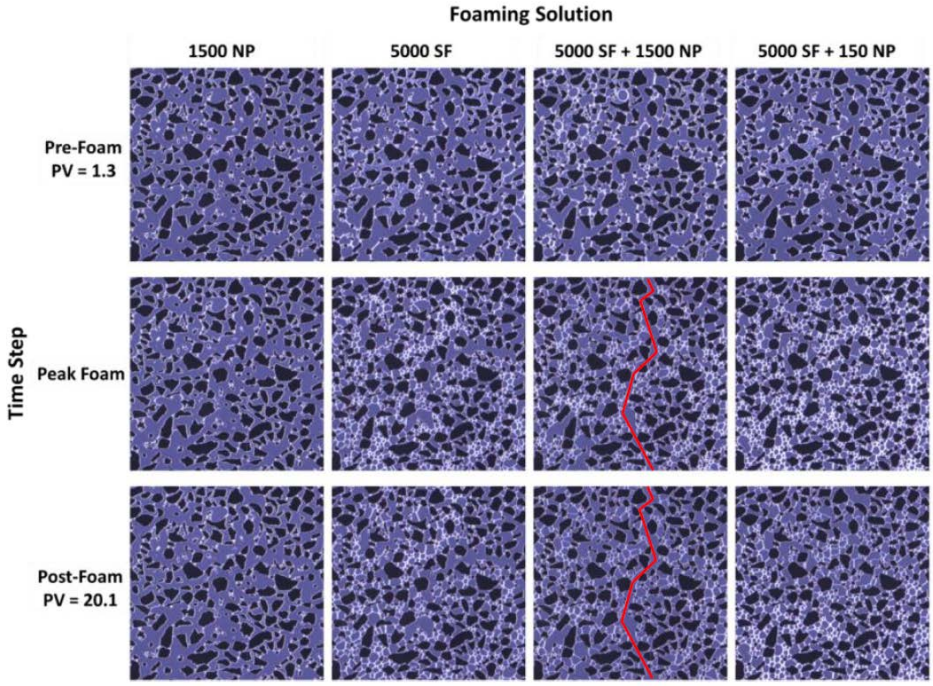

Figure 3. The pore-scale images of a focused field of view during the injection of dense phase CO_2 into a micromodel saturated with four different foaming solutions at 100 bar and 25 °C. Experiments with different foaming solutions are shown across the top: 1500 ppm nanoparticles (1500 NP), 5000 ppm surfactant (5000 SF), hybrid 5000 ppm surfactant and 1500 ppm nanoparticles (5000 SF + 1500 NP) and hybrid 5000 ppm surfactant and 150 ppm nanoparticles (5000 SF + 150 NP). Injection was from top to bottom in each image. The dark opaque areas are grains, the grayish-blue open areas are the pore space and the thin white films are lamellae. Individual image dimensions are 2190 × 2190 μm. The grain size ranged from 100 to 79,000 μm^2 and the pore throat distribution ranged from 10 to 200 μm for the entire micromodel.

Direct visual observations of the experiment with the hybrid foaming solution containing 5000 ppm surfactant and 1500 ppm nanoparticles revealed a continuous open flow path for CO_2 throughout the duration of the experiment (Figure 3, red line, 5000 SF + 1500 NP). No lamellae impeded CO_2 flow in this region and the CO_2 relative permeability was reduced by the presence of lamellae in the remainder of the pore network. Therefore, within this focused field of view, a continuous gas-foam was generated.

Figure 4 quantifies the number of bubbles versus the bubble size for the images shown in Figure 3. Bubble number and size were used as indications of foam generation and strength where a higher bubble number corresponded to a finer textured foam. All foaming solutions containing surfactant-generated small bubbles ($\leq 10^3$ μm^2) at the peak generation stage. In the post-foam generation stage, the total number of bubbles decreased and their size increased; hence, the foam texture coarsened, increasing CO_2 mobility as CO_2 was continuously injected. The hybrid foaming solutions with either 1500 ppm or 150 ppm nanoparticles showed similar behavior, indicating that foam strength and stability was not sensitive to nanoparticle concentration when used together with the selected surfactant.

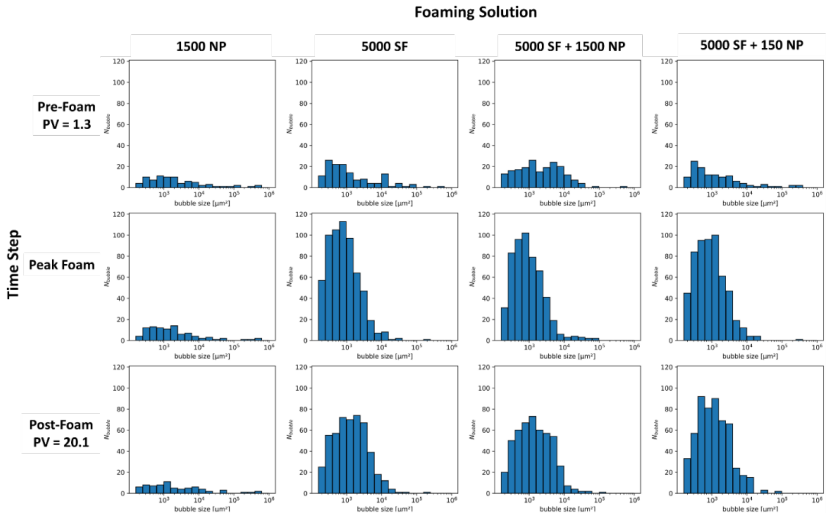

Figure 4. The number of bubbles (N_{bubble}) versus bubble size for the micromodel experiments with four different foaming solutions. Foaming solutions are shown across the top and include 1500 ppm nanoparticles (1500 NP), 5000 ppm surfactant (5000 SF), hybrid 5000 ppm surfactant and 1500 ppm nanoparticles (5000 SF + 1500 NP) and hybrid 5000 ppm surfactant and 150 ppm nanoparticles (5000 SF + 150 NP).

Pore-scale foam behavior was also analyzed by examining the total bubble number (N_i) as a function of the PV of CO_2 injected. The number of bubbles during foam generation and coalescence (N_{bubble}) were normalized to baseline ($N_{baseline}$) for the four foaming solutions. Figure 5 shows the normalized bubble number as a function of PV injected for each foaming solution for the focused field of view. Foam generation (as indicated by bubble number) increased from approximately 9 to 11 times the baseline for all foaming solutions. Peak foam generation was reached after approximately seven PVs of the CO_2 injected. After peak foam generation, the number of bubbles steadily decreased from bubble coarsening as the dominant coalescence mechanism as observed in Figure 3. The hybrid foaming solutions, containing nanoparticles and surfactant, had a limited impact on the number of bubbles and foam stability during continuous CO_2 injection.

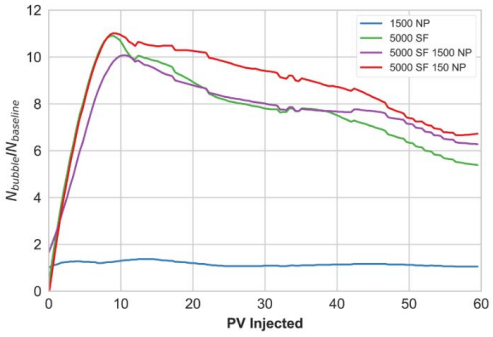

Figure 5. Development in normalized bubble number as a function of pore volume (PV) injected using four different foaming solutions for the focused field of view. The blue curve represents the foaming solution with 1500 ppm nanoparticles (1500 NP), the green curve represents the 5000 ppm surfactant solution (5000 SF), the purple curve represents the hybrid solution with 5000 ppm surfactant and 1500 ppm nanoparticles (5000 SF + 1500 NP) and the red curve represents the hybrid solution with 5000 ppm surfactant and 150 ppm nanoparticles (5000 SF + 150 NP).

The two-dimensional geometry of the micromodel likely resulted in multiple bubbles per pore because the widths of some of the pore throats were narrower than the pore throat depths. Therefore, pore-scale foam texture may not have a direct relation to foam in three-dimensional porous media. Many studies report that in situ foam usually consists of bubbles about the same size or larger than pore bodies based upon effluent analysis during laboratory experiments and the large flow resistance for bubbles smaller than pores [12,36,37]. In addition, most mechanistic foam models [38–40] assume a single bubble per pore and that discrete bubbles flow through the porous media, where foam strength is controlled by foam texture (bubble size). The latter assumptions are supported by the pore-scale observations reported here.

3.2. Pore-Scale: Foam in the Presence of Oil

Dynamic foam generation in the presence of oil was evaluated by injecting CO_2 into a micromodel saturated with a hybrid foaming solution and oil. The aim was to evaluate the impact of oil on foam generation and gain insight on the influence of oil/water emulsions during CO_2 foam processes. Figure 6 shows the pore-scale images of the unsteady-state CO_2 injection in the presence of oil with the hybrid foaming solution containing 3500 ppm surfactant and 1500 ppm nanoparticles. Three stages of the experiment are shown which correspond to before CO_2 injection, the start of CO_2 injection, and during CO_2 injection. Each image was acquired with 75 s between each time step.

Before CO_2 injection, the micromodel was initially saturated with foaming solution and oil (Figure 6a). Foaming solution appears as the continuous liquid phase, whereas oil is seen as isolated globules in interconnected pores. At the start of CO_2 injection (Figure 6b), the oil globules faded due to miscibility between CO_2 and oil. As CO_2 injection continued, the oil was displaced by CO_2 and foam readily generated in areas where oil was not present. Oil not displaced formed oil/water emulsions and occupied pores without foam present (Figure 6c). The foam (CO_2/water emulsion) had thicker lamellae compared to the oil/water emulsions likely due to interfacial tension differences at these conditions as also observed in [41]. Compared to foam (CO_2/water emulsion) alone, the combined effect of oil/water emulsions and foam further reduced CO_2 mobility. This resulted in increased "foam" strength as also observed in the core-scale experiments in the presence of oil (discussed in Section 3.4).

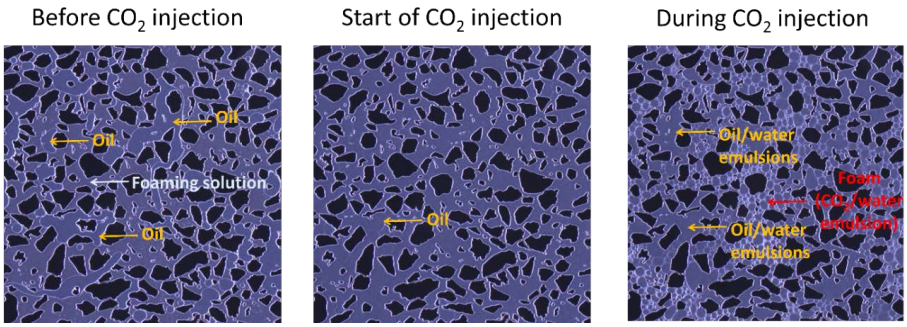

Figure 6. Pore-scale images of a focused field of view during the injection of dense phase CO_2 into a micromodel saturated with a hybrid foaming solution and oil at 100 bar and 25 °C. Three stages of the experiment are shown which correspond to: (**a**) before CO_2 injection; (**b**) the start of CO_2 injection; and (**c**) during CO_2 injection. Injection was from top to bottom in each image. The dark opaque areas are grains, the grayish-blue open areas are the pore space filled and the thin white films are the lamellae. Individual image dimensions are 2190 × 2190 µm. The grain size ranged from 100 to 79,000 µm^2 and the pore throat distribution ranged from 10 to 200 µm for the entire micromodel.

3.3. Core-Scale—Foam in the Absence of Oil

Dynamic foam generation and stability in the absence of oil was evaluated by injecting CO_2 into cores saturated with different foaming solutions. This set of experiments established conditions to investigate foam behavior during prolonged periods of CO_2 injection in a drainage-like process. Figure 7a shows the apparent viscosity versus pore volume of CO_2 injected for the CO_2 foam stability scans with foaming solutions containing only surfactant at concentrations of 3500 ppm (green curves) and 5000 ppm (blue curves). Figure 7b shows the results from the experiments using the two hybrid foaming solutions with 3500 ppm surfactant and 150 ppm nanoparticles (orange curves) and 3500 ppm surfactant and 1500 ppm nanoparticles (red curves). A baseline scan, without foaming solution, is also shown in each figure for comparison (black curves).

For all experiments, the rapid and linearly increasing apparent viscosity until 0.2 PV injected indicated that foam was generated as CO_2 invaded the core saturated with foaming solution. Apparent viscosity steadily increased, from 0.2 to 0.5 PV injected, as foam continued to generate and propagate into the core. A peak in apparent viscosity (foam strength) was achieved after approximately 0.5 PV was injected. The magnitude of the peak apparent viscosity varied from 45 to 65 cP for all experiments. The peak in apparent viscosity indicated a transition from a period of predominantly foam generation to predominantly foam coalescence. The development of a continuous CO_2 flow path not impeded by lamellae caused the foam to coalesce, likely related to a combination of bubble rupture and foam displacement. The CO_2 flow path rapidly reduced the apparent viscosity just before one PV was injected. After about six PVs were injected, the initial CO_2 viscosity was not fully recovered due to trapped bubbles in the pore space, which continued to reduce CO_2 mobility.

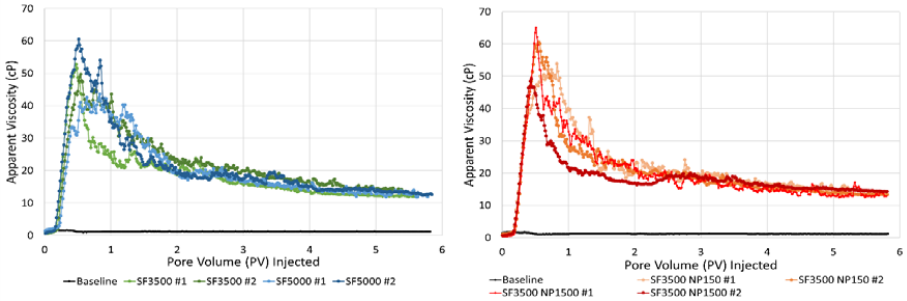

(**a**) (**b**)

Figure 7. Apparent viscosity versus pore volume of the CO_2 injected for the unsteady state CO_2 injections into cores pre-saturated with foaming solutions containing: (**a**) 3500 ppm surfactant (green curves) and 5000 ppm surfactant (blue curves); (**b**) hybrid foaming solutions containing 3500 ppm surfactant and 150 ppm nanoparticles (orange curves) and 3500 ppm surfactant and 1500 ppm nanoparticles (red curves). The black curve is the baseline with only brine.

The difference in dynamic foam generation and coalescence processes for the foaming solutions with and without nanoparticles were insignificant. Including nanoparticles in the surfactant-laden foaming solution did not result in a more stable foam and the type of foaming solutions did not clearly affect the apparent viscosity of the foam. Therefore, the surfactant contributed mostly to foam generation and the nanoparticles had only minor impacts on the foam strength and stability in these experiments. The experiments with the hybrid foaming solutions (Figure 7b) revealed similar foam behavior independent of nanoparticle concentration. Despite an order of magnitude difference in nanoparticle concentration, the measured apparent viscosities and stability of the foam were similar. Thus, the nanoparticle concentrations of 150 ppm gave similar performance as the nanoparticle concentrations of 1500 ppm when used with the selected surfactant. The next set of experiments focused on evaluating the same foaming solutions in the presence of oil, a condition known to destabilize some surfactant-based foams.

3.4. Core-Scale—Foam in the Presence of Oil

Dynamic foam generation and stability for foaming solutions with and without nanoparticles in the presence of oil was evaluated by injecting CO_2 into a core saturated with each foaming solution. The core contained a residual oil saturation of around 30% prior to being flooded with foaming solution and then CO_2. Each experiment was conducted a minimum of two times for reproducibility. Figure 8 shows the average apparent viscosity (cP) versus the pore volume of CO_2 injected for the unsteady state CO_2 foam stability scans in the presence of oil. Experiments using the foaming solution with only surfactant are shown with the blue curve and experiments with the hybrid foaming solution are shown with the red curve.

Both types of foaming solutions generated foam within the first 0.2 PV injected. However, the hybrid foaming solution generated foam more rapidly (faster increase in apparent viscosity) than the solution containing only surfactant. In addition, the hybrid foaming formulation generated a stronger (higher apparent viscosity) foam, compared to the solution containing only surfactant. The increased apparent viscosity for both types of solution indicated that each formulation generated foam with the residual oil present.

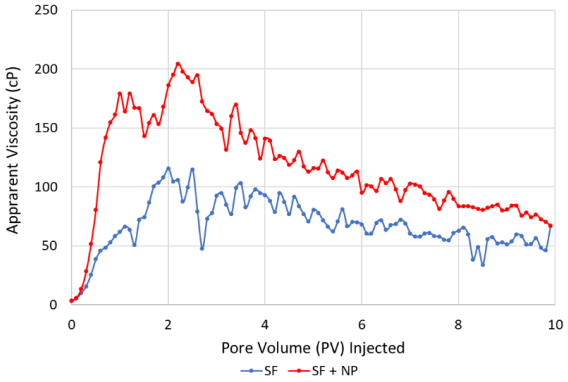

Figure 8. Apparent viscosity versus pore volume of the CO_2 injected for the unsteady state CO_2 injections in cores with residual oil (S_{or}) and pre-saturated with a hybrid foaming solution containing surfactant and nanoparticles (SF + NP, red curve) or a foaming solution containing only surfactant (SF, blue curve).

Foam-apparent viscosity values with the hybrid solution in the presence of oil (Figure 8, red curve) were nearly three times as high as the experiments without oil present (Figure 7b). In the presence of oil, the foaming solution with only surfactant (Figure 8, blue curve) had foam-apparent viscosity values about twice as high as experiments in the absence of oil (Figure 7a). This is related to the development of oil/water emulsions, which were likely stabilized by each respective foaming agent. The emulsions influenced the calculated apparent viscosities (differential pressure) and are indistinguishable from foam (CO_2/water emulsion). Nonetheless, the oil/water emulsions highlight an important facet of the CO_2 foam process, which can be beneficial to enhancing oil recovery by increasing the capillary number (increased viscous forces and lower interfacial tension) [42].

3.5. From Pore- to Core-Scale

The similarity in foam generation and coalescence during unsteady-state CO_2 injections at the pore- and core-scale is striking. Figures 5 and 7 reveal dynamic foam generation and coalescence processes with similar behavior at two different length scales. The experiments in this work were characterized by a period of rapid foam generation during drainage-like CO_2 injection and a period of foam coalescence during prolonged CO_2 injection. The decline in foam strength, at both scales, was related to the development of open CO_2 flow paths through the generated foam. This phenomenon

was a result of bubble coarsening from diffusion. The pore-scale observations unlocked real-time insights on in situ foam behavior that may help explain the observations from the core-scale experiments. Since foam was rapidly generated at both scales (due to ideal conditions for foam generation), the coalescence mechanisms during continued CO_2 injection at the pore-scale may be applied at the core-scale with some level of confidence. It is understood that foam will dry out as more CO_2 is injected and not supplemented with additional surfactant solution. Here, we showed one of the physical mechanisms responsible for such behavior.

In addition, the experiments in the presence of oil revealed the importance of stable oil/water emulsions on the CO_2 foam process. The insights from pore-scale experiments with oil shed light on the influence of oil/water and CO_2/water emulsions on CO_2 mobility reduction. Higher foam apparent viscosities were calculated for the core-scale experiments with oil present and were likely related to the development of the oil/water emulsions. Because apparent viscosity is used as an indication of foam generation and strength in laboratory experiments, care must be taken when interpreting the results from coreflood studies with the presence of stable oil/water emulsions. These emulsions can influence the calculated apparent viscosities (based on differential pressures) and may contribute to reducing CO_2 mobility.

4. Conclusions

This work presented a multi-scale investigation of hybrid nanoparticle–surfactant foam for CO_2 mobility control for CO_2 EOR and CO_2 storage. High-pressure micromodel experiments and high-pressure/high-temperature core floods evaluated a hybrid forming solution and foaming solutions with only surfactant or nanoparticles, in the presence and absence of oil. The following conclusions can be drawn:

- Direct pore-scale observations of dense phase CO_2 injection into a micromodel saturated with foaming solutions containing only surfactant or a hybrid nanoparticle–surfactant foaming solution revealed snap-off as the primary foam generation mechanism and leave-behind as a secondary foam generation mechanism.
- At the pore-scale, foam readily generated in areas where oil was not present and oil/water emulsions initially occupied pores without foam present.
- All foaming solutions containing surfactant generated foam in the presence and absence of oil, whereas foaming solution only containing nanoparticles did not. Thus, surfactant was the main foam generator and nanoparticles may be more important for foam stabilization.
- Foam strength was not sensitive to nanoparticle concentration when used together with surfactant in the tested foaming solutions.
- At the core-scale, all foaming solutions rapidly generated foam in the presence of residual oil.
- Foam apparent viscosity values with the hybrid foaming solution, in the presence of oil, were nearly three times as high as the experiments without oil. This was related to the development of oil/water emulsions, which were likely stabilized by the foaming agents.
- A link is proposed between direct pore-scale visual observations and quantitative core-scale measurements. The combined influence of stable oil/water emulsions and foam (CO_2/water emulsions) may be beneficial for increasing the capillary number by achieving higher apparent viscosity and lower interfacial tension (IFT).
- The experiments in this work were characterized by a period of rapid foam generation during drainage-like CO_2 injection and a period of foam coalescence during prolonged CO_2 injection. The decline in foam strength is related to the development of open CO_2 flow paths through the generated foam.
- Increased apparent viscosities with foam reduced CO_2 mobility at multiple length scales, which can improve volumetric sweep efficiency in field-scale CO_2 EOR and CO_2 storage processes.

Author Contributions: Conceptualization, Z.P.A., T.F., J.G., M.F.; methodology, Z.P.A., T.F., J.G., B.B., M.F.; formal analysis, Z.P.A., T.F., J.G.; investigation, T.F., B.B., A.S.; writing—original draft preparation, Z.P.A.; review and editing, T.F., J.G., B.B., M.F.; supervision, Z.P.A., J.G., M.F.; project administration, M.F.; funding

acquisition, M.F. All authors have read and agreed to the published version of the manuscript. Please turn to the CRediT taxonomy for the term explanation.

Funding: This research was funded by the Norwegian Research Council, grant numbers 268216 and 294886.

Conflicts of Interest: The authors declare no conflict of interest.

References

1. IPCC. *Climate Change 2014: Chapter 1: Mitigation of Climate Change. Contribution of Working Group III to the Fifth Assessment Report of the Intergovernmental Panel on Climate Change*; Victor, D.G., Zhou, D., Ahmed, E.H.M., Dadhich, P.K., Olivier, J.G.J., Rogner, H.-H., Sheikho, K., Yamaguchi, M., Eds.; Cambridge University Press: Cambridge, UK; New York, NY, USA, 2014.
2. Enick, R.M.; Olsen, D.K.; Ammer, J.R.; Schuller, W. *Mobility and Conformance Control for CO_2 EOR via Thickeners, Foams, and Gels—A Detailed Literature Review of 40 Years of Research*; DOE/NETL-2012/1540; USDOE, National Energy Technology Laboratory: Washington, DC, USA, 2012.
3. Hoefner, M.L.; Evans, E.M. CO_2 Foam: Results from Four Developmental Field Trials. *SPE Reserv. Eng.* **1995**, *10*, 273–281, doi:10.2118/27787-pa.
4. Martin, F.D.; Stevens, J.E.; Harpole, K.J. CO_2-Foam Field Test at the East Vacuum Grayburg/San Andres Unit. *SPE Reserv. Eng.* **1995**, *10*, 266–272, doi:10.2118/27786-pa.
5. Rossen, W.R. Foams in Enhanced Oil Recovery. In *Foams Theory, Measurements, and Applications*; Prud'homme, R.K., Khan, S.A., Eds.; Marcel Dekker, Inc.: New York, NY, USA, 1996; Volume 57, Chapter 11, pp. 414–464.
6. Falls, A.H.; Hirasaki, G.J.; Patzek, T.W.; Gauglitz, D.A.; Millerand, D.D.; Ratulowski, T. Development of a Mechanistic Foam Simulator: The Population Balance and Generation by Snap-off. *SPE Reserv. Eng.* **1988**, *3*, 884–892, doi:10.2118/14961-pa.
7. Espinosa, D.; Caldelas, F.; Johnston, K.; Bryant, S.L.; Huh, C. Nanoparticle-Stabilized Supercritical CO_2 Foams for Potential Mobility Control Applications. In Proceedings of the SPE Improved Oil Recovery Symposium, Tulsa, OK, USA, 24–28 April 2010.
8. Rognmo, A.U.; Al-Khayyat, N.; Heldal, S.; Vikingstad, I.; Eide, Ø.; Fredriksen, S.B.; Alcorn, Z.P.; Graue, A.; Bryant, S.L.; Kovscek, A.R.; ; Fernø; M. Performance of Silica Nanoparticles in CO_2-Foam for EOR and CCUS at Tough Reservoir Conditions. In Proceedings of the SPE Norway One-Day Seminar, Bergen, Norway, 2020.
9. Ogolo, N.A.; Olafuyi, O.A.; Onyekonwu, M.O. Enhanced Oil Recovery Using Nanoparticles. In Proceedings of the SPE Saudi Arabia Section Technical Symposium and Exhibition, Al-Khobar, Saudi Arabia, 2012.
10. Yu, J.; Wang, S.; Liu, N.; Lee, R. Study of Particle Structure and Hydrophobicity Effects on the Flow Behavior of Nanoparticle-Stabilized CO_2 Foam in Porous Media. In Proceedings of the SPE Improved Oil Recovery Symposium, Tulsa, OK, USA, 2014.
11. Bennetzen, M.; Mogensen, K. Novel Applications of Nanoparticles for Future Enhanced Oil Recovery. In Proceedings of the International Petroleum Technology Conference, Kuala Lumpur, Malaysia, 2014.
12. Ettinger, R.A.; Radke, C.J. Influence of Texture on Steady Foam Flow in Berea Sandstone. *SPE Reserv. Eng.* **1992**, *7*, 83–90, doi:10.2118/19688-pa.
13. Chen, M.; Yortos, Y.C.; Rossen, W.R. A Pore-Network Study of the Mechanisms of Foam Generation. In Proceedings of the SPE Annual Technical Conference and Exhibition, Houston, TX, USA, 26–29 September 2004; SPE-90939.
14. Farajzadeh, R.; Andrianov, A.; Krastev, R.; Hirasaki, G.J.; Rossen, W.R. 2012. Foam–oil interaction in porous media: Implications for foam assisted enhanced oil recovery. *Adv. Colloid Interface Sci.* **2012**, *183*, 1–13, doi:10.1016/j.cis.2012.07.002.
15. Harkins, W.D.; Feldman, A. Films: The spreading of liquids and the spreading coefficient. *J. Am. Chem. Soc.* **1922**, *44*, 2665–2685, doi:10.1021/ja01433a001.
16. Schramm, L.L.; Novosad, J.J. Micro-visualization of Foam Interactions with Crude Oil. *Colloids Surfaces* **1990**, *46*, 21–43, doi:10.1016/0166-6622(90)80046-7.
17. Marsden, S.S. *Foams in Porous Media—SUPRI TR-49*; U.S. Department of Energy Topical Report; 1986.

18. Talebian, S.H.; Masoudi, R.; Tan, I.M.; Zitha, P.L.J. Foam Assisted CO_2 EOR; Concepts, Challenges and Applications. In Proceedings of the SPE Enhanced Oil Recovery Conference held in Kuala Lumpur, Malaysia, 2–4 July 2013.
19. Farajzadeh, R. Enhanced Transport Phenomena in CO_2 Sequestration and CO_2 EOR. Ph.D. Thesis, Faculty of Civil Engineering and Geosciences, Delft University of Technology, 2009.
20. Kristiansand, T.S.; Holt, T. Properties of Flowing Foam in Porous media Containing Oil. In Proceedings of the SPE/DOE Improved Oil Recovery Symposium, Tulsa, OK, USA, 22–24 April 1992.
21. Kovscek, A.R.; Radke, C.J. Fundamentals of Foam Transport in Porous Media. In *Foams: Fundamentals and Applications in the Petroleum Industry*; American Chemical Society: Washington, DC, USA, 1994; pp. 115–163.
22. Saint-Jalmes, A. Physical chemistry in foam drainage and coarsening. *Soft Matter* **2006**, *2*, 836–849, doi:10.1039/b606780h.
23. Marchalot, J.; Lambert, J.; Cantat, I.; Tabeling, P.; Jullien, M.-C. 2D foam coarsening in a microfluidic system. *EPL (Europhysics Lett.)* **2008**, *83*, 64006, doi:10.1209/0295-5075/83/64006.
24. Falls, A.; Musters, J.; Ratulowski, J. The Apparent Viscosity of Foams in Homogeneous Bead Packs. *SPE Reserv. Eng.* **1989**, *4*, 155–164, doi:10.2118/16048-pa.
25. Farajzadeh, R.; Lotfollahi, M.; Eftekhari, A.A.; Rossen, W.R.; Hirasaki, G.J.H. Effect of Permeability on Implicit-Texture Foam Model Parameters and the Limiting Capillary Pressure. *Energy Fuels* **2015**, *29*, 3011–3018, doi:10.1021/acs.energyfuels.5b00248.
26. Buchgraber, M.; Al-Dossary, M.; Ross, C.M.; Kovscek, A.R. Creation of a dual-porosity micromodel for pore-level visualization of multiphase flow. *J. Pet. Sci. Eng.* **2012**, *86*, 27–38.
27. Hornbrook, J.W.; Castanier, L.M.; Pettit, P.A. Observation of Foam/Oil Interactions in a New, High-Resolution Micromodel. In Proceedings of the SPE Annual Technical Conference and Exhibition, Dallas, TX, USA, 6–9 October 1991; Society of Petroleum Engineers: Houston, TX, USA, 1991.
28. Benali, B. Quantitative Pore-Scale Analysis of CO_2 Foam for CCUS. Master's Thesis, University of Bergen, Bergen, Norway, December 2019. Available online: http://hdl.handle.net/1956/21300 (accessed on).
29. Bradski, G. The OpenCV Library. *Dr Dobb's J. Softw. Tools* **2000**, *25*, 120–125.
30. Føyen, T.; Alcorn, Z.P.; Fernø, M.A.; Holt, T. 2020 CO_2 Mobility Reduction Using Foam Stabilized by CO_2-and Water-Soluble Surfactants. *J. Pet. Sci. Eng.* **2020**, doi:10.1016/j.petrol.2020.107651.
31. Hirasaki, G.J.; Lawson, J.B. Mechanisms of Foam Flow in Porous Media: Apparent Viscosity in Smooth Capillaries. *SPE J.* **1985**, *25*, 176–190, doi:10.2118/12129-pa.
32. Jones, S.A.; Laskaris, G.; Vincent-Bonnieu, S.; Farajzadeh, R. Surfactant Effect on Foam: From Core Flood Experiments to Implicit-Texture Foam- Model Parameters. In Proceedings of the SPE Improved Oil Recovery Conference, Tulsa, OK, USA, 11–13 April, 2016; SPE-179637; doi:10.2118/179637-MS.
33. Føyen, T.; Brattekås, B.; Fernø, M.; Barrabino, A.; Holt, T. Increased CO_2 storage capacity using CO_2-foam. *Int. J. Greenh. Gas Control.* **2020**, *96*, 103016, doi:10.1016/j.ijggc.2020.103016.
34. Chambers, K.T.; Radke, C.J. *Interfacial Phenomena is Oil Recovery*; Morrow, N.R., Ed.; Marcel Dekker: New York, NY, USA, 1990.
35. Ranshoff, T.C.; Radke, C.J. Mechanics of Foam Generation in Glass Bead Packs. *SPE Reserv. Eng.* **1988**, *3*, 573–585, doi:10.2118/15441-pa.
36. Rossen, W.R. Theory of mobilization pressure gradient of flowing foams in porous media: III. Asymmetric lamella shapes. *J. Colloids Interface Sci.* **1990**, *136*, 38–53.
37. Falls, A.H.; Hirasaki, G.J.; Patzek, T.W.; Gauglitz, D.A.; Millerand, D.D.; Ratulowski, T. Development of a Mechanistic Foam Simulator: The Population Balance and Generation by Snap-Off. *SPE Reserv. Eng.* **1988**, *3*, 884–892, doi:10.2118/14961-pa.
38. Kovscek, A.R.; Patzek, T.W.; Radke, C.J. A Mechanistic Population Balance Model for Transient and Steady-State Foam Flow in Boise Sandstone. *Chem. Eng. Sci.* **1995**, *50*, 3783–3799, doi:10.1016/0009-2509(95)00199-f.
39. Simjoo, M.; Zitha, P.L.J. Modeling and Experimental Validation of Rheological Transition during Foam Flow in Porous Media. *Transp. Porous Media* **2020**, *131*, 315–332.
40. Ma, K.; Ren, G.; Mateen, K.; Moreland, D.; Cordelier, P. Modeling techniques for foam flow through porous media. *SPE J.* **2015**, *20*, 453–470.
41. Gauteplass, J.; Follesø, H.N.; Graue, A.; Kovscek, A.R.; Fernø, M.A. Visualization of pore-level displacement mechanisms during CO2 injection and EOR processes. In Proceedings of the EAGE IOR—17th European Symposium on Improved Oil Recovery, St. Petersburg, Russia, 16–18 April 2013.

42. Simjoo, M.; Dong, Y.; Andrianov, A.; Talanana, M.; Zitha, P.L.J. A CT Scan Study of Immiscible Foam Flow in Porous Media for EOR. In Proceedings of the SPE EOR Conference at Oil and Gas West Asia, Muscat, Oman, 16–18 April 2012.

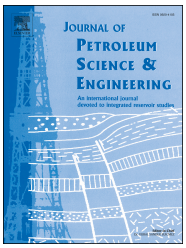

CO_2 mobility reduction using foam stabilized by CO_2- and water-soluble surfactants

T. Føyen, Z.P. Alcorn, M.A. Fernø, A. Barrabino, T. Holt

PII: S0920-4105(20)30718-X
DOI: https://doi.org/10.1016/j.petrol.2020.107651
Reference: PETROL 107651

To appear in: *Journal of Petroleum Science and Engineering*

Received Date: 12 May 2020
Revised Date: 22 June 2020
Accepted Date: 12 July 2020

Please cite this article as: Føyen, T., Alcorn, Z.P., Fernø, M.A., Barrabino, A., Holt, T., CO_2 mobility reduction using foam stabilized by CO_2- and water-soluble surfactants, *Journal of Petroleum Science and Engineering* (2020), doi: https://doi.org/10.1016/j.petrol.2020.107651.

CO_2 Mobility Reduction using Foam Stabilized by CO_2- and Water-Soluble Surfactants

Føyen, T.[1,2], Alcorn, Z.P.[1], Fernø, M.A.[1], Barrabino. A.[2], Holt, T.[2]

[1] Department of Physics and Technology University of Bergen, Norway

[2] SINTEF Industry, Norway

Abstract

Foam can reduce CO_2 mobility to improve the sweep efficiency during injection into subsurface geological formations for CO_2 storage and enhanced oil recovery. However, CO_2 foams are thermodynamically unstable, so they must be stabilized. Surfactants are often used to generate and stabilize foams in porous media and can be soluble in the aqueous phase, or in the CO_2 phase. Aqueous- and CO_2-soluble surfactants must be characterized for their ability to reduce CO_2 mobility and stabilize foam at reservoir conditions. In addition, numerical models are necessary to predict and evaluate the effect of foam for field-scale applications and require empirical data obtained from core-scale flooding experiments. This study presents a series of steady-state foam co-injections with dense phase CO_2 and either aqueous- or CO_2-soluble surfactant solutions at varying CO_2 flow velocities and CO_2 fractions. One anionic water-soluble surfactant, which is considered a benchmark foam stabilizer, and five partially CO_2-soluble non-ionic surfactants were investigated. Gamma ray attenuation was used to accurately monitor *in-situ* saturations during steady-state co-injections. The primary objective was to determine the steady-state foam characteristics of the different surfactants by evaluating the mobility reduction factor (MRF) and the limiting water saturation where foam abruptly collapses (S_w^*). All of the tested surfactants generated foam and reduced CO_2 mobility by more than three orders of magnitude. The anionic surfactant increased foam stability at lower water saturations, compared to the non-ionic surfactants, which resulted in lower residual water saturations and increased pore volume available for CO_2 storage. Core flooding results provided input into a local-equilibrium foam model. The fitted foam model reproduced the experimental results for the anionic surfactant and for three of the five non-ionic surfactants. The two latter non-ionic surfactants violated model assumptions because non-monotonic water saturation changes were observed, an effect not accurately captured by local-equilibrium foam models. However, the modelling work elucidated subtle experimental trends and demonstrated the applicability of the dataset as input into implicit-texture local-equilibrium foam models.

1 Introduction

Large-scale CO_2 storage in subsurface geologic formations is required to achieve the emission goals of limiting global warming to 1.5 °C (IPPC, 2014). The bulk of CO_2 emissions are from hydrocarbon combustion and industrial activities. Despite the need to reduce CO_2 emissions, a drastic reduction in hydrocarbon production is not expected in the next decades (IEA, 2018). Therefore, technologies must be developed to provide reliable, available and affordable energy with reduced carbon footprint. Lifecycle CO_2 emissions from hydrocarbons can be significantly reduced by utilizing captured anthropogenic CO_2 for enhanced oil recovery (EOR), where CO_2 is used as a commodity to extract remaining oil from depleted reservoirs and is simultaneously stored (Lake *et al*., 2014). CO_2 EOR can provide a cost-efficient method for establishing the necessary infrastructure for large-scale projects when co-optimized for both oil production and CO_2 storage (Ettehadtavakkol *et a*l., 2014; Lindeberg *et al*., 2017). Over 40 years of CO_2 EOR experience in the US shows mixed results due to

poor sweep efficiency caused by the high mobility of CO_2 at reservoir conditions, relative to oil and brine. Poor sweep efficiencies are also amplified by reservoir heterogeneities (Lee and Kam, 2013) because injected CO_2 may flow through the highest permeability layers and/or fractures.

CO_2 foam mobility control can mitigate poor sweep efficiencies during CO_2 EOR and CO_2 storage by reducing CO_2 mobility and stabilizing the displacement front (Enick *et al*., 2012; Vitoonkijvanich *et al*., 2015). Foam is a two-phase system consisting of gas (CO_2) dispersed in continuous thin aqueous films, called lamella, which are thermodynamically unstable and require a stabilizer (surfactants). Gas flow is impeded by lamellae which effectively decrease gas relative permeability (k_{rg}) and increase gas viscosity (μ_g). Reduction in gas permeability is caused by the trapped gas saturation (Kovscek and Radke, 1994) and increased viscosity is related to viscous shear when lamella move along pore walls (Hirasaki and Lawson, 1985) and through pore throats (Falls *et al*., 1989). k_{rg} and μ_g are tied to each other through Darcy's law and cannot be measured independently during core flooding experiments, implying that it is sufficient to modify either k_{rg} or μ_g to account for foam effects on

$$u_g = \frac{k k_{rg} \nabla p_g}{\mu_g} \tag{1}$$

CO_2 mobility. The relationship between k_{rg} and μ_g is shown in Equation 1:

where u_g is the gas flow velocity, k is the absolute permeability and ∇p_g is the gaseous phase pressure gradient. The flow of the continuous aqueous phase is not directly affected by foam (Bernard and Jacobs, 1965; Eftekhari and Farajzadeh, 2017), therefore the water relative permeability (k_{rw}) and viscosity (μ_w) remain unchanged.

During steady-state co-injection of gas and water into a porous medium (without foam), the water saturation will adjust so that the porous medium transports the two phases at the relative rates required by the injected fluid fractions. An increase in the gas fractional flow is accommodated by a simultaneous change of both gas and water mobilities through a reduction of the water saturation and an increase in capillary pressure (Valavanides, 2018; Worthen *et al*., 2018).

However, an increase in gas fractional flow will not necessarily cause a reduction of water saturation during steady-state foam flow. Two distinct quality regimes of foam can exist in porous media; low-quality and high-quality regimes, separated by a transitional gas fraction f^*. When foam is in the low-quality regime, the pressure gradient adjusts to the level that the foam films can withstand, termed the limiting pressure gradient. Falls *et al.* (1989) assumed that there is one maximum pressure drop that any film in the porous medium can withstand. This implies that the pressure gradient should be independent of the flow rate and that the gas relative permeability increases linearly with the flow rate, exhibiting a shear thinning behaviour as elucidated by Rossen and Wang (1999).

Foam enters the high-quality regime when the gas fraction is increased above the transitional gas fraction, f^* and the water saturation approaches a saturation value where the lamellae are no longer stable. This occurs at a limiting capillary pressure (P_c^*) that corresponds to the maximum disjoining pressure of the foam film and is associated with a limiting water saturation for foam stability, defined as the foam breakdown saturation, S_w^* (Falls *et al*., 1989; Farajzadeh *et al*., 2015). For a foam close to its maximum disjoining pressure, a minute increase in the capillary pressure will bring a large number of films to capillary-driven rupture, so the gas fractional flow increases with virtually no saturation

changes. Deviations from the above descriptions are expected in porous media because there will be a distribution of grain geometry and pore sizes influencing foam flow. The water saturation may vary over a limited range in the high-quality regime. Furthermore, variations in the maximum pressure gradient can be expected in the low-quality regime.

Alpha olefin sulfonates (AOS) are a class of anionic surfactants that are well known and widely used to generate foam with excellent foaming properties and are considered benchmark surfactants (Farajzadeh *et al*., 2008; Farajzadeh *et al*., 2011; Jones *et al*., 2016). This includes the large scale field test in the Snorre reservoir for hydrocarbon gas foam EOR (Blaker *et al*., 2002) and CO_2 foams field tests with either AOS or mixtures with AOS and other surfactants (Borling, 1994; Chou *et al*., 1992; Henry *et al*., 1996; Hoefner and Evans, 1995; Jonas *et al*., 1990; Moffitt *et al*., 2015). Anionic surfactants are only soluble in the aqueous phase, which can segregate from less dense CO_2 some distance from the well, potentially limiting the distribution of foam in the formation during field-scale operations (Vassenden *et al*., 1999).

Segregation of the injected surfactant can be mitigated by using surfactants soluble and transported by both the aqueous and gaseous phase. Several studies have tested various types of surfactant that partition between CO_2 and water in porous media, including: linear and branched alkylphenol ethoxylates (McLendon *et al*., 2012; Xing *et al*., 2010), branched alkyl ethoxylates (Xing *et al*., 2012), ethoxylated cocoamines (Chen *et al*., 2012), triblock copolymer surfactants (Adkins *et al*., 2010) and dioctyl sodium sulfosuccinates(Le *et al*., 2008). These studies report foam rheology measurements performed in bulk foam (Xing *et al*., 2010), or by flow experiments in porous media, cylindrical cores (Le *et al*., 2008; McLendon *et al*., 2012; Xing *et al*., 2012) and sand packs (Adkins *et al*., 2010; Chen e*t al*., 2012), respectively . However, the foam experiments are challenging to generalise, compare and use for parameterization in foam models due to the injection schemes used. Additionally, the core and sand pack experiments lack saturation measurements, which are important for constructing relative permeability curves and determining key foam properties such as the foam breakdown saturation, S_w^*.

This work evaluated five commercially available non-ionic, partially CO_2-soluble surfactants (Brij L23, Igepal CO720, Tergitol NP10, Tergitol TMN10, Tergitol 15-S-9) as foam stabilizers. The primary objective was to determine the steady-state foam characteristics of the different surfactants by evaluating the mobility reduction factor (MRF) and the limiting water saturation where foam abruptly collapses (S_w^*). Partitioning between CO_2 and brine, cloud point temperature has previously been reported by Barrabino *et al*. (2020) and foam generation and decay during unsteady-state injection by Føyen *et al*. (2020). Foam measurements were obtained by co-injecting CO_2 and surfactant solutions through a sandstone core at various CO_2 flow velocities and CO_2 fractions. Gamma ray attenuation was used to accurately monitor *in-situ* saturations during steady-state co-injections. The surfactants were evaluated by considering the water saturation where foam will abruptly collapse (S_w^*) and the mobility reduction factor (MRF), describes the reduction in gas mobility by foam (see Equation 8 for details). The five partially CO_2-soluble, non-ionic surfactants were compared with the well-known and widely used water-soluble anionic AOS surfactant. The experimental observations were fitted to an implicit-texture local-equilibrium foam model developed by Vassenden and Holt (2000). The model curves aid the analyses by simplifying quantification, revealing additional observations and demonstrating the use of the dataset as input to implicit-texture local-equilibrium foam models.

2 Methods and materials

2.1 Rock material

Steady-state co-injections with CO_2 and brine or surfactant solution were performed in a single cylindrical, outcrop Bentheimer sandstone core (**Table 1**) to eliminate the impact of changing core properties. Porosity was determined by $NaNO_3$ flooding. The liquid absolute permeability was calculated using Darcy's law using four constant volumetric injection rates. The core was cleaned and re-saturated with surfactant solution before each separate foam injection experiment. The permeability of the core was monitored throughout the experimental campaign and negligible variations between measurements were observed.

Table 1. Core properties	
Length (cm)	19.9 ± 0.01
Diameter (cm)	3.71 ± 0.01
Pore Volume (ml)	47.8 ± 0.5
Porosity	0.22± 0.01
Permeability (Darcy)	2.83 ±0 .15

2.2 Fluid preparation

Synthetic seawater doped with caesium (Cs-dSSW, see Table 2) was used as the aqueous phase for all co-injections and was mixed with the appropriate surfactant (Table 3) to produce surfactant solutions. Addition of Caesium improves signal-to-noise ratio during *in-situ* saturation monitoring due to increased gamma attenuation that increases the signal contrast between the aqueous phase and CO_2 at experimental conditions. All aqueous phases were filtered through a 0.45 µm cellulose acetate filter before injection through the core sample. The foaming ability of five commercially available non-ionic surfactants (Sigma-Aldrich) with different CO_2/brine partitioning coefficients (kp) were compared to a $C_{14\text{-}16}$ AOS (Stepan), all listed in Table 3. A constant surfactant concentration (0.5 wt. %) was used for all surfactant solutions. The surfactant solutions were flushed with argon to remove dissolved oxygen and stored under an argon atmosphere. CO_2 of 99.9999% purity was used during the co-injection experiments. Measurements of cloud point temperature and partitioning coefficient for the surfactants used in this study is previously reported by Barrabino et al. (2020).

Table 2: Composition of caesium doped synthetic seawater. All salts were EMSURE salts (Merck Millipore) supplied by VWR.

Component	**Concentration [wt. %]**
Deionized water	94.52
CsCl	2.63
NaCl	1.37
$CaCl_2 \bullet 2H_2O$	0.19
$MgCl_2 \bullet 6H_2O$	0.90
KCl	0.07
Na_2SO_4	0.33

Table 3: Surfactants used as the foaming agents. Partitioning coefficients were measured at 40°C and 200 bar (Barrabino *et al.*, 2020).

Commercial Name	**Type**	**kp [wt. %/wt. %]**
Anionic, water-soluble		
BIO-TERGE® AS-40 (AOS)	$C_{14\text{-}16}$ sodium olefin sulfonate	0
Non-ionic, partially CO_2-soluble		
Tergitol 15-S-9	Branched alkyl ethoxylate	1.45± 0.14
Tergitol TMN 10	Branched alkyl ethoxylate	0.87± 0.01
Tergitol NP 10	Branched alkylphenol ethoxylate	0.10± 0.00
Igepal CO 720	Linear nonylphenol ethoxylate	0.22± 0.00
Brij L23	Lauryl ethoxylate.	0.02 ± 0.00

2.3 Core preparation

The Bentheimer core plug was wrapped in nickel foil (0.025 mm) to reduce exposure between CO_2 and the Viton rubber sleeve in the carbon fibre bi-axial core holder (**Figure 1**). Methanol was injected to increase pore pressure and to fill the pore space with liquid. The pore pressure was always 200 bar and the confinement pressure was 270 bar during the co-injections. The temperature was 40°C when non-ionic surfactant solutions (CO_2-soluble surfactants) were used and 80°C when AOS was used.

A rigorous core cleaning process was performed after each experiment to ensure that surfactant residue was removed. The cleaning started with injection of 2-propanol/water azeotrope followed by methanol, toluene and n-hexane (approximate 10 PV for each). The cleaning process summarised below also ensured 100% fluid saturation of the CO_2 saturated core ($I_{Sw=0}$) and the aqueous phase saturated core ($I_{Sw=1}$) necessary to perform the reference scans needed for *in-situ* saturation monitoring.

1. Injection of 2-propanol/water azeotrope (87.7 wt. % 2-propanol)
2. Injection of methanol
3. Injection of toluene
4. Injection of n-hexane
5. Injection of CO_2
6. Record CO_2 (I_{Sw}=0) reference scans
7. Injection of synthetic seawater
8. Injection of surfactant solution
9. Record brine (I_{Sw}=1) reference scans (core ready for next co-injection experiment)

Absorption measurements were also performed when the core was saturated with surfactant solution by measurement of surfactant concentrations in the produced effluents. The surfactant analyses during Step 8 (by HPLC) showed no traces of the surfactant used in the previous experiment, indicating sufficient cleaning of the core.

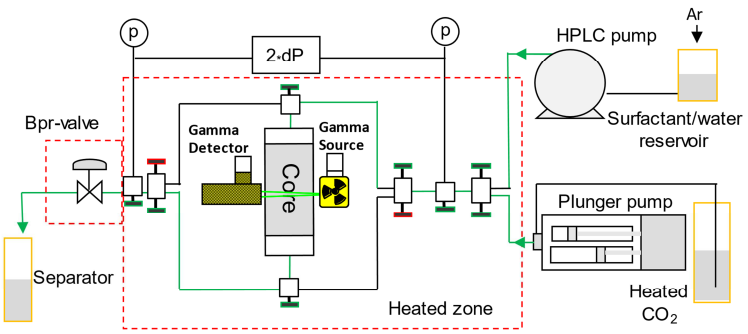

Fig. 1. Experimental setup for co-injections with CO_2 and surfactant solution. CO_2 from the plunger pump (Quizix Q5210) was co-injected with surfactant solution from the HPLC pump (Beckman Model 100A) through the high-pressure steel tubes (1/8 in inner diameter, marked green) and Autoclave needle valves (green for open, red for closed) to the top of the vertically positioned core sample. Produced fluids at the bottom were depressurized through the back-pressure regulator valve and collected in the separator. A gamma source and detector mounted on a motorized unit (not shown) enabled ISSM. The HPLC pump was used between co-injections to inject various solutions (brine, surfactant solutions and cleaning fluids).

2.4 Experimental procedure

Steady-state co-injections of CO_2 and surfactant solution for six different surfactants evaluated the foaming properties of each surfactant. In addition, CO_2/water relative permeability curves in the presence and absence of foam were obtained. The experimental observations provided input parameters for the foam model. Before every co-injection several pore volumes (>6) of surfactant solution were first injected to satisfy surfactant adsorption. Effluent concentrations were measured to ensure that the core was fully saturated with surfactant solution prior to starting the co-injection. The volume of surfactant solution required to satisfy adsorption varied for the different surfactants but was less than 2.0 PV (for Tergitol 15-S-9 that had the highest adsorption, 1.1 mg surfactant per gram of rock).

Foam was injected from the top of the core using four different CO_2 Darcy velocities (u_g = 0.5, 0.8, 1.05 and 1.3 m/day) at four different gas fractions (0.6, 0.8, 0.9 and 0.95), as indicated in the injection scheme (**Figure 2**). The CO_2 velocities and gas fractions could vary slightly for the different experiments. For the experiments with Tergitol 15-S-9 only three gas fractions were used for the flow velocity 1.05 m/s. The flow rates were changed when steady-state pressures were reached. The fluid saturations were measured at steady-state using *in-situ* saturation monitoring (Chapter 2.5). The differential pressure across the core was logged versus time, using two Fuji differential pressure transmitters (range 5 and 20 bar) to calculate the foam apparent viscosity (μ_{app}), water relative permeability (k_{rw},) and CO_2 relative permeabilities with and without the presence of foam (k_{rg}^{f} and k_{rg}) using equations 3 and 4, respectively. Experimental input parameters such as core temperature, flow velocities and back- and confinement-pressures were logged versus time during co-injections. Experimental output parameters such as inlet-, outlet- and differential pressures were continuously monitored and are presented and discussed below. Data is available from an open-source online data repository hosted by Mendeley Data (Føyen and Holt, 2020).

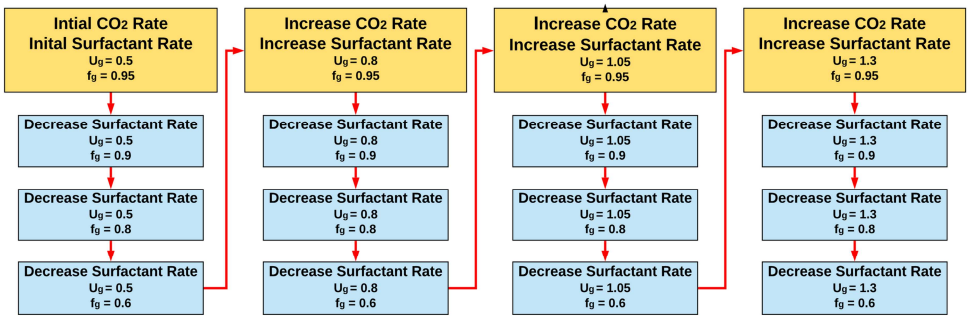

Fig. 2. The injection schemes used during the steady-state co-injections with CO_2 and surfactant solution. The unit for CO_2 Darcy velocities (u_g) is m/day.

In addition to the foam co-injections, a steady-state co-injection with CO_2 and brine was performed at five different gas fractions (0.22, 0.42, 0.60, 0.80 and 0.90) with a Darcy velocity of 2.9 m/day to obtain reference water/CO_2 relative permeability data without the presence of foam. The experimental results were fitted to the LET relative permeability curves as shown in Figure 5.

2.5 *In-situ* Saturation Monitoring

Aqueous (surfactant solutions and brine) and (CO_2) phase saturations were measured using gamma ray attenuation saturation monitoring. The gamma ray source and detector was located on one side of the core and the detector was directly opposite (Figure 1). The source and detector pair were attached to the same motorized unit so that they could move up and down along the core for

measurements at multiple predetermined positions distributed at a 5mm distance across the core length. At each scan-location, acquisition was performed by emitting the γ-ray at a constant intensity through the core towards the detector. The intensity (counts) was recorded over a predetermined acquisition time (120 s) before the source/detector was moved to the next position. The recorded intensity (I_{Sw}) was used to calculate the phase saturation at each position using Equation 2. The calculation required two reference scans; one for each phase, obtained when the core was 100% saturated with the aqueous phase ($I_{Sw=1}$) and the gaseous phase CO_2 ($I_{Sw=0}$). The reported S_w is the average value for the whole core, excluding the first and last 1cm of the core affected by interference from the end pieces of the core holder.

$$S_w = \frac{\ln(\frac{I_{Sw}}{I_{Sw=0}})}{\ln(\frac{I_{Sw=1}}{I_{Sw=0}})} \quad (2)$$

Reference scans (minimum one for each phase) were performed prior to co-injection to account for any differences in rock material, core location and aqueous solution composition for gamma attenuation, as recommended by Reed and Cense (2018). The saturation profiles had small capillary end effects and the complete profiles can be found in the online dataset (Føyen and Holt, 2020).

2.6 Flow equations

2.6.1 Relative permeability of water and CO_2 without foam

Co-injection of CO_2 and brine was used to calculate the CO_2/water relative permeability without foam. The relative permeability for water (k_{rw}) and gas (k_{rg}) was calculated with the Darcy equation:

$$k_{rw} = \frac{u_w * \mu_w}{\mathrm{k} * \nabla p_w} \quad (4) \qquad \text{and} \qquad k_{rg} = \frac{u_g * \mu_g}{\mathrm{k} * \nabla p_g} \quad (3)$$

where μ_w and μ_g, u_w and u_g, $\nabla p_w$and ∇p_g are the viscosities, Darcy velocities and pressure gradients of the water and gas phases, respectively. Zero capillary pressure is assumed, *i.e.* $\nabla p_w = \nabla p_g$.

Experimentally obtained water and gas relative permeability (k_{rw} and k_{rg}) data were fitted to permeability curves as a function of water saturation using the empirical LET model (Lomeland *et al.*,

$$k_{rg} = k_{rg}^{x} * \frac{(1 - S_{wn})^{Lg}}{(1 - S_{wn})^{Lg} + E_g * (S_{wn})^{Tg}} \quad (4)$$

$$k_{rw} = k_{rw}^{0} * \frac{(S_{wn})^{Lw}}{(S_{wn})^{Lw} + E_w * (1 - S_{wn})^{Tw}} \quad (6)$$

2005):

where k_{rg}^{x} and k_{rw}^{0} are end points relative permeabilities and Lg, Eg, T_g, Lw, E_w, and T_w are empirical fitting parameters.

$$S_{wn} = \frac{S_w - S_{wi}}{1 - S_{wi} - S_{gr}} \quad (7)$$

The normalized water saturation S_{wn} is defined as

where $\boldsymbol{S_{wi}}$ is the irreducible water saturation and $\boldsymbol{S_{gr}}$ is the residual gas saturation.

2.6.2 Relative permeability of water and CO_2 with foam

Water $\left(k_{rw}^{f}\right)$ and gas (k_{rg}^{f}) relative permeabilities in the presence of foam were calculated by using the same procedure as above during co-injections with CO_2 and surfactant solutions. It is well established that foam reduces gas relative permeability and can be modelled by modifying the no-foam gas relative permeability (k_{rg}) by the factor FM, inversely proportional to the mobility reduction factor (MRF). The gas relative permeability in the presence of foam (k_{rg}^{f}) was calculated

$$k_{rg}^{f}(S_w) = k_{rg}(S_w) * FM \quad (8)$$

using Equation 8.

Numerous foam models that implement and extrapolate core-scale laboratory data to evaluate field-scale foam behaviour are described in the literature (Ma *et al.*, 2015). Depending on the selected foam model, FM can capture the influence of several parameters such as surfactant concentration, salt concentration, permeability, flow velocity, water saturation, oil saturation and composition. The experimental observations reported here were fitted to an implicit-texture local-equilibrium foam model derived by Vassenden and Holt (2000), labelled the V-H model. The V-H model was originally derived from experimental AOS co-injection data with hydrocarbon and nitrogen gas.

$$FM = e^{(S_w^* - S_w) * s_1} + \left(\frac{u_g}{u_{g0}}\right) * FM_0 * e^{(S_w^* - S_w) * s_2}, when\ S_w > S_w^*$$
$$FM = 1;\ S_w < S_w^* \quad (9)$$

For the V-H foam model, FM is defined as

Where S_w is the water saturation, S_w^* is the foam breakdown saturation, FM_0 is the largest mobility reduction at the reference gas Darcy flow velocity u_{g0}, u_g is the Darcy flow velocity, s_1 and s_2 are fitting parameters controlling the mobility reduction in the high and low quality regimes, respectively.

The V-H model input parameters used to calculate the gas relative permeability with foam are illustrated in Figure 3. Below the foam breakdown saturation (S_w^*) foam will not exist (red-area) and the gas relative permeability equals the no-foam gas relative permeability (k_{rg}), shown as the red solid line. In the high-quality foam regime (yellow-area), the V-H model gives an exponential reduction in foam gas relative permeability (k_{rg}^{f}) where the slope is controlled by the parameter s_1 (blacked dashed lines). A round transition region truncates the high-quality regime into the low-

quality regime (green-area) where the gas mobility is a factor (FM_0) lower than the gas mobility without foam at a the reference gas velocity (u_{g0}) . The parameter s_2 allows the mobility reduction to vary in the low-quality regime and the term $^{u_g}/_{u_{g0}}$ accounts for the shear-thinning behaviour. The water permeability with foam is assumed to be equal to the water permeability without foam.

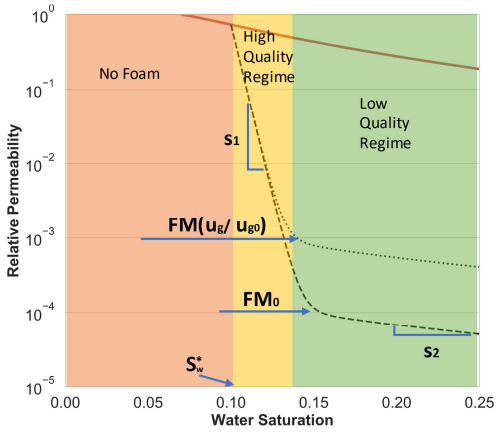

Fig. 3. Illustration of how the different V-H foam model parameters affect the gas relative permeability in the different foam regimes. Gas relative permeability without foam (red line) and with foam (black lines) using the V-H model at a reference gas velocity (dashed line) and a gas velocity $u_g > u_{g0}$ (dotted line). Values are generic but are representative for typical foam systems. Figure modified from Vassenden and Holt (2000) .

2.6.3 Fractional flow and apparent viscosity

Foam strength during co-injections are typically reported as apparent viscosity as a function of gas fraction (Alcorn *et al*., 2019) and can be obtained from the relative permeability measurements using the Buckley-Leverett equation for the fractional flow curves of water and gas, f_w and f_g. To account for the foam effect, a substitution was made using the foam gas relative permeability (k_{rg}^f). Solving

$$f_g = 1 - \frac{1}{1 + \frac{k_{rg}^f * \mu_w}{\mu_g * k_{rw}}} \tag{10}$$

for gas fractional flow gives:

$$\mu_{app} = f_g * \frac{\mu_g}{k_{rg}^f} \tag{11}$$

Thus, the apparent foam viscosity can be calculated as:

2.6.4 Parameterization and coefficient of determination

A simple iterative approach was used to obtain the best fit between experimental data for the LET relative permeability model and the V-H foam model by looping through a list containing combinations of the parameters. The reported parameters were selected based on calculated errors between model curves and observed data. The conventional coefficient of determination, R^2, was used for water and CO_2 relative permeability (without foam, LET model) and was calculated by:

$$R^2 = 1 - \frac{SS_{res}}{SS_{tot}} \quad (12)$$

where, SS_{tot} is the total sum of squares, given by the mean of the observed data ($\bar{y}$) and the

$$SS_{tot} = \sum(y_i - \bar{y})^2 \quad (13)$$

experimental data points (y_i):

$$SS_{res} = \sum(y_i - f_i)^2 \quad (14)$$

and, SS_{res} is the sum of squares of residuals, given by the modelled values (f_i):

For the foam model, the parameterization giving the lowest SS_{res} was used because SS_{tot} is dependent upon mean values and can become unsuitably small resulting in negative R^2 values on log scales.

3 Results and Discussion

This section presents relative permeability curves for CO_2/water in the presence and absence of foam and the local-equilibrium foam model fitting to the experimental data. Data is available from an open-source online data repository hosted by Mendeley Data (Føyen and Holt, 2020).

3.1 Reference CO_2 and water relative permeability

Steady-state CO_2/water relative permeability curves provided a reference case for the CO_2 relative permeability in the presence of foam (k_{rg}^f). The V-H model foam-gas relative permeability curves were fitted to the experimental data (**Figure 4**) using Equation 3 and 4 with LET parameters listed in **Table 4**. The low capillary number (low pressure gradient) during the co-injection without foam limited the water saturation range of the CO_2/water relative permeability data ($S_w = 0.45$ to 0.85) and did not overlap the saturation range ($S_w = 0.10$ to 0.35) observed with foam present because of the higher capillary number. The parameter L_w controls the shape of the water relative permeability (k_{rw}) curve at lower saturations and L_w was varied between 2.0 and 2.6 to achieve a model fit for CO_2 injections with foam below $S_w = 0.4$. The gas relative permeabilities without foam (k_{rg}) and water (k_{rw}) matched with L_w = 2.2 and were used as a reference for subsequent co-injections with foam. Other empirical parameters listed in **Table 4** remained constant for all matches. For CO_2 storage decreased water saturation is beneficial, as it increases the volume occupied by CO_2.

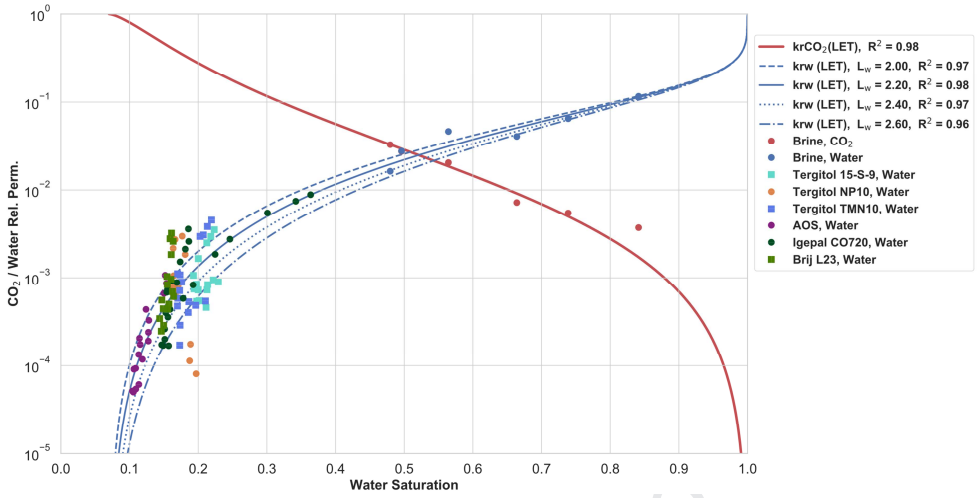

Fig. 4. Relative permeability curves (lines) for water (blue) and CO_2 (red) when fitted to the experimental data points (solid points) with and without the presence of foam. Each surfactant is identified with a unique coloured symbol. The water relative permeability parameter L_w was varied between 2.0 and 2.6 to produce a range of curves (in blue) fit to experimental data points, where the determination (R^2) was 0.98 for CO_2 (without foam) and ranged between 0.93 – 0.98 for water (with and without foam). Intermediate water saturation data points (S_w = 0.25 to 0.35) for surfactant Igepal CO720 were achieved with decreasing surfactant concentrations (< 0.5 wt%) in a separate CO_2-injection to expand the experimental saturation range between S_w = 0.85 to 0.10 in the water relative permeability curve.

Table 4: LET parameters for relative permeability curves CO_2/water without foam in Figure 4

S_{wi}	S_{grw}	L_w	E_w	T_w	L_g	E_g	T_g
0.07	0.00	2.20	10.34	0.39	1.73	36	1.45

3.2 Foam Model Fitting to Experimental Observations

Three physical features of foam are important to be observed in the experimental dataset and should be captured by the foam model.

i) The high- and low-quality regimes, separated by the transition gas fraction, where the mobility reduction (apparent viscosity) of foam is largest.

ii) The shear thinning behaviour in the low-quality regime, due to the limiting pressure gradient (Rossen and Wang, 1999).

iii) The abrupt reduction in foam strength in the high-quality regime, due to high capillary pressure (Falls *et al*., 1989).

All features were well captured using the V-H foam model for the steady-state co-injection with CO_2 and the anionic AOS surfactant (**Figure 5**) using a water relative permeability curve with L_w = 2.2. The data points were obtained within the low- and the high-quality regime and the foam breakdown saturation (S_w^*) was captured together with the largest mobility reduction by foam (FM_0.). The four flow velocities show shear-thinning behaviour in the low-quality regime, captured by the term u_g/u_{g0} in the V-H model (Equation 9).

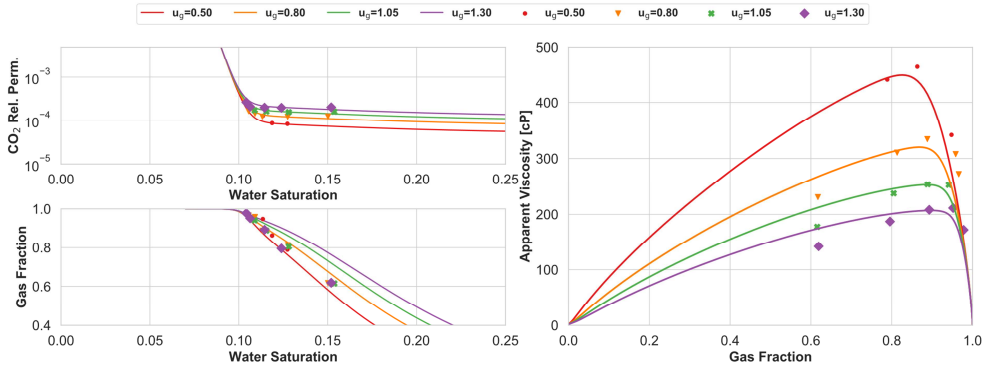

Fig. 5. Steady-state co-injection with CO_2 and the anionic AOS surfactant. The V-H model (solid lines) was matched to experimental data (symbols). Top-left: CO_2 relative permeability versus water saturation. Bottom-left: Gas fractional flow versus water saturation. Right: Apparent viscosity versus gas fractional flow. The experimental data points at different gas flow velocities are shown using unique shapes and colours. Modelled curves are shown using lines and gas flow velocities use the same colour-scheme as the experimental data points.

The steady-state co-injection with CO_2 and the non-ionic Brij L23 surfactant generated foam (**Figure 6**) which reduced CO_2 mobility by a factor of 1800 (**Figure 11**). The low- and high- quality regimes were clearly observed during the experiment. The transition gas fraction revealed the largest mobility reduction of the foam with an abrupt reduction in foam strength beyond this point, in the high-quality regime. However, the shear-thinning behaviour in the low-quality regime was only evident at the lowest gas fractions (0.6 and 0.8). Additionally, the measured water saturations were within in a narrow range from 0.14 to 0.17 for the Brij L23 foam injection (Figure 6), compared to 0.10 to 0.15 for the AOS foam injection (Figure 5). The limited distribution in water saturations and lack of data points showing shear-thinning behaviour, indicate that most data points were obtained in the high-quality regime, or at the transition to the high-quality regime.

In contrast to steady-state co-injections without foam, increased gas flow velocities will not necessarily result in higher gas saturation for foam in the high-quality regime. This is because in the high-quality regime, bubble coalescence rather than changes in saturation facilitate the increased flow velocity (Vassenden and Holt, 2000). Figure 6 (left plots) shows this behaviour, as the water saturation was nearly unchanged across the range of gas fractions and velocities. The sensitivity between water saturation and foam gas relative permeability in the high-quality regime caused challenges when using of Buckley Leverett equation to capture the gas fractional flow versus water saturation.

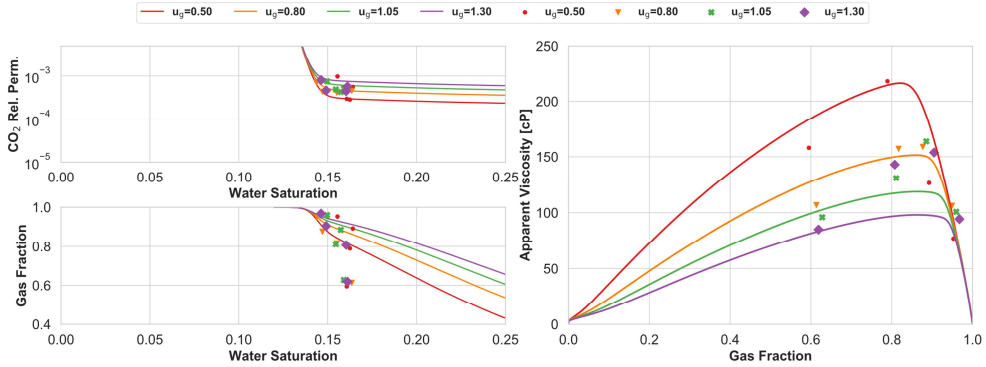

Fig. 6. Steady-state co-injection with CO_2 and the non-ionic Brij L23 surfactant. The V-H model (solid lines) was matched to experimental data (symbols). Top-left: CO_2 relative permeability versus water saturation. Bottom-left: Gas fractional flow versus water saturation. Right: Apparent viscosity versus gas fractional flow. The experimental data points at different gas flow velocities are shown using unique shapes and colours. Modelled curves are shown using lines; gas flow velocities are shown using the same colour-scheme as the experimental data points.

Figure 7 and **Figure 8** show the results from the steady-state co-injections with Igepal CO720 (Figure 7) and Tergitol NP10 (Figure 8). Both experiments revealed the three physical features important to be observed. This included the presence of a low- and high-quality foam regime, shear-thinning behaviour in the low-quality regime and an abrupt reduction in foam strength (apparent viscosity) in the high-quality regime. However, initially, the V-H model could not match the experimentally observed transition between the low- and the high-quality regimes in the apparent viscosity curves. This was due to an inadequate match between water saturation and gas fractional flow at high gas fractions. Therefore, L_w was increased to 2.4 to better reflect the water relative permeability curve for these surfactants and improved the gas fractional flow curves (see Figure 4).

During both co-injections (Igepal CO720 and Tergitol NP10), foam gas relative permeability data points were obtained within the low- and the high-quality regime. When the necessary adjustments in the water relative permeability curve were performed, the location of the transition between the low- and high-quality regime, and the foam breakdown saturation (S_w^*) were captured. The four flow velocities, in both co-injections, showed a shear-thinning behaviour in the low-quality regime, captured by the term $^{u_g}/_{u_{g0}}$ in the V-H model (Equation 9).

Despite the improved match with small changes in water relative permeability in the presence of foam, the assumption that foam does not affect water relative permeability is considered valid. Relatively, the difference between the water relative permeability curves using $L_w = 2.2$ and 2.4 (see Figure 4) are small when compared with the difference between foam gas relative permeability curves (k_{rg}^f) and (no-foam) gas relative permeability curves (k_{rg}). However, the sensitivity demonstrates the importance of accurate fluid saturation measurements and reference relative permeability curves when determining foam parameters.

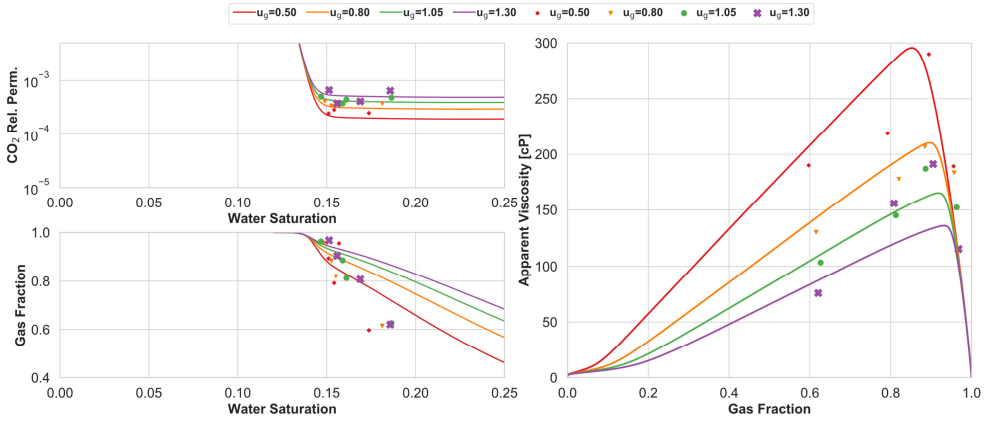

Fig. 7. Steady-state co-injection with CO_2 and the non-ionic Igepal CO720 surfactant (non-ionic). The V-H model (solid lines) was matched to experimental data (symbols) using an adjusted water relative permeability curve. Top-left: CO_2 relative permeability versus water saturation. Bottom-left: Gas fractional flow versus water saturation. Right: Apparent viscosity versus gas fractional flow. The experimental data points at different gas flow velocities are shown using unique

shapes and colours. Modelled curves are shown using lines; gas flow velocities are shown using the same colour-scheme as the experimental data points.

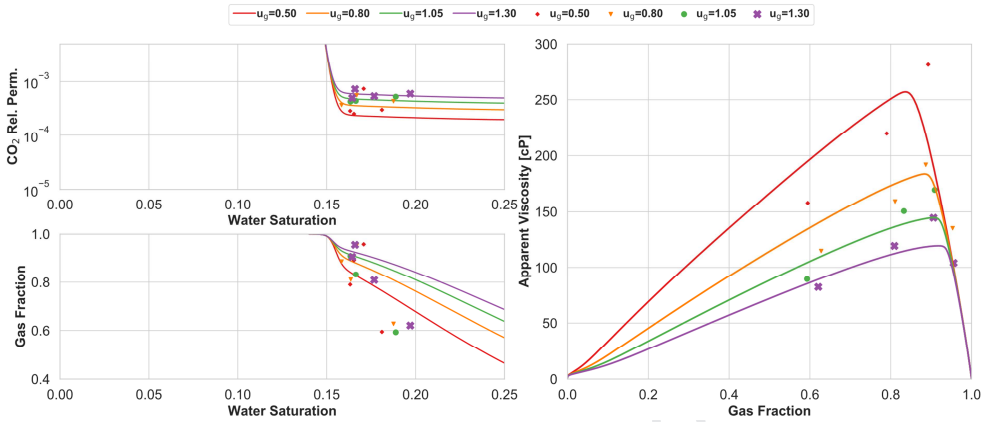

Fig. 8. Steady-state co-injection with CO_2 and the non-ionic Tergitol NP10 surfactant (non-ionic). The V-H model (solid lines) was matched with experimental data (symbols), using an adjusted water relative permeability curve. Top-left: CO_2 relative permeability versus water saturation. Bottom-left: Gas fractional flow versus water saturation. Right: Apparent viscosity versus gas fractional flow. The experimental data points at different gas flow velocities visualized using unique shapes and colours. Modelled curves are showed using lines; gas flow velocities are visualized using the same colour-scheme as the experimental data points.

3.3 Non-monotonic changes in water saturation

The water saturation during steady-state co-injection is expected to decrease monotonically (or remain constant) when the gas fraction is increased, i.e. the lowest water saturation is expected at the highest gas fractions. However, this was not observed for the co-injections with Tergitol TMN 10 (**Figure 9**) and Tergitol 15-S-9 (**Figure 10**). Both experiments observed the lowest water saturations at the gas fraction with the lowest foam-gas relative permeability and higher water saturations were observed at both lower and higher gas fractions.

The increase in water saturation was likely caused by the reduction in CO_2 phase pressure when foam coalesced and is consistent with the difference in water saturation observed during the co-injections using surfactants (foam) and brine (reference relative permeability), due to a lower pressure gradients and associated capillary numbers (Lake *et al.*, 2014). However, conceptually, the "limiting capillary pressure" describes an equilibrium region where increases in water saturation should cause foam regeneration and subsequent re-reduction in water, thereby maintaining a constant water saturation (Vassenden and Holt, 2000). A lack of foam regeneration when the water saturation increased may explain the observed behaviour during co-injections with Tergitol TMN 10 and Tergitol 15-S-9, indicating that the foam generation was more related to fractional flow and less to the water saturation.

The observation has implications, resulting in a relationship between the foam gas relative permeability (k_{rg}^{f}) and water saturation (S_w) that the V-H foam model (and other implicit-texture local-equilibrium foam models) cannot capture. Relative permeability curves derived from experimental data, which is used as input for reservoir scale simulations, should for each saturation have only one relative permeability, i.e. a monotonic relative permeability curve. This is evidently not the case for two foam co-injections using Tergitol TMN 10 and Tergitol 15-S-9 and the foam model fitted to the experimentally observed relative permeability data points is not applicable for reliable simulations.

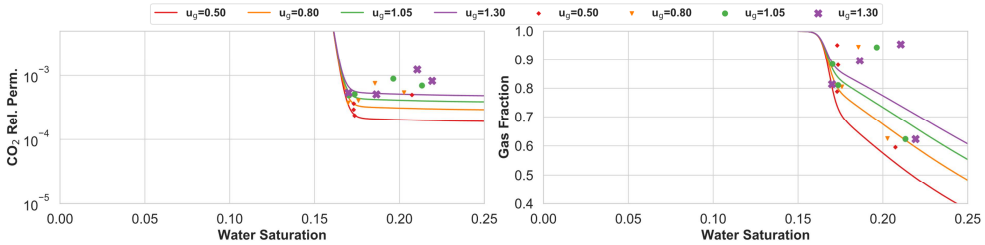

Fig. 9: Steady-state foam flood using the Tergitol TMN 10 (non-ionic). Left: Relative permeability versus water saturation. Right: Fractional flow (gas and water) versus water saturation. The experimental data points at different gas flow velocities are shown using unique shapes and colours. Modelled curves are shown using lines; gas flow velocities are shown using the same colour-scheme as the experimental data points.

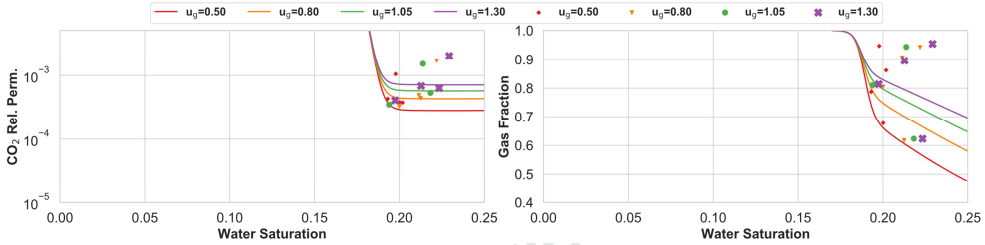

Fig. 10: Steady-state foam flood using the Tergitol 15-S-9 (non-ionic). Left: Relative permeability versus water saturation. Right: Fractional flow (gas and water) versus water saturation. The experimental data points at different gas flow velocities are shown using unique shapes and colours. Modelled curves are shown using lines; gas flow velocities are shown using the same colour-scheme as the experimental data points.

3.4 Surfactant performance as foam stabilizers

All six surfactants generated foam during the steady-state co-injections, reducing CO_2 mobility by more than three orders of magnitude (**Figure 11**). Four of the foam co-injections (AOS, Brij L23, Igepal CO720 and Tergitol NP10) exhibited a relationship between reduced gas relative permeability, water saturation, flow rate and gas fraction, in both the low- and high-quality regime and were capable of being captured by the V-H model (Table 5). However, two of the foam co-injections (Tergitol TMN10 and Tergitol 15-S-9), exhibited a non-monotonic change in water saturation, which the V-H foam model (and other implicit-texture local-equilibrium foam models) was not capable of capturing.

Table 5: Foam parameters and Lw values for all co-injections with surfactant solution

Surfactant	S^*	s_1	s_2	FM_0	L_w
Capable of being captured by the V-H model					
AOS	0.07	260	-7.0	0.00009	**2.2**
Brij L23	0.12	310	-7.0	0.00055	**2.2**
Igepal CO720	0.12	330	-9.0	0.00035	**2.4**
Tergitol NP10	0.14	500	-7.5	0.00050	**2.4**
Not capable of being captured by the V-H model					
Tergitol TMN10	0.15	400	-8.0	0.00050	**2.2**
Tergitol 15-S-9	0.17	350	-9.0	0.00080	**2.2**

Two features obtained from the steady-state co-injections and associated model fitting are of particular interest when comparing and evaluating the performance of the surfactants as foaming agents. These include the water saturation where foam will abruptly collapse (S_w^*) and the largest MRF, which it is by definition inversely proportional to FM_0 (Equation 8). In general, a stronger foam (higher MRF) is beneficial as it improves the foam's ability to divert flow at the reservoir scale, increasing the volume of the reservoir swept during CO_2 injection. However, large mobility reductions can impair injectivity. Increased foam breakdown saturation (S_w^*) improves the stability foam at high gas saturation, which is beneficial. An additional effect of foam being stable a lower water saturation is decreased residual water saturation, increasing the pore volume available for CO_2 storage.

The overview (**Figure 11**) shows a clear difference in the performance between the extensively studied anionic AOS surfactant and the five non-ionic surfactants. The AOS surfactant had 4 to 10 times higher MRF and a 50% reduction in S_w^*, compared to the non-ionic surfactants. MRF accounts for the differences in temperature between the AOS surfactant co-injection (80 C°) and the non-ionic surfactant co-injections (40 C°) because the viscosity of CO_2 at the respective temperatures are included in the calculations. Despite the discrepancies in performance, secondary properties of the non-ionic surfactants such as rock absorption and being transportable by both the aqueous and gaseous phase was not considered and could outweigh the higher performance of the AOS surfactant. Complete assessments require field-scale numerical simulations using the obtained foam parameters, but also additional parameters representing concentrations, adsorption, transport, *etc*. It is interesting to observe that the two surfactants that could not be fitted to the V-H model are also the surfactants with the largest partitioning coefficients (*cf.* Table 3), *i.e.* the most CO_2 soluble surfactants. The three other non-ionic surfactants are, in this respect, more similar to the anionic AOS.

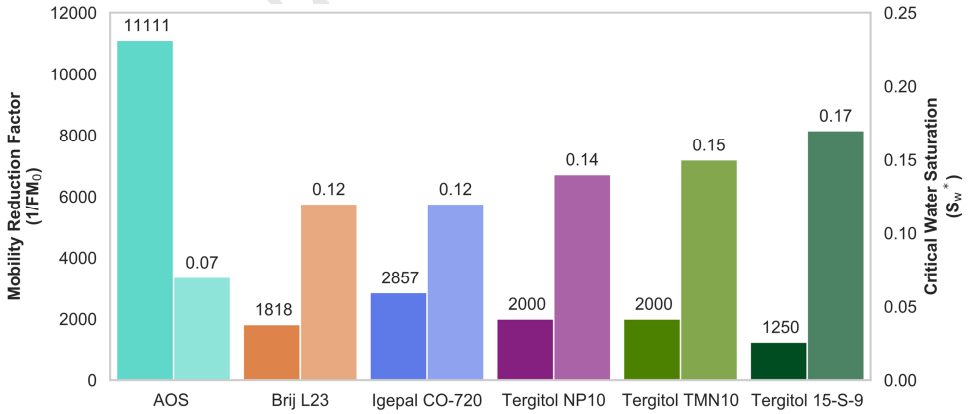

Fig. 11: Performance of the surfactants by MRF (left columns, higher is better) and foam breakdown saturation, S_w* (right columns, lower is better).

4 Conclusions

This study presented a series of steady-state co-injections of dense phase CO_2 with either anionic or non-ionic surfactant solutions at varying CO_2 flow velocities and CO_2 fractions. Six different surfactants were evaluated including the well-known anionic water-soluble AOS surfactant and five non-ionic partially CO_2-soluble surfactants. The performance of the different surfactants for stabilizing foam in porous media were evaluated by the mobility reduction factor (MRF) and the limiting water saturation where foam abruptly collapses (S_w^*).

All surfactants generated foam that reduced the mobility of CO_2 by more than three orders of magnitude. However, the AOS surfactant outperformed the non-ionic surfactants with respect to mobility reduction, exceeding a four order of magnitude reduction in MRF. The water saturations during the foam injections were significantly lower compared to the water saturations during the reference CO_2 and water relative permeability measurements due to the higher capillary number (pressure differential). An additional effect of foam being stable lower water saturations is decreased residual water saturation, which increases the pore volume available for CO_2 storage.

The V-H local-equilibrium foam model captured the experimental observations from the co-injections using the anionic AOS surfactant and three of the five non-ionic surfactants, including the reduction of foam strength in the high-quality regime and the shear-thinning flow behaviour in the low-quality regime. The model fit demonstrated the applicability of the experimental dataset for use as input into implicit-texture local-equilibrium foam models. However, two of the co-injections (Igepal CO720 and Tergitol NP10) required minute adjustments in the water relative permeability curves to achieve a model fit. Non-monotonic water saturation changes were also observed in co-injections using two of the tested surfactants (Tergitol TMN10 and Tergitol 15-S-9), which the foam model was not capable of capturing. Nonetheless, the modelling work elucidated subtle experimental trends and demonstrated the applicability of the dataset as input into implicit-texture local-equilibrium foam models.

4.1 Data Availability

Datasets from the seven co-injections can be found at http://dx.doi.org/10.17632/fz56dzr8p3.1, an open-source online data repository hosted by Mendeley Data (Føyen and Holt, 2020).

4.2 Acknowledgements

The authors wish to acknowledge the Research Council of Norway for financial support: *Improved performance of CO_2 EOR and underground storage by mobility control of CO_2* (project no. 267859 wherein all experimental work was performed); *CO_2 Storage From Laboratory to On-Shore Field Pilots Using CO_2-Foam for Mobility Control in CCUS* (project no. 249742); *Nanoparticles to Stabilize CO2-foam for Efficient CCUS in Challenging Reservoirs* (project no. 268216); and for funding of PhD candidate Tore Føyen.

4.3 Abbreviation

AOS	Alpha olefin sulfonate
Cs-dSSW	Caesium doped synthetic seawater
CO_2	Carbon dioxide
EOR	Enhanced oil recovery
ISSM	In-situ Saturation Monitoring
V-H	Foam model , Vassenden and Holt

4.4 Symbols

f_i	Modelled value
FM	Gas mobility reduction factor
f_w and f_g	Fractional flow (water, gas)
I_{Sw}	Recorded γ-ray intensity
$I_{Sw=1}$ and $I_{Sw=0}$	Reference scans (water, gas)
kp	Partition coefficient
k	Permeability
k_{rw} and k_{rg}	Relative permeability (water, gas)
k_{rg}^f	Gas-foam relative permeability
L_g, E_g, T_g, k_{rg}^x, L_w, E_w, T_w, k_{rg}^0	Relative permeability parameters (LET)
$NaNO_3$	Sodium nitrate
P_c^*	Critical capillary pressure
∇p_w and ∇p_g	Pressure gradient (water, gas)
MRF	Mobility reduction factor
R^2	Coefficient of determination
S_1, S_2, S^*, u_{g0}, FM_0	Foam parameters (V-H model)
S_{gr}	Residual gas saturation
SS_{res}	Sum of squares of residuals
SS_{tot}	The total sum of squares
S_W	Water saturation
S_w^*	Foam breakdown saturation
S_{wn}	Normalized water saturation
S_{wi}	Irreducible water saturation
u_w and u_g	Darcy velocity (water, gas)
$\bar{y}$	Mean of the observed data
y_i	Observed data
Wt.%	Weight percentage
μ_{app}	Foam Apparent viscosity
$\mu_w$and μ_g	Viscosity (water, gas)

4.5 References

Adkins, S.S., Chen, X., Chan, I., Torino, E., Nguyen, Q.P., Sanders, A.W. and Johnston, K.P., 2010. Morphology and Stability of CO2-in-Water Foams with Nonionic Hydrocarbon Surfactants. Langmuir, 26(8): 5335-5348. https://doi.org/10.1021/la903663v

Alcorn, Z.P., Fredriksen, S.B., Sharma, M., Rognmo, A.U., Føyen, T.L., Fernø, M.A. and Graue, A., 2019. An Integrated Carbon-Dioxide-Foam Enhanced-Oil-Recovery Pilot Program With Combined Carbon Capture, Utilization, and Storage in an Onshore Texas Heterogeneous Carbonate Field. SPE Reservoir Evaluation & Engineering, 22(04): 1449-1466, SPE-190204-PA https://doi.org/10.2118/190204-PA

Barrabino, A., Holt, T. and Lindeberg, E., 2020. Partitioning of non-ionic surfactants between CO2 and brine. Journal of Petroleum Science and Engineering, 190: 107106. https://doi.org/10.1016/j.petrol.2020.107106

Bernard, G.G. and Jacobs, W.L., 1965. Effect of Foam on Trapped Gas Saturation and on Permeability of Porous Media to Water. Society of Petroleum Engineers Journa, 5(04: 295-300, SPE-1204-PA,). https://doi.org/10.2118/1204-PA

Blaker, T., Aarra, M.G., Skauge, A., Rasmussen, L., Celius, H.K., Martinsen, H.A. and Vassenden, F., 2002. Foam for Gas Mobility Control in the Snorre Field: The FAWAG Project. SPE Reservoir Evaluation & Engineering, 5(04): 317-323, SPE-78824-PA. https://doi.org/10.2118/78824-PA

Borling, D. (1994). Injection Conformance Control Case Histories Using Gels at the Wertz Field CO2 Tertiary Flood in Wyoming. SPE/DOE Improved Oil Recovery Symposium. https://doi.org/10.2118/27825-MS

Chen, Y., Elhag, A.S., Poon, B.M., Cui, L., Ma, K., Liao, S.Y., Omar, A., Worthen, A., Hirasaki, G.J., Nguyen, Q.P. and Johnston, K.P. (2012). Ethoxylated Cationic Surfactants For CO2 EOR In High Temperature, High Salinity Reservoirs. SPE Improved Oil Recovery Symposium, Tulsa, Oklahoma, USA. https://doi.org/10.2118/154222-MS

Chou, S., Vasicek, S., Pisio, D., Jasek, D. and Goodgame, J. (1992). CO2 Foam Field Trial at North Ward-Estes. SPE annual technical conference and exhibition. https://doi.org/10.2118/24643-MS

Eftekhari, A.A. and Farajzadeh, R., 2017. Effect of Foam on Liquid Phase Mobility in Porous Media. Scientific Reports, 7. https://doi.org/10.1038/srep43870

Enick, R.M., Olsen, D.K., Ammer, J.R. and Schuller, W. (2012). Mobility and Conformance Control for CO2 EOR via Thickeners, Foams, and Gels -- A Literature Review of 40 Years of Research and Pilot Tests. SPE Improved Oil Recovery Symposium, Tulsa, Oklahoma, USA. https://doi.org/10.2118/154122-MS

Ettehadtavakkol, A., Lake, L.W. and Bryant, S.L., 2014. CO2-EOR and storage design optimization. International Journal of Greenhouse Gas Control, 25: 79-92. https://doi.org/10.1016/j.ijggc.2014.04.006

Falls, A.H., Musters, J.J. and Ratulowski, J., 1989. The Apparent Viscosity of Foams in Homogeneous Bead Packs. SPE Reservoir Engineering, 4(02): 155-164, SPE-16048-PA. https://doi.org/10.2118/16048-PA

Farajzadeh, R., Krastev, R. and Zitha, P.L.J., 2008. Foam films stabilized with alpha olefin sulfonate (AOS). Colloids and Surfaces A: Physicochemical and Engineering Aspects, 324(1): 35-40. https://doi.org/10.1016/j.colsurfa.2008.03.024

Farajzadeh, R., Lotfollahi, M., Eftekhari, A.A., Rossen, W.R. and Hirasaki, G.J.H., 2015. Effect of Permeability on Implicit-Texture Foam Model Parameters and the Limiting Capillary Pressure. Energy & Fuels, 29(5): 3011-3018. https://doi.org/10.1021/acs.energyfuels.5b00248

Farajzadeh, R., Muruganathan, R.M., Rossen, W.R. and Krastev, R., 2011. Effect of gas type on foam film permeability and its implications for foam flow in porous media. Advances in Colloid and Interface Science, 168(1): 71-78. https://doi.org/10.1016/j.cis.2011.03.005

Føyen, T., Brattekås, B., Fernø, M.A., Barrabino, A. and Holt, T., 2020. Increased CO2 storage capacity using CO2-foam. International Journal of Greenhouse Gas Control, 96: 103016. https://doi.org/10.1016/j.ijggc.2020.103016

[Dateset] Føyen, T. and Holt, T., 2020. "Dataset: CO2 Mobility Reduction by Foam Stabilized using CO2- and Water-Soluble Surfactants". Mendeley Data. https://doi.org/10.17632/fz56dzr8p3.1

Henry, R.L., Fisher, D.R., Pennell, S.P. and Honnert, M.A. (1996). Field Test of Foam to Reduce CO2 Cycling. SPE/DOE Improved Oil Recovery Symposium. https://doi.org/10.2118/35402-MS

Hirasaki, G.J. and Lawson, J.B., 1985. Mechanisms of Foam Flow in Porous Media: Apparent Viscosity in Smooth Capillaries. Society of Petroleum Engineers Journal, 25(02): 176-190, SPE-12129-PA. https://doi.org/10.2118/12129-PA

Hoefner, M. and Evans, E., 1995. CO2 Foam: Results From Four Developmental Field Trials. SPE Reservoir Engineering, 10(04): 273-281. https://doi.org/10.2118/27787-PA

IEA, 2018. World Energy Outlook 2018, IEA, Paris.

IPPC, 2014. Climate Change 2014: Synthesis Report. Contribution of Working Groups I, II and III to the Fifth Assessment Report of the Intergovernmental Panel on Climate Change, Geneva.

Jonas, T., Chou, S. and Vasicek, S. (1990). Evaluation of a CO2 Foam Field Trial: Rangely Weber Sand Unit. SPE Annual Technical Conference and Exhibition. https://doi.org/10.2118/20468-MS

Jones, S.A., Laskaris, G., Vincent-Bonnieu, S., Farajzadeh, R. and Rossen, W.R., 2016. Effect of surfactant concentration on foam: From coreflood experiments to implicit-texture foam-model parameters. Journal of Industrial and Engineering Chemistry, 37: 268-276. https://doi.org/10.1016/j.jiec.2016.03.041

Kovscek, A.R. and Radke, C.J., 1994. Fundamentals of Foam Transport in Porous Media, Foams: Fundamentals and Applications in the Petroleum Industry. Advances in Chemistry. American Chemical Society, pp. 115-163.

Lake, L.W., Johns, R.T., Rossen, R.W. and Pope, G.A., 2014. Fundamentals of Enhanced Oil Recovery. Society of Petroleum Engineers, Richardson, 496 pp.

Le, V.Q., Nguyen, Q.P. and Sanders, A. (2008). A Novel Foam Concept With CO2 Dissolved Surfactants. SPE Symposium on Improved Oil Recovery, Tulsa, Oklahoma, USA. https://doi.org/10.2118/113370-MS

Lee, S. and Kam, S.I., 2013. Chapter 2 - Enhanced Oil Recovery by Using CO2 Foams: Fundamentals and Field Applications. In: J.J. Sheng (Editor), Enhanced Oil Recovery Field Case Studies. Gulf Professional Publishing, Boston, pp. 23-61.

Lindeberg, E., Grimstad, A.-A., Bergmo, P., Wessel-Berg, D., Torsæter, M. and Holt, T., 2017. Large Scale Tertiary CO2 EOR in Mature Water Flooded Norwegian Oil Fields. Energy Procedia, 114: 7096-7106. https://doi.org/10.1016/j.egypro.2017.03.1851

Lomeland, F., Ebeltoft, E. and Thomas, W.H. (2005). A New Versatile Relative Permability Correlation. International Symposium of the Society of Core Analysts Toronto, Canada, Alternate A New Versatile Relative Permability Correlation.

Ma, K., Ren, G., Mateen, K., Morel, D. and Cordelier, P., 2015. Modeling Techniques for Foam Flow in Porous Media. SPE-195310-PA, 20. https://doi.org/10.2118/169104-PA

McLendon, W.J., Koronaios, P., McNulty, S., Enick, R.M., Biesmans, G., Miller, A.N., Salazar, L.C., Soong, Y., Romanov, V. and Crandall, D. (2012). Assessment of CO2-Soluble Surfactants for Mobility Reduction using Mobility Measurements and CT Imaging. SPE Improved Oil Recovery Symposium, Tulsa, Oklahoma, USA. https://doi.org/10.2118/154205-MS

Moffitt, P., Pecore, D., Trees, M. and Salts, G. (2015). East Vacuum Grayburg San Andres Unit, 30 Years of CO2 Flooding: Accomplishments, Challenges and Opportunities. SPE Annual Technical Conference and Exhibition. https://doi.org/10.2118/175000-MS

Reed, J. and Cense, A. (2018). In Situ Saturation Monitoring (ISSM) – Recommendations for Improved Processing. International Symposium of the Society of Core Analysts, Trondheim

Rossen, W.R. and Wang, M.W., 1999. Modeling Foams for Acid Diversion. SPE Journal, 4(02): 92-100, SPE-56396-PA. https://doi.org/10.2118/56396-PA

Valavanides, M.S., 2018. Review of Steady-State Two-Phase Flow in Porous Media: Independent Variables, Universal Energy Efficiency Map, Critical Flow Conditions, Effective Characterization of Flow and Pore Network. Transport in Porous Media, 123(1): 45-99. https://doi.org/10.1007/s11242-018-1026-1

Vassenden, F. and Holt, T., 2000. Experimental Foundation for Relative Permeability Modeling of Foam. SPE Reservoir Evaluation & Engineering, 3(02): 179-185, SPE-62506-PA. https://doi.org/10.2118/62506-PA

Vassenden, F., Holt, T., Ghaderi, A. and Solheim, A., 1999. Foam Propagation on Semi-Reservoir Scale. SPE Reservoir Evaluation & Engineering, 2(05): 436-441, SPE-58047-PA. https://doi.org/10.2118/58047-PA

Vitoonkijvanich, S., AlSofi, A.M. and Blunt, M.J., 2015. Design of foam-assisted carbon dioxide storage in a North Sea aquifer using streamline-based simulation. International Journal of Greenhouse Gas Control, 33: 113-121. https://doi.org/10.1016/j.ijggc.2014.11.022

Worthen, A.J., Alzobaidi, S., Tran, V., Iqbal, M., Liu, J.S., Cornell, K.A., Kim, I., DiCarlo, D.A., Bryant, S.L. and Huh, C., 2018. Design of nanoparticles for generation and stabilization of CO2-in-brine foams with or without added surfactants. arXiv preprint arXiv:1811.11217

Xing, D., Wei, B., McLendon, W.J., Enick, R.M., McNulty, S., Trickett, K., Mohamed, A., Cummings, S., Eastoe, J., Rogers, S., Crandall, D., Tennant, B., McLendon, T., Romanov, V. and Soong, Y., 2012. CO2-Soluble, Nonionic, Water-Soluble Surfactants That Stabilize CO2-in-Brine Foams. SPE Journal, 17(04): 1172-1185, SPE-129907-PA. https://doi.org/10.2118/129907-PA

Xing, D., Wei, B., Trickett, K., Mohamed, A., Eastoe, J., Soong, Y. and Enick, R.M. (2010). CO2-Soluble Surfactants for Improved Mobility Control. SPE Improved Oil Recovery Symposium, Tulsa, Oklahoma, USA. https://doi.org/10.2118/129907-MS

Highlights

Six surfactants, five non-ionic CO_2-soluble, were evaluated as foam stabilizers

All surfactants generated foam that reduced the mobility of CO_2 by more than three orders

A foam model captured the experimental observations

CO_2 foam decreased water saturation, increasing the volume for CO_2 storage.

Føyen, T: Formal analysis, Visualization, Writing - Original Draft

Alcorn, Z.P.: Writing - Review & Editing

Fernø, M.A.: Writing - Review & Editing,

Barrabino, A.: Investigation, Writing - Review & Editing

Holt, T: Project administration, Investigation, Formal analysis, Writing - Review & Editing

Declaration of interests

☒ The authors declare that they have no known competing financial interests or personal relationships that could have appeared to influence the work reported in this paper.

☐The authors declare the following financial interests/personal relationships which may be considered as potential competing interests:

Graphic design: Communication Division, UiB / Print: Skipnes Kommunikasjon AS

uib.no

ISBN: 9788230845677 (print)
9788230864319 (PDF)